

construction
engineering
research
laboratory

PT
TECHNICAL REPORT M-170

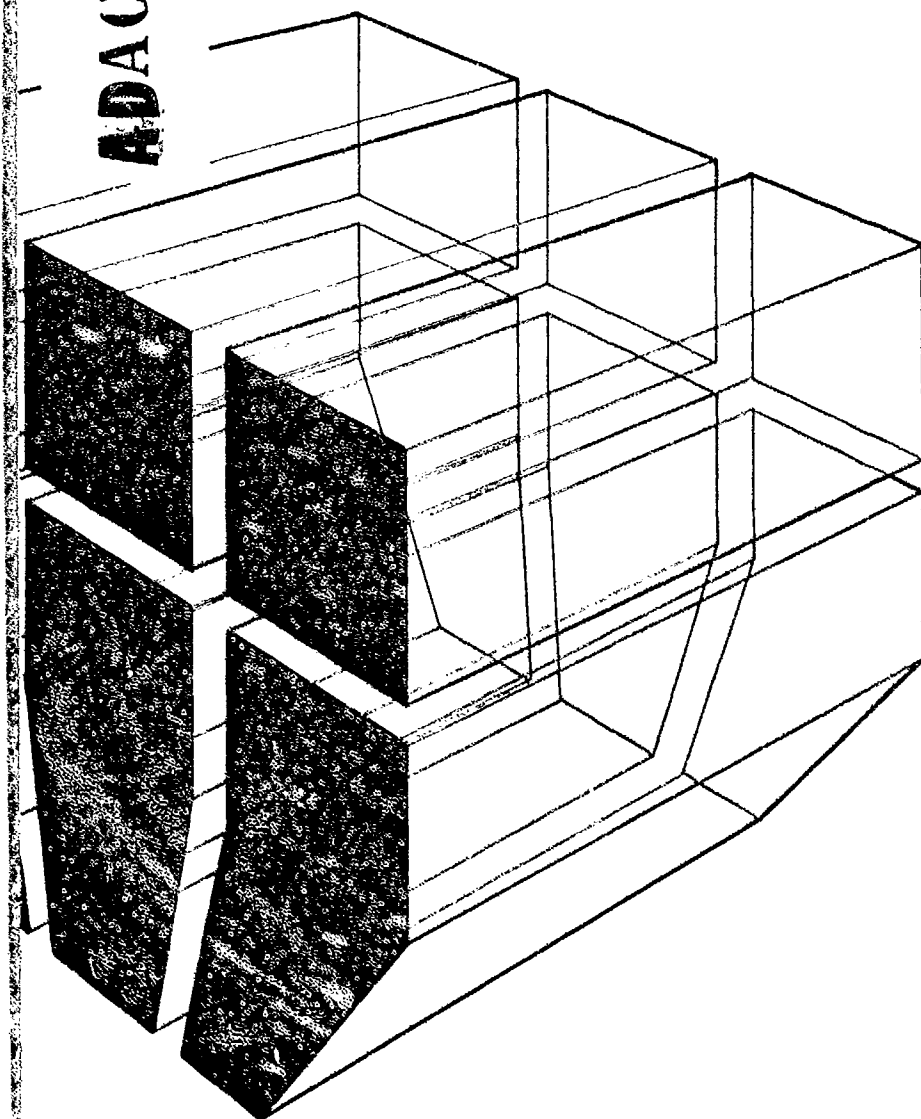
November 1975

Characterization of Fracture of Engineering Materials

ADA019930

FRACTURE CHARACTERISTICS OF STRUCTURAL
STEELS AND WELDMENTS

by
J. Aleszka
Y. G. Kim

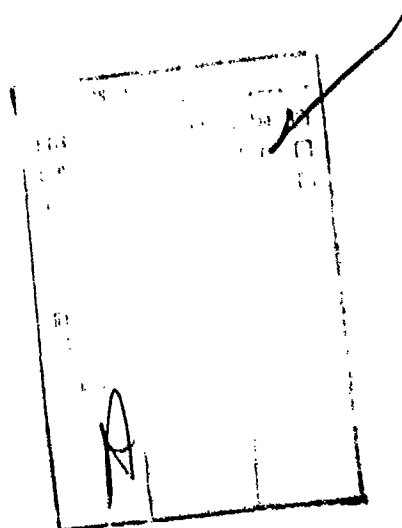


D D C
JAN 29 1976
A

WV
GERL

Approved for public release; distribution unlimited.

The contents of this report are not to be used for advertising, publication, or promotional purposes. Citation of trade names does not constitute an official indorsement or approval of the use of such commercial products. The findings of this report are not to be construed as an official Department of the Army position, unless so designated by other authorized documents.



DESTROY THIS REPORT WHEN IT IS NO LONGER NEEDED
DO NOT RETURN IT TO THE ORIGINATOR

UNCLASSIFIED

SECURITY CLASSIFICATION OF THIS PAGE (When Data Entered)

REPORT DOCUMENTATION PAGE		READ INSTRUCTIONS BEFORE COMPLETING FORM
1. REPORT NUMBER TECHNICAL REPORT M-170	2. GOVT ACCESSION NO.	3. RECIPIENT'S CATALOG NUMBER (19) CERL-TR-M-170
4. TITLE (and Subtitle) 6 FRACTURE CHARACTERISTICS OF STRUCTURAL STEELS AND WELDMENTS	5. TYPE OF REPORT & PERIOD COVERED 9 FINAL rept.	
7. AUTHOR(s) 10 J. Aleszka Y. G. Kim	8. CONTRACT OR GRANT NUMBER(s) (12) 111 f.	
9. PERFORMING ORGANIZATION NAME AND ADDRESS CONSTRUCTION ENGINEERING RESEARCH LABORATORY P.O. BOX 4005 Champaign, IL 61820	10. PROGRAM ELEMENT, PROJECT, TASK AREA & WORK UNIT NUMBERS (16) DA-4A761102AT23-02-002	
11. CONTROLLING OFFICE NAME AND ADDRESS	12. REPORT DATE (11) November 1975	
	13. NUMBER OF PAGES	
14. MONITORING AGENCY NAME & ADDRESS (if different from Controlling Office)	15. SECURITY CLASS. (of this report) UNCLASSIFIED	
(17) 4-A-761102-AT-2302	15a. DECLASSIFICATION/DOWNGRADING SCHEDULE	
16. DISTRIBUTION STATEMENT (of this Report) Approved for public release; distribution unlimited.		
17. DISTRIBUTION STATEMENT (of the abstract entered in Block 20, if different from Report)		
18. SUPPLEMENTARY NOTES Copies are obtainable from National Technical Information Service Springfield, VA 22151		
19. KEY WORDS (Continue on reverse side if necessary and identify by block number) fracture characteristics scanning electron microscope structure steel steel weldments		
20. ABSTRACT (Continue on reverse side if necessary and identify by block number) This report presents the findings of a scanning electron microscope study of the tensile, fatigue, and impact fracture characteristics of a carbon steel; two high-strength, low-alloy steels; and a high-strength steel weldment. Tension and fatigue specimens were tested in as-received, hydrogen-embrittled, and temper-embrittled conditions, while impact specimens were tested in the as-received condition only. The failure mode of embrittled and unembrittled weldments containing induced weld defects was also studied.		

UNCLASSIFIED

SECURITY CLASSIFICATION OF THIS PAGE(When Data Entered)

The hydrogen-enbrittled, high-strength steels exhibited large reductions in ductility and fatigue life. The fracture surfaces of these specimens contained a dispersion of fish-eyes and craters. Temper embrittling the high-strength steels increased their susceptibility to lamellar tearing.

The carbon steel was not as susceptible to either hydrogen or temper embrittlement as the high-strength steels.

Crack nucleation in the unembrittled weldments occurred at the weld defect, while failure in the embrittled weldments began at both an outside edge and the weld defect.

UNCLASSIFIED

SECURITY CLASSIFICATION OF THIS PAGE(When Data Entered)

FOREWORD

This investigation was conducted by the Metallurgy Branch, Materials Systems and Science Division (MS) of the U.S. Army Construction Engineering Research Laboratory (CERL). The study was sponsored by the Directorate of Military Construction, Office of the Chief of Engineers, under Project 4A761102AT23, "Structural Systems," Scientific Area 02, "Facility Components," Work Unit 002, "Characterization of Fracture of Engineering Materials." The OCE Technical Monitor was I. A. Schwartz.

CERL personnel connected with the investigation were J. Aleszka, S. Joshi and Dr. Y. G. Kim. Dr. R. Quattrone is Chief of the Metallurgy Branch, and Dr. W. E. Fisher is Acting Chief of MS. COL M. D. Remus is Commander and Director of CERL and Dr. L. R. Shaffer is Deputy Director.

CONTENTS

DD FORM 1473	1
FOREWORD	3
LIST OF TABLES AND FIGURES	5
1 INTRODUCTION	11
Objective	
Approach	
Background	
2 EXPERIMENTAL PROCEDURE	14
Materials	
Welding Procedure	
Specimen Fabrication and Testing	
Hydrogen Embrittlement	
Temper Embrittlement	
3 RESULTS AND DISCUSSION	16
ASTM A-36	
ASTM A-517 Grade F (USS T-1) Steel	
HY-130 Steel	
AX-110 Weld	
Failure of Defective Weldments	
4 CONCLUSIONS	22
FIGURES	23
GLOSSARY	110
REFERENCES	110
DISTRIBUTION	

TABLES

Number	Page
1 Chemical Composition of Steels and Weld Metal	14
2 Mechanical Properties of Steels and Weld Metal	15
3 Welding Parameters	15
4 Temperatures and Environments of Charpy Tests	15
5 Summary of Tests Conducted in This Study	17
6 Summary of Fatigue Test Parameters and Data	17

FIGURES

1 Equiaxed Dimples Containing Inclusions, 4250x	23
2 Elongated Dimples, 3750x	23
3 Cleavage Facets, 400x	24
4 Quasi-Cleavage Facets, 1600x	24
5 Fatigue Striations, 4000x	25
6 Intergranular Fracture, 300x	25
7 Microstructure of A-36 Steel, 200x	26
8 Microstructure of T-1 Steel, 200x	26
9 Microstructure of HY-130 Steel, 200x	26
10 Specimen Joints for Welding	27
11 Specimen Geometry for Tensile and Charpy Impact Tests	28
12 Specimen Geometry for Fatigue Tests	28
13 Load-Deflection Curves for A-36, T-1, and HY-130 Steel	29
14 Variation in Absorbed Energy for A-36, T-1, and HY-130 Steel and AX-110 Weld Deposit	30
15 Tensile Fracture Surface of A-36 Steel, 12x	31
16 Dimple Rupture in A-36 Steel, 1000x	31
17 Plastic Deformations in Dimple Rupture in A-36 Steel, 3000x	32
18 Tensile Fracture Surface of Hydrogen-Embrittled A-36 Steel, 10x	32
19 Quasi-Cleavage Facets in Hydrogen-Embrittled A-36 Steel, 1100x	33
20 Inclusion-Nucleated Dimples in Hydrogen-Embrittled A-36 Steel, 2000x	33
21 Fatigue Fracture Surface of A-36 Steel, 8x	34
22 Fatigue Striations on Surface of A-36 Steel, 4000x	34
23 Stereo Micrograph of Fatigue Zone in A-36 Steel, 500x	35
24 Tensile Overload Region in A-36 Fatigue Specimen, 700x	35
25 Fracture Surface of a Hydrogen-Embrittled A-36 Fatigue Specimen, 8x	36
26 Fatigue Striations on Surface of Hydrogen-Embrittled A-36 Fatigue Specimen, 4250x	36
27 Stereo Micrograph of Fatigue Zone in Embrittled A-36 Steel, 500x	37
28 Tensile Overload Region in Embrittled A-36 Fatigue Specimen, 1400x	37
29 Fracture Surface of A-36 Charpy Specimen Tested at -196°C, 7x	38
30 Cleavage Fracture in A-36 Charpy Specimen Tested at -196°C, 100x	38
31 River Patterns in Cleavage Facets, 500x	39
32 Fracture Surface of A-36 Charpy Specimen Tested at -83°C, 7x	39
33 Mixed Mode Failure in A-36 Charpy Specimen Tested at -83°C, 1000x	40
34 Fracture Surface of A-36 Charpy Specimen Tested at -18°C, 7x	40
35 Dimple Rupture in Notch Region of A-36 Charpy Specimen Tested at -18°C, 100x	41
36 Mixed Mode Failure in Central Region of A-36 Charpy Specimen Tested at -18°C, 100x	41
37 Fracture Surface of A-36 Charpy Specimen Tested at Room Temperature, 7x	42

FIGURES (cont'd)

Number	Page
38 Dimple Rupture in Notch Region of A-36 Charpy Specimen Tested at Room Temperature, 100x	42
39 Cleavage Fracture in Central Region of A-36 Charpy Specimen Tested at Room Temperature, 100x	43
40 Microvoid Coalescence and Inclusion-Generated Voids in Region Near Notch, 1000x	43
41 Microvoid Coalescence Interspersed Among Cleavage Facets in Central Region of A-36 Charpy Specimen Tested at Room Temperature, 1000x	44
42 Tensile Fracture Surface of T-1 Steel Plate Specimen, 8x	44
43 Equiaxed Dimples in Central Region of Fracture Surface, 1500x	45
44 Equiaxed Dimples Containing Inclusions, 7500x	45
45 Tensile Fracture Surface of Hydrogen-Embrittled T-1 Steel, 8x	46
46 Tensile Failure of Hydrogen-Embrittled Steel by Dimple Rupture, 650x	46
47 Tensile Fracture Surface of Temper-Embrittled Steel, 8x	47
48 Tensile Failure of Temper-Embrittled T-1 Steel by Dimple Rupture, 375x	47
49 Equiaxed Dimples and Microvoid Coalescence in Temper-Embrittled T-1 Steel, 1500x	48
50 Fatigue Fracture Surface of a T-1 Steel Plate Specimen, 10x	48
51 Fatigue Striations on Surface of T-1 Fatigue Specimen, 1000x	49
52 Stereo Micrograph of Fatigue Zone in T-1 Steel, 1600x	49
53 Tensile Overload Region of T-1 Fatigue Specimen, 700x	50
54 Fracture Surface of Hydrogen-Embrittled T-1 Plate Fatigue Specimen, 8x	50
55 Fatigue Zone of Hydrogen-Embrittled T-1 Plate Fatigue Specimen, 60x	51
56 Stereo Micrograph of Fatigue Zone in Hydrogen-Embrittled T-1 Steel, 400x	51
57 Stereo Micrograph of Fatigue Zone in Hydrogen-Embrittled T-1 Steel, 500x	52
58 Optical Micrograph of Longitudinal Section of the Fatigue Zone in Hydrogen-Embrittled T-1 Steel, 550x	52
59 Optical Micrograph Showing the Beginning and Intermediate Stages of Crater Formation, 550x	53
60 Tensile Overload Region of Hydrogen-Embrittled T-1 Plate Fatigue Specimen, 140x	53
61 Fracture Surface of Temper-Embrittled T-1 Plate Fatigue Specimen, 10x	54
62 Transition Region from Fatigue to Tensile Overload in Temper-Embrittled T-1 Fatigue Specimen, 35x	54
63 Fatigue Striations on Fracture Surface of Temper-Embrittled T-1 Steel, 5000x	55
64 Dimple Rupture in Tensile Overload Region of Temper-Embrittled T-1 Steel Fatigue Specimen, 3500x	55
65 Fracture Surface of T-1 Charpy Specimen Tested at -196°C, 8x	56
66 Cleavage Fracture in T-1 Charpy Specimen Tested at -196°C, 250x	56
67 Cleavage Facets Containing Tear Lines, 5000x	57
68 Fracture Surface of T-1 Charpy Specimen Tested at -83°C, 8x	57
69 Edge of T-1 Charpy Specimen Tested at -83°C, 1000x	58
70 Center of T-1 Charpy Specimen Tested at -83°C, 1000x	58
71 Fracture Surface of T-1 Charpy Specimen Tested at -18°C, 8x	59
72 Failure of T-1 Charpy Specimen Tested at 18°C by Dimple Rupture, 1000x	59
73 Fracture Surface of T-1 Charpy Specimen Tested at Room Temperature, 10x	60
74 Failure of T-1 Charpy Specimen Tested at Room Temperature by Dimple Rupture, 1700x	60
75 Dimple Rupture by Microvoid Coalescence, 4750x	61
76 Tensile Fracture Surface of HY-130 Steel Specimen, 8x	61

FIGURES (cont'd)

Number	Page
77 Center of HY-130 Tensile Specimen, 1500x	62
78 Edge of HY-130 Tensile Specimen, 1600x	62
79 Tensile Fracture Surface of Hydrogen-Embrittled HY-130 Specimen, 9x	63
80 "Fisheyes" on Surface of Hydrogen-Embrittled HY-130 Tensile Specimen, 120x	63
81 Stereo Micrograph of Center of Fisheye on Fracture Surface of Hydrogen-Embrittled HY-130 Tensile Specimen, 1400x	64
82 Quasi-Cleavage Fracture in Fisheye, 1600x	64
83 Grain Boundary Separation With Microvoid Coalescence in Hydrogen-Embrittled HY-130 Tensile Specimen, 1200x	65
84 Grain Boundary Separation With Microvoid Coalescence in Hydrogen-Embrittled HY-130 Tensile Specimen, 3000x	65
85 Tensile Fracture Surface of Temper-Embrittled HY-130 Specimen, 8x	66
86 Fracture Surface of Temper-Embrittled HY-130 Tensile Specimen, 375x	66
87 Fracture of Temper-Embrittled HY-130 Tensile Specimen by Slipping, Tearing, and Microvoid Coalescence, 1500x	67
88 Fracture Surface of Round HY-130 Fatigue Specimen, 10x	67
89 Fracture Surface of Flat HY-130 Fatigue Specimen, 8x	68
90 Fatigue Region of HY-130 Fracture Surface, 50x	68
91 Fatigue Striations on Fracture Surface of HY-130 Steel, 1450x	69
92 Stereo Micrograph of Fatigue Zone in HY-130 Steel, 1550x	69
93 Tensile Overload Zone in HY-130 Fatigue Specimen, 1500x	70
94 Fracture Surface of Hydrogen-Embrittled HY-130 Fatigue Specimen, 10x	70
95 Fatigue Region of Hydrogen-Embrittled HY-130 Fatigue Specimen, 40x	71
96 Stereo Micrograph of Fatigue Zone in Hydrogen-Embrittled HY-130 Steel, 400x	71
97 Fatigue Striations on Fracture Surface of Hydrogen-Embrittled HY-130 Steel, 1600x	72
98 Tensile Overload Region in Hydrogen-Embrittled HY-130 Steel, 1500x	72
99 Fracture Surface of Temper-Embrittled HY-130 Fatigue Specimen, 8x	73
100 Fatigue Region of Temper-Embrittled HY-130 Fatigue Specimen, 60x	73
101 Fatigue Striations on Fracture Surface of Temper-Embrittled HY-130 Steel, 1600x	74
102 Stereo Micrograph of Fatigue Zone in Temper-Embrittled HY-130 Steel, 1500x	74
103 Slipping, Tearing, and Microvoid Coalescence Along One of Laminates in Temper-Embrittled HY-130 Steel, 800x	75
104 Band of Intergranular Fracture Between Fatigue and Tensile Overload Zones, 160x	75
105 Intergranular Fracture in Temper-Embrittled HY-130 Steel (Located in Center of 104), 1600x	76
106 Intergranular Fracture and Microvoid Coalescence in Temper-Embrittled HY-130 Steel, 800x	76
107 Fracture Surface of HY-130 Charpy Specimen Tested at -196°C, 8x	77
108 Cleavage Fracture in HY-130 Charpy Specimen Tested at -196°C, 1600x	77
109 Fracture Surface of HY-130 Charpy Specimen Tested at -83°C, 10x	78
110 Edge of an HY-130 Charpy Specimen Tested at -83°C, 650x	78
111 Center of HY-130 Charpy Specimen Tested at -83°C, 1600x	79
112 Fracture Surface of an HY-130 Charpy Specimen Tested at -18°C, 8x	79
113 Failure of HY-130 Charpy Specimen Tested at -18°C, 1600x	80
114 Fracture Surface of HY-130 Charpy Specimen Tested at Room Temperature, 8x	80
115 Failure of an HY-130 Charpy Specimen Tested at Room Temperature by Dimple Rupture, 1600x	81

FIGURES (cont'd)

Number		Page
116	Tensile Fracture Surface of an AX-110 Weld Specimen, 25x	81
117	Tensile Failure of AX-110 Weld Material by Dimple Rupture, 4000x	82
118	Tensile Fracture Surface of Hydrogen-Embrittled AX-110 Weld Specimen, 25x	82
119	Fisheye on the Fracture Surface of Hydrogen-Embrittled AX-110 Weld Specimen, 150x	83
120	Fracture Surface of Region in Fisheye, 1600x	83
121	Small Cleavage Facets Located in Fisheye, 4000x	84
122	Fracture Surface of Hydrogen-Embrittled AX-110 Weld Specimen Away From Fisheye, 1500x	84
123	Tensile Fracture Surface of Temper-Embrittled AX-110 Weld Specimen, 15x	85
124	Tensile Failure of Temper-Embrittled AX-110 Weld Specimen by Dimple Rupture, 750x	85
125	Fatigue Fracture Surface of an AX-110 Weld Specimen, 11x	86
126	Fatigue Cracks on Fracture Surface of AX-110 Weld Material, 4000x	86
127	Tensile Overload Region of AX-110 Weld Fracture Surface, 1500x	87
128	Fatigue Fracture Surface of Hydrogen-Embrittled AX-110 Weld Specimen, 10x	87
129	Stereo Micrograph of Fatigue Region in a Hydrogen-Embrittled AX-110 Weld Specimen, 40x	88
130	Fatigue Striations on Surface of Hydrogen-Embrittled AX-110 Weld Fatigue Specimen, 2000x	88
131	Stereo Micrograph of the Tensile Overload Region in a Hydrogen-Embrittled AX-110 Weld Fatigue Specimen, 1600x	89
132	Fatigue Fracture Surface of Temper-Embrittled AX-110 Weld Specimen, 11x	89
133	Fatigue Region of Temper-Embrittled AX-110 Weld Fracture Surface, 375x	90
134	Fatigue Striations on Fracture Surface of Temper-Embrittled AX-110 Weld Fatigue Specimen, 1500x	90
135	Lamellar Tearing Occurring in Fatigue Zone of Temper-Embrittled AX-110 Weld Specimen, 150x	91
136	Tensile Overload Region in Temper-Embrittled AX-110 Weld Fatigue Specimen, 750x	91
137	Fracture Surface of AX-110 Weld Charpy Specimen Tested at -196°C, 8x	92
138	Fracture Surface of AX-110 Weld Charpy Specimen Tested at -83°C, 8x	92
139	Fracture Surface of AX-110 Weld Charpy Specimen Tested at -18°C, 8x	93
140	Fracture Surface of AX-110 Weld Charpy Specimen Tested at Room Temperature, 8x	93
141	Failure of AX-110 Weld Charpy Specimen Tested at -196°C by Cleavage, 4000x	94
142	Center of AX-110 Weld Charpy Specimen Tested at -83°C, 4000x	94
143	Edge of an AX-110 Weld Charpy Specimen Tested at -83°C, 4000x	95
144	Fracture Surface of AX-110 Weld Charpy Specimen Tested at or Above -18°C, 4250x	95
145	Tensile Fracture Surface of AX-110 Weldment Containing LOP, 8x	96
146	LOP Region on Tensile Fracture Surface of AX-110 Weldment, Located in Center of Specimen, 250x	96
147	Transition Region on Tensile Fracture Surface of AX-110 Weldment, 1900x	97
148	Elongated Dimples on Tensile Fracture Surface of AX-110 Weldment, 4600x	97
149	Equiaxed Dimples on Tensile Fracture Surface of AX-110 Weldment, 4600x	98
150	Tensile Fracture Surface of AX-110 Weldment Containing LOP and LOF, 8x	98
151	LOP Region on Tensile Fracture Surface of AX-110 Weldment, 300x	99
152	LOF Region on Tensile Fracture Surface of AX-110 Weldment, 260x	99
153	Region Away From Defects on AX-110 Weldment Fracture Surface, 4000x	100

FIGURES (cont'd)

Number		Page
154	Tensile Fracture Surface of AX-110 Weldment Containing Porosity, 8x	100
155	Interior Surface of Pore, 2500x	101
156	Fracture Surface Away From Porosity Defects, 3500x	101
157	Fatigue Fracture Surface of an AX-110 Weldment Containing LOP, 8x	102
158	Fatigue Region of Fracture Surface of AX-110 Weldment Containing LOP, 1700x	102
159	Tensile Overload Region of Fatigue Fracture Surface of AX-110 Weldment Containing LOP, 3250x	103
160	Fatigue Fracture Surface of AX-110 Weldment Containing Porosity, 10x	103
161	Fatigue Initiation Site on Fracture Surface of AX-110 Weldment Containing Porosity, 50x	104
162	Fatigue Region of Fracture Surface of AX-110 Weldment Containing Porosity, 1380x	104
163	Tensile Overload Region of Fracture Surface of AX-110 Weldment Containing Porosity, 1380x	105
164	Fatigue Fracture Surface of a Hydrogen-Embrittled AX-110 Weldment Containing Porosity, 8x	105
165	Stereo Micrograph of Fatigue Region of Hydrogen-Embrittled AX-110 Weldment Containing Porosity, 120x	106
166	Origin of Fatigue Failure in Hydrogen-Embrittled AX-110 Weldment Containing Porosity, 120x	106
167	Tensile Overload Region in Hydrogen-Embrittled AX-110 Weldment Containing Porosity, 1000x	107
168	Fatigue Fracture Surface of Temper-Embrittled AX-110 Weldment Containing LOP, 8x	107
169	Origin of Failure of Temper-Embrittled AX-110 Weldment Containing LOP, 1400x	108
170	Secondary Origin of Fatigue Failure of Temper-Embrittled AX-110 Weldment Containing LOP, 70x	108
171	Fatigue Striations on Fracture Surface of Temper-Embrittled AX-110 Weldment Containing LOP, 1400x	109
172	Elongated Dimples on Shear Lip of Fracture Surface, 3500x	109

FRACTURE CHARACTERISTICS OF STRUCTURAL STEELS AND WELDMENTS

1 INTRODUCTION

Objective

The objective of this study was to use a scanning electron microscope (SEM) to establish and characterize the nature of fractures in engineering materials. This information should result in more efficient use of the materials and aid in understanding and minimizing their embrittlement. In addition, documenting the types of fracture modes will form the basis for analyzing in-service failure and help prevent similar failures in other applications.

Approach

The fracture characteristics of a low-carbon steel (ASTM A-36), two martensitic steels (ASTM A-517, also known as USS T-1, and HY-130), and high-strength steel weldments with and without induced defects were analyzed. The materials were fractured under tensile, fatigue, and impact loading conditions. The effects of hydrogen and temper embrittlement on the materials' behavior when fractured under tensile and fatigue conditions were investigated.

Background

Fracture of Steels

Fracture surface features can be divided into two categories according to the fracture propagation path: transgranular (through the grains) or intergranular (around the grains). In the transgranular fracture path category, fractures can occur by void coalescence, rupture, cleavage, or fatigue. Fractures in the intergranular fracture path category occur by grain boundary separation either with or without microvoid coalescence. Illustrations of these typical types of fracture are shown in Figures 1 through 6 as discussed below.

Many common structural metals fracture under monotonic load in a ductile fashion by microvoid coalescence. The microvoids may be nucleated at grain boundaries, second-phase particles, or other sites where strain discontinuities exist. As an applied load increases stress, the microvoids grow, coalesce, and eventually form a continuous fracture surface which exhibits numerous cup-like depressions called "dimples."

The shape of these dimples is strongly influenced by the orientation of the major stress axis. Equiaxed dimples (Figure 1) result under local conditions of uni-

axial tensile stress, while elongated dimples (Figure 2) result from failure caused by shear stress when the steel is stressed at a temperature above transition, and the shear component of the applied load is sufficiently large to overcome the shear strength of the material. Dimple size appears to depend on the number of fracture nucleation sites and the relative plasticity of the metal. If many fracture nucleation sites initiate microvoids prior to rupture, microvoid growth is limited due to intersection with other microvoid surfaces. As a result, numerous small, relatively shallow dimples are formed. However, if only a few microvoids are initiated prior to rupture, resulting dimples are large and deep.

Cleavage fractures (Figure 3) usually occur along well-defined crystallographic planes within a grain. In polycrystalline metals, a cleavage fracture propagating through one grain may have to change direction as it crosses subgrain boundaries or passes from one grain to another. The change in orientation between grains and the imperfections within grains usually produce easily distinguished markings on the fracture surface. A cleavage fracture propagating across grain or tilt boundaries forms arrays of cleavage steps or "river patterns." These river patterns are rootlike networks of cleavage facets propagating on different levels, which converge at the site of fracture initiation.¹

Quasi-cleavage (Figure 4) is a fracture mode which resembles cleavage in that it produces planar or nearly planar fracture facets; however, these facets are not parallel to the metal's normal cleavage planes.

Fatigue fracture results from stepped progression of a crack due to application of a cyclic load. The mechanism of fatigue crack nucleation is believed to involve slip plane fracture caused by repetitive reversing of the operative slip systems in the metal.² Crack growth caused by repetitive loading usually results in a fracture surface which exhibits closely spaced fatigue striations (Figure 5). Each fatigue striation represents the advance of a crack front during one loading cycle after initiation of fracture. The striations may be absent or differ in appearance depending on such variables as type of material, level and frequency of applied stress, and environment.

¹R. Honda, *International Conference on Fracture*, Sendai, Japan (1965); and J.R. Low, Jr., D.L. Averbach, et al., *Fracture* (John Wiley, 1959), p 163.

²P.J.E. Forsyth, "Fatigue Damage and Crack Growth in Aluminum Alloys," *ACTA Metallurgica*, Vol II, (1963) p 703; and C. Laird and G.C. Smith, "Crack Propagation in High Stress Fatigue," *Philosophical Magazine*, Vol 2, (1962), p 847.

Intergranular fracture resulting from grain boundary separation often results from segregation of impurity atoms along the grain boundaries (Figure 6). This segregation causes the grain boundaries to be extremely weak and brittle so an advancing crack needs very little energy to propagate along them. The surfaces of each block-like structure are the grain boundaries of the prior austenite phase. The basic difference between grain boundary separation with and without microvoid coalescence is that dimples appear on the fracture surface with microvoid coalescence. Intergranular fracture without microvoid coalescence frequently results when steel has been hydrogen- or temper-embrittled.

Hydrogen Embrittlement of Steel

Since hydrogen can easily be introduced into metals by melting, casting, welding, corrosion, and electroplating, hydrogen embrittlement has received considerable attention.³ Most investigations of hydrogen embrittlement have been performed under sustained-load or slow strain rate tensile test conditions. Research published on the behavior of hydrogen embrittlement under cyclic load conditions is limited.

The degree of embrittlement generally increases with increasing hydrogen content and tensile strength of iron-base alloys. Thus, hydrogen embrittlement is a greater problem with high-strength steels which have been exposed to hydrogen environments or contain hydrogen. The effect of hydrogen embrittlement is a sharp loss in ductility; this loss is most severe at room temperature and decreases with decreasing temperature and increasing strain rate. Reductions in fatigue life of steels due to electrolytically hydrogen-charging⁴ or testing in a hydrogen atmosphere⁵ have also been reported. The mode of failure of a hydrogen embrittled

sample depends on such variables as type of material, method of loading, and environment.

Many theories concerning the mechanism of hydrogen embrittlement have been proposed. Unfortunately, none has been able to account for more than half the experimental results. The first hydrogen embrittlement theory, proposed by Zaffe,⁶ was based on atomic hydrogen diffusing through the metal lattice, precipitating in internal voids as molecular hydrogen, and creating high pressures. It was assumed that high pressures in the voids combined with the externally applied stress to fracture the metal. Diffusion of hydrogen to the voids could explain the strain rate and temperature dependence of hydrogen embrittlement. However, this theory requires a regular array of pre-existing internal voids along which the hydrogen-charged sample can fracture, a requirement that is inconsistent with the results of studies delineating the structure of hydrogen-embrittled steels.⁷

Petch⁸ rejected the idea that cracking is propagated by internal hydrogen pressure. He suggested that adsorption of hydrogen on the surfaces of microcracks or voids lowers the surface free energy, thus also lowering the energy needed for crack propagation. He further suggested that although plastic deformation may produce many disconnected microcracks, they do not reduce fracture stress significantly in the absence of hydrogen. However, when hydrogen is present, it diffuses into the region of the advancing tip and is adsorbed on the surfaces of the crack, thereby reducing the energy required to propagate the crack.

Troiano⁹ has proposed that hydrogen which is evenly distributed throughout the metal lattice is harmless because its concentration is so small. The critical factor is the segregation of hydrogen, under an applied stress, to regions of triaxial stress near pre-existing voids in the steel; thus only hydrogen in the stressed region of the lattice is responsible for hydrogen embrittlement. Also, since hydrogen embrittlement is observed in transition metals having vacancies in the third subshell,

³P. Cotterill, "The Hydrogen Embrittlement of Metals," *Progressive Materials Science*, Vol 9, No. 4 (1961); A.S. Tetelman and A.J. McEvily, Jr., *Fracture of Structural Materials* (John Wiley, 1967); I.M. Bernstein, "The Role of Hydrogen in the Embrittlement of Iron and Steel," *Materials Science and Engineering*, Vol 6, No. 1 (1970), pp 1-19; W. Beck, E.J. Jankowski, and P. Fisher, *Hydrogen Stress Cracking of High-Strength Steels*, NADC-MA-7140 (Naval Air Development Center, 1971); and *Hydrogen Embrittlement Testing*, ASTM STP543 (American Society for Testing and Materials [ASTM], 1974).

⁴G. Schwen, G. Sachs, and K. Tonk, *ASTM Proceedings*, Vol 57 (1957), pp 682-697; W. Beck, *Electrochemical Technology*, Vol 2 (1964), pp 74-78; and J.D. Harrison and G.C. Smith, *British Welding Journal*, Vol 14 (1967), pp 493-502.

⁵W.A. Spitzig, P.M. Talda, and R.P. Wei, "Fatigue-Crack Propagation and Fractographic Analysis of 18 Ni (250) Maraging Steel Tested in Argon and Hydrogen Environments," *Engineering Fracture Mechanics*, Vol 1 (1968) pp 155-165.

⁶C.A. Zaffe, *Journal of Iron and Steel Institute*, Vol 154, No. 123 (1946).

⁷A.S. Tetelman and A.J. McEvily, Jr., *Fracture of Structural Materials* (John Wiley, 1967).

⁸N.J. Petch, "The Ductile Fracture of Polycrystalline Iron," *Philosophical Magazine*, Vol 1 (1956), pp 186-191.

⁹A. Troiano, "The Role of Hydrogen and Other Interstitials in the Mechanical Behavior of Metals," *Transactions of The American Society for Metals (ASM)*, Vol 52 (1960), p 52.

Troiano hypothesizes that hydrogen in the stressed region of the atomic lattices near the voids gives up its electrons to the third subshells of the host atoms, filling the vacancies in the third band, and thereby decreasing the binding energy or cohesiveness of the atoms in the lattice in this region. One flaw in this theory is that specimens slowly cooled from a hydrogen atmosphere or cathodically charged at room temperature contain cracks even without externally applied stress. The supposition that hydrogen segregates to stressed regions in the metal is also inconsistent with the diffusion data of Hill¹⁰ which indicate that little or no strain occurs while hydrogen diffuses.

It should be noted that the deleterious effects associated with hydrogen embrittlement can be removed by outgassing or "baking" the material for a short time in a temperature range of 100°C-300°C.¹¹

Temper Embrittlement

One problem associated with heat-treating certain steels is temper embrittlement which occurs when certain commercial-purity steels are heated in or slowly cooled through the temperature range of 550°C to 350°C.¹² If the steel is subsequently reheated above 600°C for a short time and quenched to room temperature, the embrittlement disappears.

Temper embrittlement is manifested by a loss in corrosion resistance and a large, upward shift in the brittle to ductile transition temperature.¹³ This reduction in toughness seriously limits the use of alloy steels in heavy sections such as pressure vessels and steam turbine rotors.

It is generally believed that the equilibrium segregation of various impurities to prior austenite grain boundaries is the fundamental mechanism of temper embrittlement.

¹⁰M.N. Hill and E.W. Johnson, *Transactions of the American Institute of Mining, Metallurgical and Petroleum Engineers (AIME)*, Vol 215, No. 717 (1959).

¹¹A.S. Tetelman and A.J. McEvily, Jr., *Fracture of Structural Materials* (John Wiley, 1967).

¹²J.R. Low, Jr., *Fracture of Engineering Materials* (ASM, 1964), p 127; and C.J. McMahon, Jr., *Temper Embrittlement in Steel*, ASTM STP 407 (ASTM, 1968), p 127.

¹³*Heat Treating, Cleaning, and Finishing*, ASM Metals Handbook, Vol 2, 8th Edition (1964), p 245; and R.T. Ault, R.B. Holtmann, and J.R. Myers, *Heat Treatment of a Martensitic Stainless Steel for Optimum Combination of Strength, Toughness, and Stress Corrosion Resistance*, Technical Report AFML-TR-68-7 (Air Force Materials Laboratory, April 1968).

¹⁴J.R. Low, Jr., D.F. Stein, A.M. Tuskalo, and R.P. Lafarci, *Transactions of AIME*, MT6TB, Vol 242 (1968), pp 14-24.

tlement. Low and his associates¹⁴ demonstrated the influence of specific impurities such as antimony, tin, phosphorus, and arsenic and alloying elements such as nickel and chromium in promoting embrittlement. Marcus and Palmberg¹⁵ found that when fracture occurs along prior austenite grain boundaries in low-alloy steels, significant amounts of antimony, tin, and phosphorus (100 to 500 times the bulk concentration) are present on the grain boundaries. The presence of both nickel and chromium leads to more segregation of antimony, tin, or phosphorus to the grain boundaries than when either is present alone.

Recent experiments by Ohtani¹⁶ suggest that a central feature of temper embrittlement is the redistribution of solute during carbide precipitation. The study showed that eliminating carbide precipitation in antimony- and phosphorus-doped alloys eliminated the remaining embrittlement resulting from equilibrium segregation. Ohtani concludes that embrittlement is caused by the presence of impurities in the carbide-ferrite interfaces resulting from piling-up of the impurity ahead of a growing carbide.

Regardless of how impurities reach the grain boundaries, it is generally accepted that they lower the maximum cohesive force along the prior austenite grain boundaries. Consequently, cracks can easily propagate along this path.

Welding of Steel

Welding is an important method of joining single members into complex structural systems required to function under diverse loading conditions in construction engineering. Arc welding has been widely used to join various constructional alloy steels. In the arc welding process, the arc supplies the heat needed to melt the filler and base metal surfaces being joined. Even when the proper electrodes, heat input, and weld techniques are used,¹⁷ weld deposits are rarely free of discontinuities; many types of defects occur, including porosity, lack of fusion (LOF), lack of penetration (LOP), cracks, undercuts, inclusions, and burn-through.

¹⁵H.L. Marcus, Jr. and P.W. Palmberg, "Effect of Solute Elements on Temper Embrittlement of Low Alloy Steels," *Temper Embrittlement of Steels*, ASTM STP 499 (ASTM, 1971), pp 90-103.

¹⁶H. Ohtani, H.C. Feng, and C.J. McMahon, Jr., "New Information on the Mechanism of Temper Embrittlement of Alloy Steels," *Metallurgical Transactions*, Vol 5 (1974), pp 516-518.

¹⁷A. Phillips, ed., *The Welding Handbook*, Vol 1 (American Welding Society, 1968).

The effects of these defects on the mechanical properties of the joint differ. Factors such as size, shape, orientation, distribution, and service environment also play important roles in determining the performance of a weldment.

Porosity, one of the most frequent weld defects, is formed by entrapment of evolved gases in the solidifying metal. Because of their reduced solubility, the gases are driven from solution in the weld metal as the temperature drops. Gas bubbles are formed at the solid-liquid interface and remain there until they are large enough to float through the molten metal and escape to the atmosphere.¹⁸ If the rate of flotation is less than the rate of the solidifying front's advance, the bubbles are trapped, creating porosity.

LOP defects result when the weld and base metals (or the base metal alone if no filler metal is used) do not integrally fuse at the root of the weld. This occurs when the weld metal fails to reach the root of a fillet weld or the root face of a groove weld fails to reach fusion temperature along its entire length.

LOF occurs when adjacent layers of weld metal, or weld metal and base metal, fail to fuse because the temperature of one of the metals does not reach its melting point during a weld pass.

¹⁸D. Warren and R.D. Stout, *Welding Journal*, Vol 3, No. 8, Research Support 381-S (1952).

2 EXPERIMENTAL PROCEDURE

Materials

The steels used in this investigation were 3/4 in. thick plates of ASTM A-36, ASTM A-517 Grade F (USS T-1), and HY-130. Type A-36 is the most common grade of structural steel used in bridges and buildings and for other general structural purposes. Its microstructure (Figure 7) consists of regions of ferrite and pearlite. Type A-517 Grade F structural steel (USS T-1) is a high-strength, low-alloy, quenched and tempered steel used in such applications as welded bridges, buildings, and pressure vessels. HY-130 is also a low-carbon, quenched and tempered alloy steel with a high yield strength. This steel has high toughness and adequate hardenability even for thick plate applications. The tempered martensitic microstructures of T-1 and HY-130 are shown in Figures 8 and 9.

T-1 steel weldments were fabricated using AIRCO AX 110 welding wire. The chemical compositions of the steels and weld metal are shown in Table 1; Table 2 lists their mechanical properties.

Welding Procedure

The gas-metal arc (GMA) welding process was used to prepare the T-1 steel weldments. The weld passes were deposited in either a 60° double-V groove or a single-V groove (Figure 10). Table 3 gives the welding parameters.

Table 1
Chemical Composition of Steels and Weld Metal

Steel Compositions %	ASTM A-36	ASTM A-517 Grade F (T-1)	AX110 weld deposit	HY130**
C	0.26 max	0.10-0.20	0.085 max	0.12 max
Mn	0.85-1.35*	0.60-1.00	1.23 max	0.60-0.90
P	0.04 max	0.035 max	0.011 max	0.010 max
S	0.05 max	0.04 max	0.010 max	0.015 max
Si	0.15-0.30*	0.15-0.35	0.42 max	0.20-0.35
Cu	0.20	0.15-0.50	—	—
Ni	—	0.70-1.00	2.29 max	4.75-5.25
Ti	—	—	0.009 max	—
Cr	—	0.40-0.65	0.16 max	0.40-0.70
Mo	—	0.40-0.60	0.52 max	0.30-0.65
V	—	0.03-0.08	0.0094 max	0.05-0.10
B	—	0.002-0.006	—	—
Al	—	—	0.005 max	—

*For shapes over 426 lb/ft (633.96 kg/m).

**Data provided by U.S. Steel.

Table 2
Mechanical Properties of Steels and Weld Metal

Steel	Yield Strength (ksi) (0.2% offset)	Tensile Strength (ksi)	Elong (% in 2 in. or 5.08 cm)
A-36	32-36 min. (22498240-25310520 Kg/m ²)	58-80 (40778060-56245600 Kg/m ²)	21-23 min.
T-1	100 min. (70307000 Kg/m ²)	115-135 (80853050-94914450 Kg/m ²)	18 min.
AX-110 weld deposit	100 min. (70307000 Kg/m ²)	115-135 (80853050-94914450 Kg/m ²)	20 min.
HY-130	130 min. (91399100 Kg/m ²)	150-180 (105460500-12655260 Kg/m ²)	15 min.

Table 3
Welding Parameters

Voltage	Amperage	Travel Speed (in./min)	Preheat & Interpass temp.
220V	350 amp	12 (30.48 cm/min)	93°C
Shielding Gas	Heat Input (kJ/l)	No. of Weld Passes	
2% Oxygen-Argon	60-65	4	

Normal welding procedures were intentionally disturbed to obtain the desired weld discontinuities. Clustered porosity was produced by shutting off the shielding gas, thereby contaminating the molten weld metal in the root of the joint with oxygen. Isolated porosity was introduced by shutting off the oxygen in the shielding gas, thus decreasing arc stability.

LOP was created in a double-V groove plate by butting the lands tightly together to prevent complete penetration of the weld metal. Using a single pass on each side resulted in excessive distortions; to correct this, the specimens were welded using two alternate passes on each side. The LOP was a planar, centrally located defect extending the full length of the weld.

LOF was produced by lowering the heat input 90 percent on the first pass.

Each weldment was radiographed to verify the existence of the desired defects.

Specimen Fabrication and Testing

Figures 11 and 12 show the specimen geometries for the tensile, impact, and fatigue tests. The tensile and fatigue plate specimens were machined with their longitudinal axes parallel to the rolling direction, while the longitudinal axes of the impact specimens were perpendicular to the rolling direction. The weldment specimens were machined with their longitudinal axes perpendicular to the weld axis.

The mechanical tensile tests were conducted at room temperature at a constant strain rate of 0.001 in./in./min (0.001 cm/cm/min). To determine the effect of temperature on the fracture mode of the Charpy specimens, tests were conducted at a wide range of temperatures (Table 4) using a temperature control bath. The fatigue tests were conducted at 10 cycles/sec in a tension-tension sinusoidal mode at room temperature, using a 50-kip MTS unit. All fatigue and tensile tests of the defective weldments were conducted perpendicular to the weld axis.

Table 4
Temperatures and Environments of Charpy Tests

Temp °C	Environment
-196	Liquid Nitrogen
-83	Dry Ice/Ethyl Alcohol
-18	Ice/Salt Water
23	Ambient

Hydrogen Embrittlement

To induce hydrogen embrittlement, the machined samples were cathodically charged in a solution of 10 weight percent (w/o) H_2SO_4 and 0.3 w/o As_2O_3 . The As_2O_3 was used to promote penetration of hydrogen during cathodic polarization. The cathodic charging was conducted at a current density of 6 mA/sq in. ($.93 \text{ mA/cm}^2$) for 12 hours prior to testing.

Temper Embrittlement

The T-1 specimens were temper-embrittled using the following step-cooling procedure:¹⁹

1. Temper 1 hour at 593°C .
2. Furnace-cool to 538°C and temper for 15 hours.
3. Furnace-cool to 524°C and temper for 24 hours.
4. Furnace-cool to 496°C and temper for 48 hours.
5. Furnace-cool to 468°C and temper for 72 hours.
6. Furnace-cool to 315°C .
7. Air-cool to room temperature.

The HY-130 specimens were temper-embrittled using the following procedure:²⁰

1. Temper 1 hour at 593°C .
2. Furnace-cool to 515°C and temper for 16 hours.
3. Furnace-cool to 502°C and temper for 24 hours.
4. Furnace-cool to 468°C and temper for 96 hours.
5. Furnace-cool to 452°C and temper for 144 hours.
6. Furnace-cool to 441°C and temper for 168 hours.
7. Furnace-cool to 344°C .
8. Air-cool to room temperature.

3 RESULTS AND DISCUSSION

The summary of the tests conducted in this study, typical tensile test load-deflection curves, the variation in absorbed energy with temperature for Charpy tests, and the fatigue lives of unembrittled and embrittled steels are shown in Figures 13 and 14 and Tables 5 and 6.

ASTM A-36

The tensile fracture surface of the A-36 steel is shown in Figure 15. Considerable necking occurred in the sample prior to fracture. The mechanism of failure was dimple rupture. Figure 16 shows both considerable

variation in dimple size and an entrapped inclusion. Figure 17 shows plastic deformation markings within the large concave dimples.

The effect of hydrogen embrittlement on the strength of ferritic steels is minimal due to the difficulty in propagating a crack through the ductile material. In this investigation, the hydrogen-embrittled tensile sample exhibited a dramatic loss in ductility. The fracture surface (Figure 18) consisted of a mixture of flat quasi-cleavage facets (Figure 19) and concave inclusion-nucleated dimples (Figure 20). It is postulated that the serpentine glide markings shown on the left side of Figure 20 were caused by the appearance of new free surfaces resulting from glide on a series of nearly parallel planes. As straining continued, the distinct glide planes were smoothed out and ripples formed. Formation of these smooth features has been called glide plane decohesion or ductile cleavage.²¹

Since temper embrittlement manifests itself in Charpy impact tests by raising the brittle-to-ductile transition temperature,²² it is quite easy to determine if this phenomenon is present. Charpy tests were performed on A-36 specimens after they received a heat treatment similar to the HY-130 specimens. Since there was no change in the absorbed energy of these samples as compared to the as-received samples, it was concluded that A-36 steel was not susceptible to temper embrittlement, and no further studies of this phenomenon were made with this material.

The fracture surface of the A-36 specimen broken in fatigue (Figure 21) consisted of a fatigue zone and a tensile overload zone. Distinct fatigue striations can be seen in Figure 22. Most of these striations were parallel to the machined notch, although secondary crack fronts were occasionally observed. Stereo photographs of the fatigue zone (Figure 23) show that the crack front propagated on many different levels. The central portion of the fracture surface, where rapid tensile overload occurred, consisted of equiaxed dimples generated by inclusions (Figure 24).

²¹Fractography and Atlas of Fractographs, ASM Metals Handbook, Vol 9, 8th Edition (American Society for Metals [ASM], 1974), p 81.

²²Heat Treating, Cleaning, and Finishing, ASM Metals Handbook, Vol 2, 8th Edition (1964), p 245; and R.T. Aul, R.B. Holtmann, and J.R. Myers, Heat Treatment of a Martensitic Stainless Steel for Optimum Combination of Strength, Toughness, and Stress Corrosion Resistance, Technical Report AFML-TR-68-7 (Air Force Materials Laboratory, April 1968).

¹⁹A. Joshi and D.F. Stein, Temper Embrittlement of Alloy Steels, ASTM STP 499 (ASTM, 1972), pp 39-39.

²⁰Personal communication with R.A. Swift, January 1973 concerning Temper Embrittlement Study of Hy-130 Steel.

Table 5
Summary of Tests Conducted in This Study

Material	Mode of Test								
	Tensile			Fatigue			Impact		
	As- Rec.	H ₂ Embr.	Temper Embr.	As- Rec.	H ₂ Embr.	Temper Embr.	As- Rec.	H ₂ Embr.	Temper Embr.
A-36 Plate	X	X	X	X	X		X		X
T-1 Plate	X	X	X	X	X	X	X		
HY-130 Plate	X	X	X	X	X	X	X		
T-1 Weld	X	X	X	X	X	X	X		
T-1 Weld w/Defects	X	X	X	X	X	X			

Table 6
Summary of Fatigue Test Parameters and Data*

Material	Fatigue Life (# of cycles)			Specimen Shape	Applied Stress (ksi)	
	As Received	Hydrogen-Embrittled	Temper-Embrittled		Max	Min
A-36	6600	4575	3800	flat	36 (25310520 Kg/m ²)	4 (2812280 Kg/m ²)
T-1	6050	3470	5417	flat	100 (7030700 Kg/m ²)	15 (10546050 Kg/m ²)
HY-130	11560	4410	7750	round	134 (94211380 Kg/m ²)	18 (12655260 Kg/m ²)
AX-110 weld	5510	4135	5110	flat	100 (7030700 Kg/m ²)	15 (10546050 Kg/m ²)

*Each value is an average of two or more tests.

The fracture surface of the hydrogen-embrittled fatigue specimen (Figure 25) has a woodier appearance than the unembrittled specimen. A high magnification of the fatigue zone revealed well-developed fatigue striations (Figure 26). A stereo view of this region (Figure 27) showed wider secondary cracking than in the unembrittled specimen; this may explain the difference in appearance. Large dimples were present in the tensile overload region of the fracture surface (Figure 28).

Figure 29 shows the fracture surface of an A-36 Charpy specimen broken at -196°C. A higher magnification of this surface (Figure 30) shows that failure occurred by cleavage. The river patterns (Figure 31)

show the direction of crack propagation within each cleavage facet. When the Charpy specimen was fractured at -83°C, the fracture surface (Figure 32) consisted of cleavage facets and microvoids (Figure 33), indicating that failure occurred by transgranular cleavage and microvoid coalescence. When fracture occurred at -18°C, the fracture surface (Figure 34) became more complex. Near the notch, failure occurred by dimple rupture (Figure 35); in the central portion of the specimen, failure occurred by cleavage and dimple rupture (Figure 36). The increasing amount of plastic strain at the crack tip during fracture accounts for the sudden increase in the amount of energy which must be expended to cause failure. The transition temperature of A-36, based on the average energy criterion²³ (i.e., the

temperature corresponding to an energy that is one-half the difference between the maximum and minimum energies), is approximately 10°C.

Fracturing at room temperature results in a prominent shear lip at the end of the specimen, as well as considerable tearing near the notch (Figure 37). Failure is by dimple rupture near the notch (Figure 38) and cleavage in the central region (Figure 39). The dimple rupture results from microvoid coalescence and inclusion-generated voids (Figure 40). The central region exhibits regions of this failure mode interspersed among the cleavage facets (Figure 41).

The central cleavage in an otherwise ductile Charpy specimen, called a window of fast fracture, results from transition from the plane stress to the plane strain fracture mode as the crack progresses through the specimen. A three-dimensional stress state (constraint) exists in the center of the specimen, resulting in the yield stress being increased to up to three times its normal value. In addition, the yield stress is further increased by the low test temperature (yield stress is inversely proportional to temperature). Consequently, before plastic deformation at the crack tip can occur, the stresses in the center must increase to a value much greater than the normal yield stress of the material. At the edges of the specimen, however, only a two-dimensional stress state is possible, so plastic deformation can occur more easily.

At very low temperatures (-196°C), the yield stress is so high that cleavage fracture occurs even along the edges of the specimen. At room temperature, however, the yield stress is so low that even the constraint factor cannot increase it enough to provide cleavage; fracture therefore occurs by dimple rupture throughout the specimen.

ASTM A-517 Grade F (USS T-1) Steel

The fracture surface resulting from tensile failure of T-1 steel plate (Figure 42) contained dimples (Figure 43). Failure in the center of the specimen occurred by normal rupture which produced equiaxed dimples, while the outer edges failed by shear rupture. A higher magnification (Figure 44) shows that the equiaxed dimples formed around inclusions which were still

present in the dimples, indicating that inclusion fracture initiated failure.

Hydrogen-charging T-1 steel before fracturing in tension failed to produce any noticeable effect, probably due to lack of diffusion time for the hydrogen. The fracture surface (Figure 45) seems identical to the unembrittled surface (Figure 42). Failure occurred by dimple rupture (Figure 46) and microvoid coalescence in both cases. Secondary microcracks formed as a result of voids joining. While hydrogen embrittling did not affect the ultimate strength of the material, it did result in a minor loss in ductility evidenced by a smaller area under the load/deflection curve (Figure 13).

When T-1 steel was subjected to temper embrittlement, the tensile fracture surface (Figure 47) consisted entirely of dimple rupture and microvoid coalescence (Figures 48 and 49). Although this is identical to the failure mode of the as-received specimen, it does not mean that the steel was not embrittled. Schultz and McMahon²⁴ found that temper embrittling an alloy with composition similar to that of T-1 steel by step-cooling produced the same type of failure mode. They verified the presence of embrittlement by observing the corresponding increase in the transition (from brittle to ductile) temperature. Since the fracture surface alone is not sufficient to identify the presence of embrittlement, further tests such as the Charpy impact test should be performed to verify its presence.

The fracture surface of an unembrittled double-notched T-1 plate specimen broken in fatigue (Figure 50) consisted of a fatigue zone near each notch and a region of tensile overload in the center of the specimen. The striations in the fatigue zone (Figure 51) were initiated parallel to the machined notch; however, secondary cracking began near the tensile overload region, and the striations became multi-directional (Figure 52). The small holes resulted from large inclusions which were pulled from the matrix as the fatigue crack advanced. A cracked inclusion remains at the bottom of one of the holes. The tensile overload region (Figure 53) consisted of equiaxed dimples of varying sizes.

Introduction of excessive hydrogen in the T-1 steel by cathodic charging reduced the fatigue life between 20 and 60 percent (Table 5). The fracture surface of a hydrogen-embrittled T-1 plate specimen broken in

²³A.S. Tetelman and A.J. McEvily, Jr., *Fracture of Structural Materials* (John Wiley, 1967).

²⁴B.J. Schultz and C.J. McMahon, Jr., *Temper Embrittlement of Alloy Steels*, ASTM STP 499 (ASTM, 1972), pp 104-135.

fatigue (Figure 54) was also composed of fatigue regions near the notches and a tensile overload region. The fatigue region, however, was not flat, but consisted of parabolic contours (Figure 55). Photographing these contours at different tilt angles revealed that the parabolic contours were actually craters in the fracture surface (Figures 56 and 57). The shape of the craters can be seen in the optical micrograph (Figure 58) taken from a section in the fatigue zone perpendicular to the machined notch. Many of these craters contained cracks in the bottom perpendicular to the machined notch. Failure occurred by quasi-cleavage inside the craters, while considerable secondary cracking outside resulted in multi-directional fatigue striations. There were no fatigue striations evident near the notch.

The formation of craters in the hydrogen-embrittled fatigue-fractured samples can be explained using Troiano's theory of hydrogen embrittlement.²⁵ He proposed that accumulation of hydrogen followed by subsequent crack nucleation occurred in regions of high triaxial stress. A triaxial stress state occurs below the root of a notch where cracks can initiate as a result of a critical combination of stress and hydrogen concentration. Since fatigue striations were present in the unembrittled samples, it was assumed that the absence of striations near the notch in the embrittled samples indicated that subsurface crack nucleation had occurred instead of the progressive type of crack advance from the outside surface of the notch as evidenced in the A-36 specimens and the unembrittled T-1 specimens. Subsurface fatigue cracks nucleated - microcracks, voids, or inclusions grow on planes perpendicular to the major applied stress axis. When these transverse fatigue cracks intersect the longitudinal cracks associated with stringers, subsequent cyclic stressing enlarges the cracks into craters. Figure 59, a longitudinal section of the hydrogen-embrittled fatigue zone, illustrates the beginning and intermediate stages of crater formation. Widening of the longitudinal microcracks by the main fatigue crack is clearly evident.

The central portion of the fracture surface, where tensile overload occurred, consisted of various-sized dimples and occasional void-generated secondary cracks (Figure 60). The absence of hydrogen embrittlement effect in this region was probably because failure was very rapid, giving the hydrogen insufficient time to build up to a critical concentration in the area.

²⁵A. Troiano, "The Role of Hydrogen and Other Interstitials in the Mechanical Behavior of Metals," *Transactions of The American Society for Metals (ASM)*, Vol 52 (1960), p 52.

The temper-embrittled T-1 fatigue fracture surface (Figure 61) contained a large amount of lamellar tearing in the fatigue zone (Figure 62). Although a small amount of tearing was noticed in the as-received fatigue sample, temper embrittlement seemed to render the material more susceptible to lamellar tearing. It is believed that the heat treatment cycle reduces the material's short transverse tensile properties so that as the fatigue crack propagates, the large triaxial stresses which build up ahead of the crack front fracture the weakened interface between the matrix and the long stringers of inclusions. As in the unembrittled sample, fatigue striations were parallel to the machined notch (Figure 63). Figure 62 clearly shows the transition from a fatigue to a tensile overload failure mode. As in the previous cases, the central region consisted of dimple rupture (Figure 64).

When a T-1 Charpy specimen was fractured at -196°C (Figure 65), failure was entirely by cleavage (Figure 66). River patterns (Figure 67) show the direction of crack propagation across each cleavage facet. When the specimen was broken at -83°C (Figure 68), mixed mode failure occurred by cleavage (Figure 70). As with the A-36 samples, the onset of dimple formation on the fracture surface corresponded directly with the increase in energy needed to cause failure (Figure 14). At -18°C, the fracture surface (Figure 71) exhibited a "woody" fracture and consisted entirely of dimples (Figure 72), indicating that failure resulted from microvoid coalescence. The fracture surface of a Charpy specimen broken at room temperature (Figure 73) also consisted of dimples of varying sizes (Figure 74). A higher magnification (Figure 75) shows that dimple formation resulted from microvoid coalescence along with inclusions.

HY-130 Steel

Since HY-130 is also a quenched and tempered martensitic steel, its fracture behavior should be similar to that of T-1. Comparing their stress-strain curves (Figure 13) shows that HY-130 is stronger and more ductile than T-1. Because of this high strength, HY-130's susceptibility to hydrogen embrittlement is expected to be severe.

When HY-130 was broken in tension (Figure 76), high magnifications of the fracture surface revealed that failure occurred by normal rupture in the center of the specimen (Figure 77) and shear rupture on edges of the specimen (Figure 78). The large cracks on the fracture surface probably resulted from microcracks which formed at the interface between the martensitic matrix and long stringers of inclusions.

Figure 13 clearly shows the difference in ductility between A-36 and the two martensitic steels. In A-36, more plastic deformation occurred at the crack tip. As a result, the dimples in A-36 steel (Figure 16) were larger than in the T-1 (Figure 43) and HY-130 (Figure 77) steels.

Hydrogen-charging the HY-130 sample prior to fracture significantly affected the appearance of the fracture surface (Figure 79). The surface contained many small, circular, flat regions called "fisheyes" (Figure 80). Stereo photographs of a fisheye (Figure 81) show that the center is actually a deep pit. When fracture initiated from this area, it propagated in a quasi-cleavage mode (Figure 82).

Troiano's theory of hydrogen embrittlement can explain the appearance of the fisheyes. If atomic hydrogen can diffuse to regions of high triaxial stress under an applied load, a critical concentration of hydrogen results. This hydrogen, in conjunction with the applied load, causes localized fracture to occur in a brittle manner. Since the conventional tensile test is fairly rapid, too little time is available for the regular mechanism of hydrogen-induced microcracking to repeat itself at the tip of the newly formed microcrack. Thus, the size of the fisheye is confined to the initial microcrack associated with the cavity. Other portions of the sample failed by grain boundary separation with microvoid coalescence (Figures 83 and 84). A smaller reduction in cross section in the hydrogen-embrittled sample indicated a loss in ductility. This observation was confirmed by the load-deflection curve (Figure 13) which also indicated a loss in ductility due to hydrogen embrittlement.

Considerable lamellar tearing is evident on the fracture surface of a temper-embrittled HY-130 tensile specimen (Figure 85). Failure occurred in a steplike fashion (Figure 86). The failure mode was a combination of slipping, tearing, and microvoid coalescence (Figure 87). Serpentine glide patterns were evident on the fracture surface. As with the T-1 steel, temper embrittlement increased the material's susceptibility to lamellar tearing.

Figures 88 and 89 show the fracture surfaces of round and flat as-received HY-130 specimens fractured in fatigue. The fatigue and overload regions are easily distinguishable in both samples. The fatigue region (Figure 90) consisted of parallel striations indicative of crack front progression across the surface (Figure 91). A stereo micrograph of the fatigue region (Figure 92) shows that the fracture surface is generally flatter than

the A-36 or T-1 fracture surface. The central region, which failed by normal rupture in the center and shear rupture on the sides, consisted of equiaxed and elongated dimples (Figure 93).

The hydrogen-embrittled HY-130 fatigue sample is shown in Figure 94. The fatigue region (Figure 95) differs considerably from the unembrittled fatigue region (Figure 90). The parabolic contour lines on the fracture surface are similar to those on the hydrogen-embrittled T-1 fatigue sample (Figure 55). A stereo photograph of one of these contours (Figure 96) shows that like those on the hydrogen-embrittled T-1 sample (Figure 57), they are deep craters on the fracture surface. The mechanism of formation of these craters in the hydrogen-embrittled HY-130 is postulated to be the same as in the embrittled T-1 steel.

Fatigue striations in the hydrogen-embrittled HY-130 (Figure 97) had multiple orientations on the fracture surface and were usually associated with secondary cracking. The tensile overload region consisted of dimple rupture and microvoid coalescence (Figure 98). Table 5 shows the reduction in fatigue life due to hydrogen embrittlement.

Temper-embrittling HY-130 steel prior to testing in fatigue resulted in the fracture surface shown in Figure 99. The fatigue and tensile overload regions are clearly distinguishable. Since considerably more lamellar tearing occurred than in the as-received specimen broken in fatigue, the embrittlement cycle seemed to increase HY-130's susceptibility to such tearing. At a higher magnification, the fatigue region (Figure 100) was found to contain fatigue striations parallel to the machined notch (Figure 101). A stereo micrograph of the fatigue region (Figure 102) shows that crack propagation occurred on relatively few levels, as in the as-received specimen. In the tensile overload region, failure along the lamellae occurred by slipping, tearing, and microvoid coalescence (Figure 103). A region of intergranular fracture was observed between the fatigue zone and the tensile overload region (Figure 104). Most of the failure in this region was intergranular (Figure 105), presumably along prior austenitic grain boundaries; there were also regions of microvoid coalescence (Figure 106).

The fracture surface of an HY-130 Charpy sample broken at -196°C (Figure 107) consisted solely of cleavage (Figure 108). When failure occurred at -83°C , near the transition temperature, mixed mode fracture occurred (Figure 109). The outer regions consisted of dimple

rupture (Figure 110), while the mechanism of failure in the central region was cleavage (Figure 111). Failure at -18°C , above the transition temperature, resulted in a fracture surface (Figure 112) consisting entirely of dimple rupture (Figure 113). Fracturing at room temperature produced a fracture surface (Figure 114) similar to the -18°C fracture surface (Figure 113). The mechanism of failure was again entirely dimple rupture (Figure 115).

AX-110 Weld

Figure 116 shows the fracture surface of a solid AX-110 weld deposit tested in tension. Failure occurred by microvoid coalescence and dimple rupture (Figure 117). Exposure of an AX-110 weld tensile sample to hydrogen-charging prior to testing produced the fracture surface shown in Figure 118. In one area of the surface small fisheyes were present (Figure 119). The fisheye region (Figure 120) consisted of very small cleavage facets (Figure 121). This failure mode resulted from pockets of entrapped hydrogen gas. The rest of the specimen failed by microvoid coalescence (Figure 122). When the tensile specimens were temper-embrittled prior to testing, the fracture surface (Figure 123) consisted of dimple rupture and microvoid coalescence (Figure 124).

The fracture surface of a solid AX-110 weld tested in fatigue is shown in Figure 125. The fatigue region consisted of parallel microcracks rather than striations (Figure 126). As the crack advanced into the center of the specimen, the failure mode changed from fatigue to tensile overload by microvoid coalescence. When the crack was large enough to cause rapid tensile overload, failure occurred by dimple rupture and microvoid coalescence (Figure 127).

When the weld test specimen was hydrogen-embrittled prior to fatigue testing, the fracture surface (Figure 128) was similar to that of the hydrogen-embrittled T-1 plate specimen (Figure 54), except for the presence of large facets on one side of the weld fracture surface. The fatigue regions consisted of numerous small craters, many of which contained microcracks (Figure 129). Fatigue striations with multiple orientations (Figure 130) were present on the fracture surface around the craters. There was evidence of crater formation even in the central region where failure occurred by dimple rupture and microvoid coalescence (Figure 131).

Temper-embrittling an AX-110 weld fatigue specimen prior to testing produced the fracture surface

shown in Figure 132. The fatigue region (Figure 133) contained relatively few distinct fatigue patterns (Figure 134). There was evidence of lamellar tearing near the transition region from the fatigue to tensile overload failure mode (Figure 135). Failure in the overload region occurred by dimple rupture and microvoid coalescence (Figure 136).

The effects of test temperature on the fracture mode of Charpy specimens revealed the low ductile to brittle transition temperature (DBTT) characteristic of an AX-110 weld. The fracture surfaces resulting from tests conducted at -196°C , -83°C , -18°C , and room temperature are shown in Figures 137 through 140. At -196°C , failure occurred entirely by cleavage (Figure 141). At the transition temperature (-83°C), mixed mode failure occurred; the central region of the specimen failed by cleavage (Figure 142), while the outer areas failed by dimple rupture (Figure 143). At -18°C and above, failure occurred entirely by dimple rupture (Figure 144).

Failure of Defective Weldments

The tensile fracture surface of an AX-110 weldment containing LOP is shown in Figure 145. The LOP area (Figure 146), reveals the vertical machine markings on the base metal plate. The lower half of the fracture surface contained a horizontal line where the fracture mode changed from shear rupture to normal rupture (i.e., the fracture path is normal to the tensile axis) (Figure 147). The area nearest the defect exhibited elongated dimples (Figure 148), while the area nearest the surface consisted of equiaxed dimples (Figure 149). It appears that the crack initiated at the LOP area and propagated toward the surface by shear rupture, with final fracture occurring by normal rupture.

Figure 150 shows the fracture surface of a tensile specimen containing LOP (Figure 151) and LOP (Figure 152). The failure occurred by microvoid coalescence (Figure 153); which defect initiated it is uncertain.

Figure 154 shows the tensile fracture surface of an AX-110 T-1 weldment containing porosity. The interior surface of a porosity bubble revealed dendritic growth patterns and grain boundaries (Figure 155). The fracture of the weld metal, which probably initiated in the porosity region, occurred by microvoid coalescence (Figure 156).

The fracture surface resulting from fatigue fracture of an AX-110 weldment containing LOP is shown in Figure 157. Fracture initiated in the LOP region in the

center of the specimen. Fatigue striations originating from the defect were fairly well developed and easily recognizable (Figure 158). Rapid fracture in the outer portion of the specimen was by dimple rupture (Figure 159).

The fracture surface resulting from fatigue failure of a weldment containing porosity is shown in Figure 160. All the fatigue regions initiated at pores (Figure 161). As the crack propagated through the specimen, the fracture mode changed from fatigue (Figure 162) to dimple rupture (Figure 163).

Hydrogen embrittlement affected the fracture behavior of an AX-110 weldment containing porosity the same way it affected the T-1 plate and sound weld. Large parabolic contours (later confirmed as craters) pointing toward the origin of fracture were apparent on the fracture surface of an AX-110 weldment containing porosity and tested in fatigue (Figure 164). Near the center of the specimen, the craters became more circular (Figure 165). Failure initiated at an outer edge of the specimen (Figure 166). When the propagating crack reached a critical size, catastrophic failure by dimple rupture occurred (Figure 167).

Figure 168 shows the fracture surface resulting from fatigue-failure of a temper-embrittled AX-110 weldment containing LOP. Fatigue initiated from the central defect (Figure 169) and the outside edge of the specimen (Figure 170). No fatigue striations were discernible at the origin, but they became evident as the crack advanced through the material (Figure 171). The peripheral shear lip, where final fracture occurred, exhibited elongated dimples (Figure 172).

4 CONCLUSIONS

1. A-36 steel was found to be susceptible to hydrogen embrittlement, which caused loss in ductility and reduction in fatigue life. Tensile failure in the hydrogen-embrittled specimens occurred mainly by dimple rupture and microvoid coalescence, resulting in the formation of elongated or equiaxed dimples. The fracture surface of the hydrogen-embrittled specimen also contained regions of quasi-cleavage.

2. A-36 steel was found not to be susceptible to the

temper-embrittlement heat treatment performed in this study.

3. The effect of testing temperature on the Charpy specimens was seen in a change from cleavage failure at low temperatures to dimple rupture at room temperature.

4. The fracture surfaces of the as-received and temper-embrittled T-1 (plate and weld) tensile samples were identical. Failure in each case occurred by dimple rupture and void coalescence; therefore, the fracture appearance of tensile specimens is not a dependable method for determining temper-embrittlement.

5. The effect of hydrogen embrittlement was quite severe in quenched and tempered martensitic steels (T-1 and HY-130) tested in fatigue. A significant reduction in fatigue life was observed, and the fatigue regions were found to contain a dispersion of craters. In the hydrogen-embrittled HY-130 and weld samples, small fisheyes which were believed to result from pockets of entrapped hydrogen were evident.

6. Subsurface crack nucleation appears to occur in regions where a critical combination of triaxial stress and hydrogen concentration exists. Transverse cracks, which propagate on a plane perpendicular to the major stress axis, intersect longitudinal cracks formed at matrix-stringer interfaces. Subsequent cycling produces the craters on the fracture surface.

7. Nucleation and propagation of subsurface fatigue cracks in the hydrogen-embrittled samples appear to be responsible for the severe reduction in fatigue life.

8. When fractured in fatigue, the temper-embrittled T-1 plate and, to a lesser extent, T-1 weld were susceptible to lamellar tearing.

9. HY-130 exhibited a markedly increased susceptibility to lamellar tearing when temper-embrittled and tested in tension and fatigue.

10. Fractures of defective welds originated at the internal defect. However, when these specimens were hydrogen-embrittled prior to fatigue testing, failure also originated at an outside free surface.

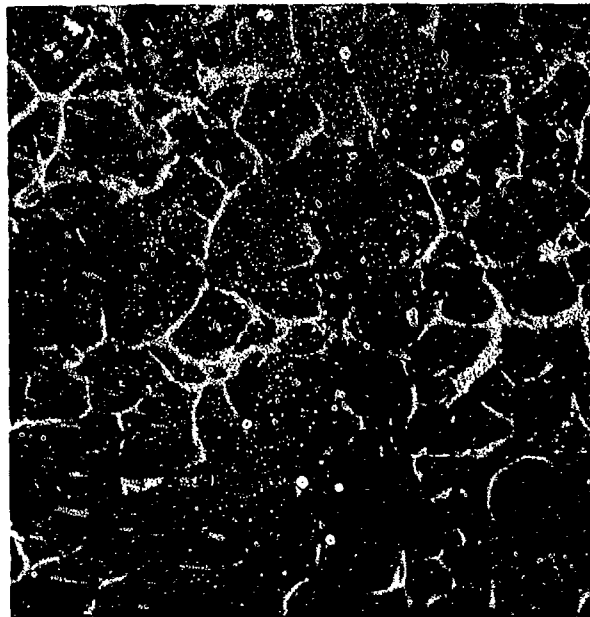


Figure 1. Equiaxed dimples containing inclusions, 4250x.

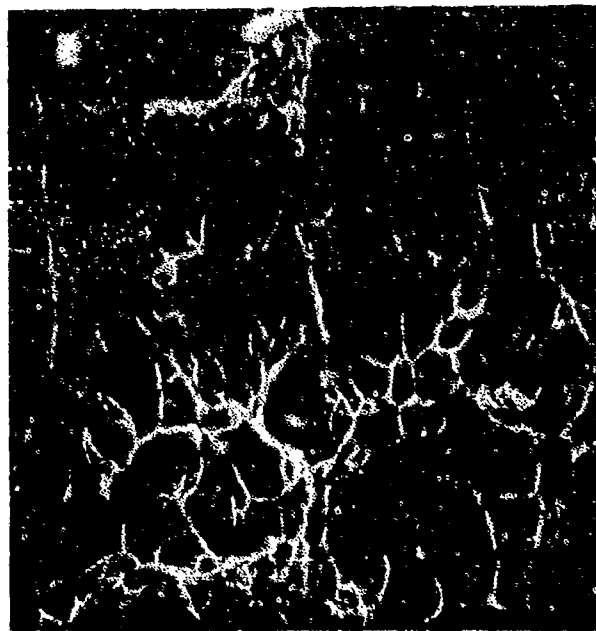


Figure 2. Elongated dimples, 3750x.

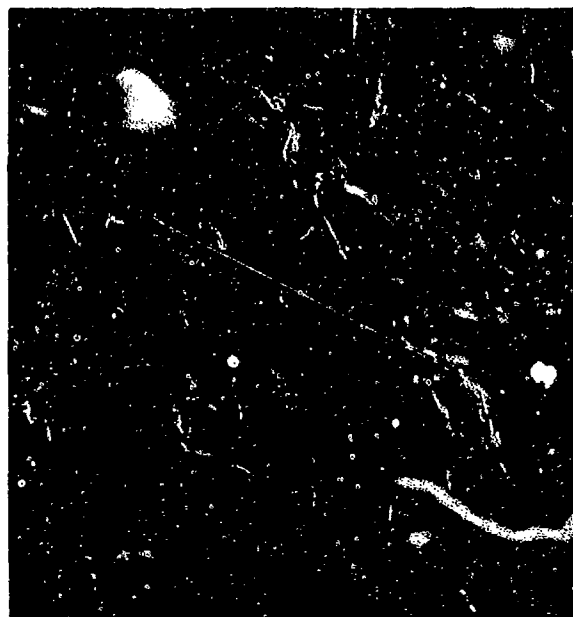


Figure 3. Cleavage facets, 400x.

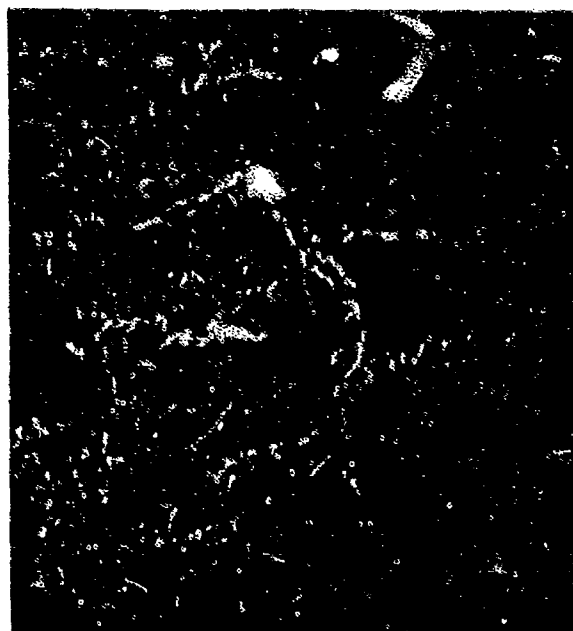


Figure 4. Quasi-cleavage facets, 1600x.

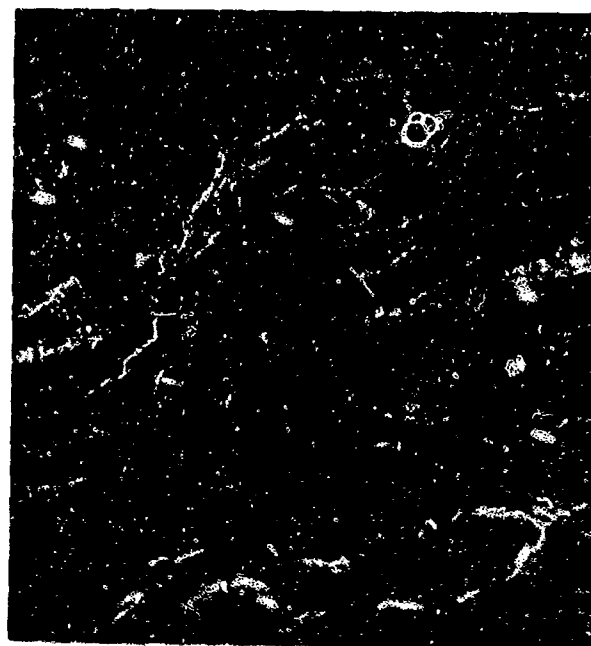


Figure 5. Fatigue striations, 4000x.

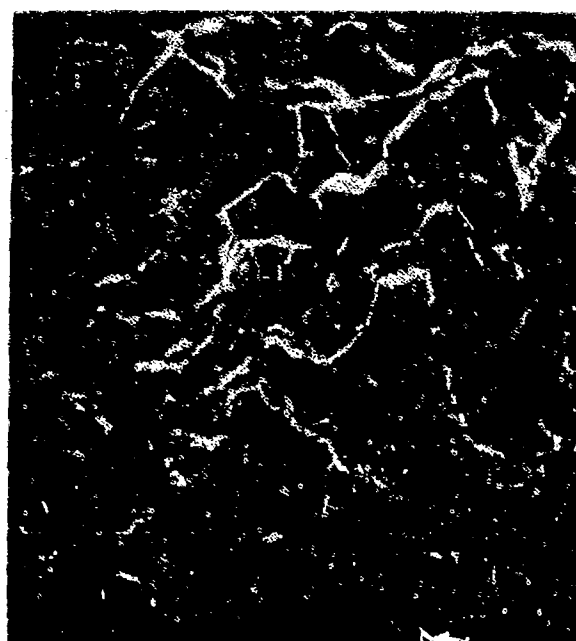


Figure 6. Intergranular fracture, 300x.

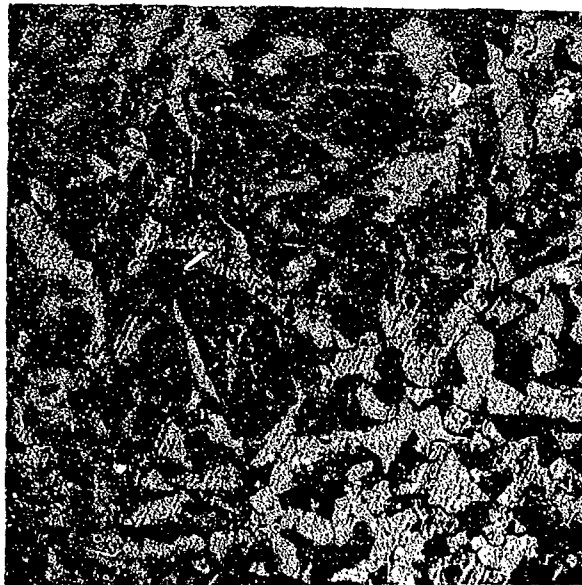


Figure 7. Microstructure of A-36 steel, 200x.

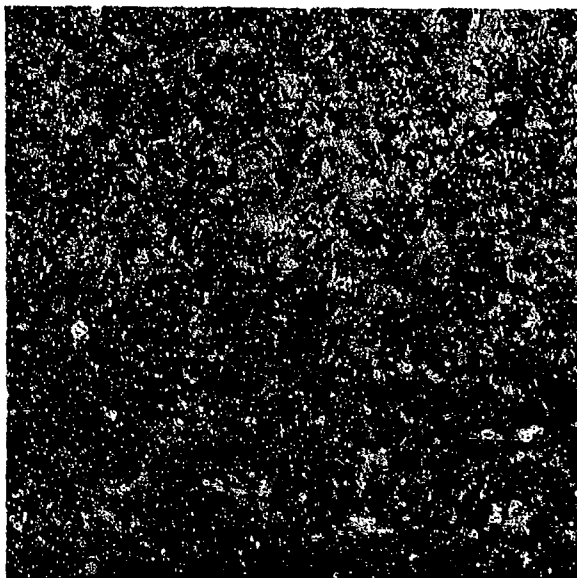


Figure 8. Microstructure of T-1 steel, 200x.

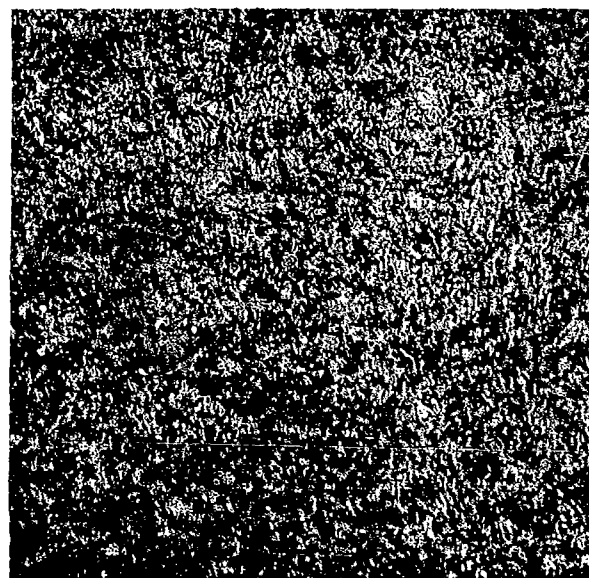
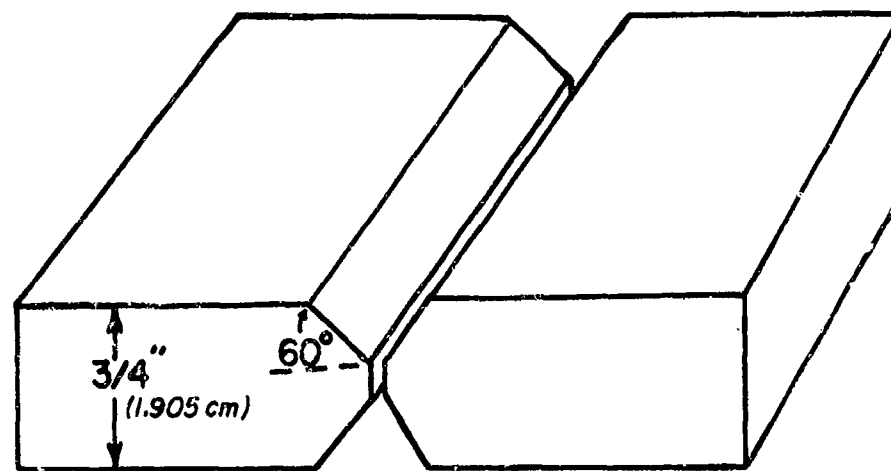
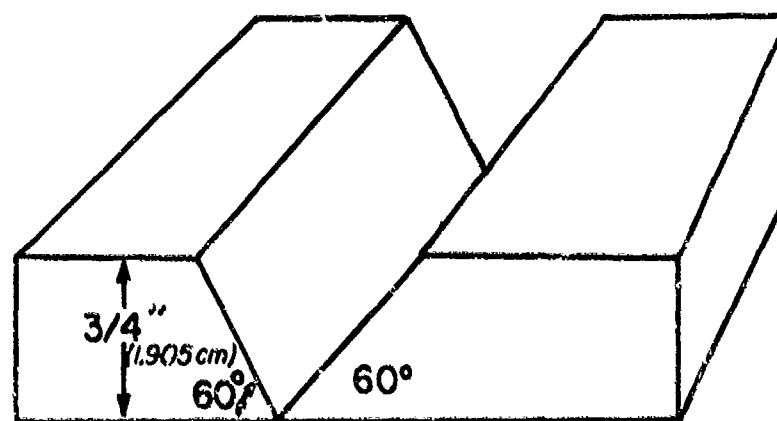


Figure 9. Microstructure of HY-130 steel, 200x.

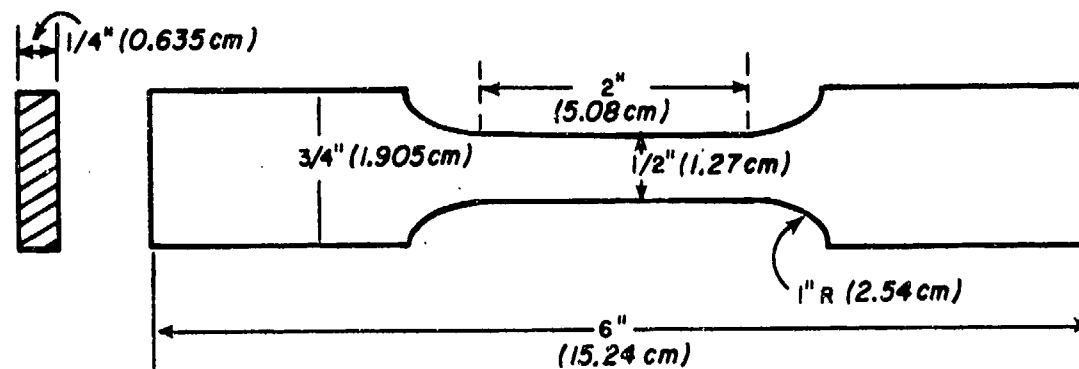


(a) Double Vee Joint

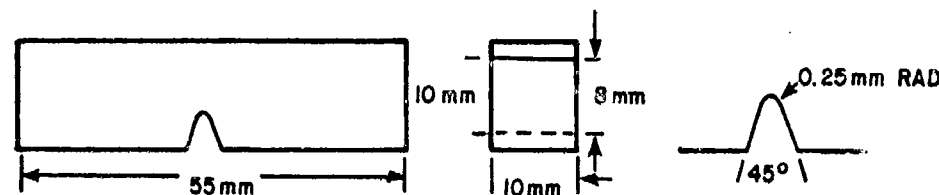


(b) Single Vee Joint

Figure 10. Specimen joints for welding.



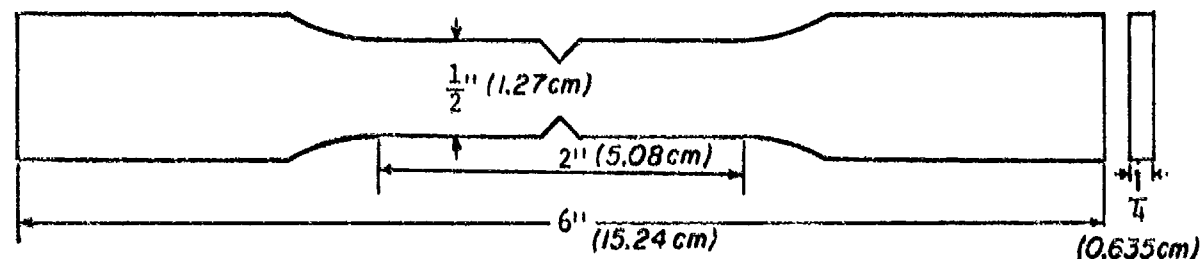
a) Tensile specimen.



b) Charpy specimen.

Figure 11. Specimen geometry for tensile and Charpy impact tests.

Double notch: 45 deg
 $0.01\text{ in. root radius (}0.254\text{ mm)}$
 $1/8\text{ in. deep (}3.175\text{ mm)}$



Single notch: 60 deg
 $1/16\text{ in. deep (}1.59\text{ mm)}$

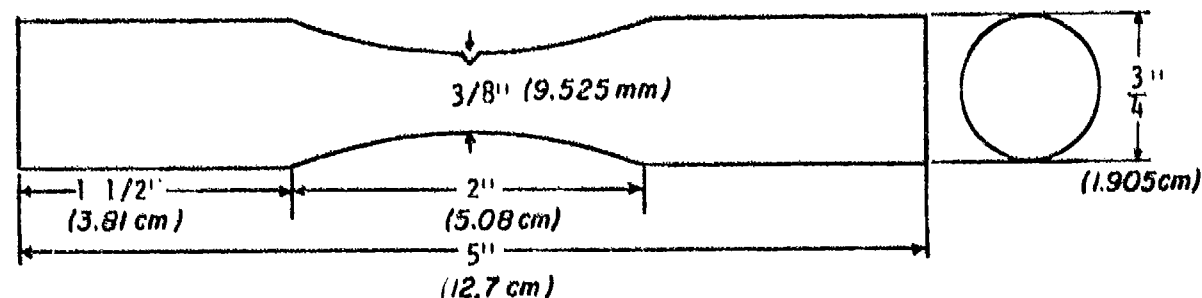


Figure 12. Specimen geometry for fatigue tests.

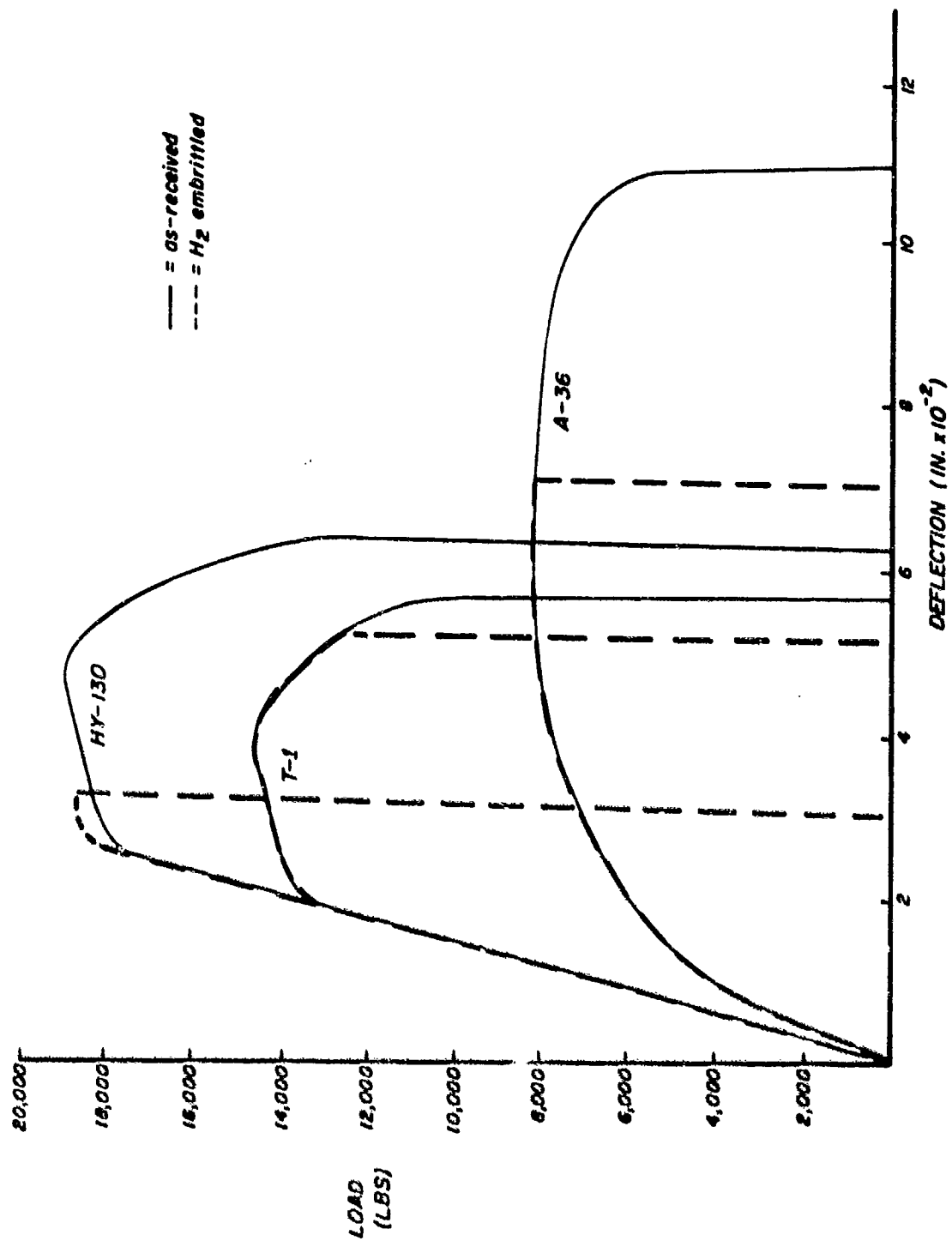


Figure 13. Load-deflection curves for A-36, T-1, and HY-130 steel.

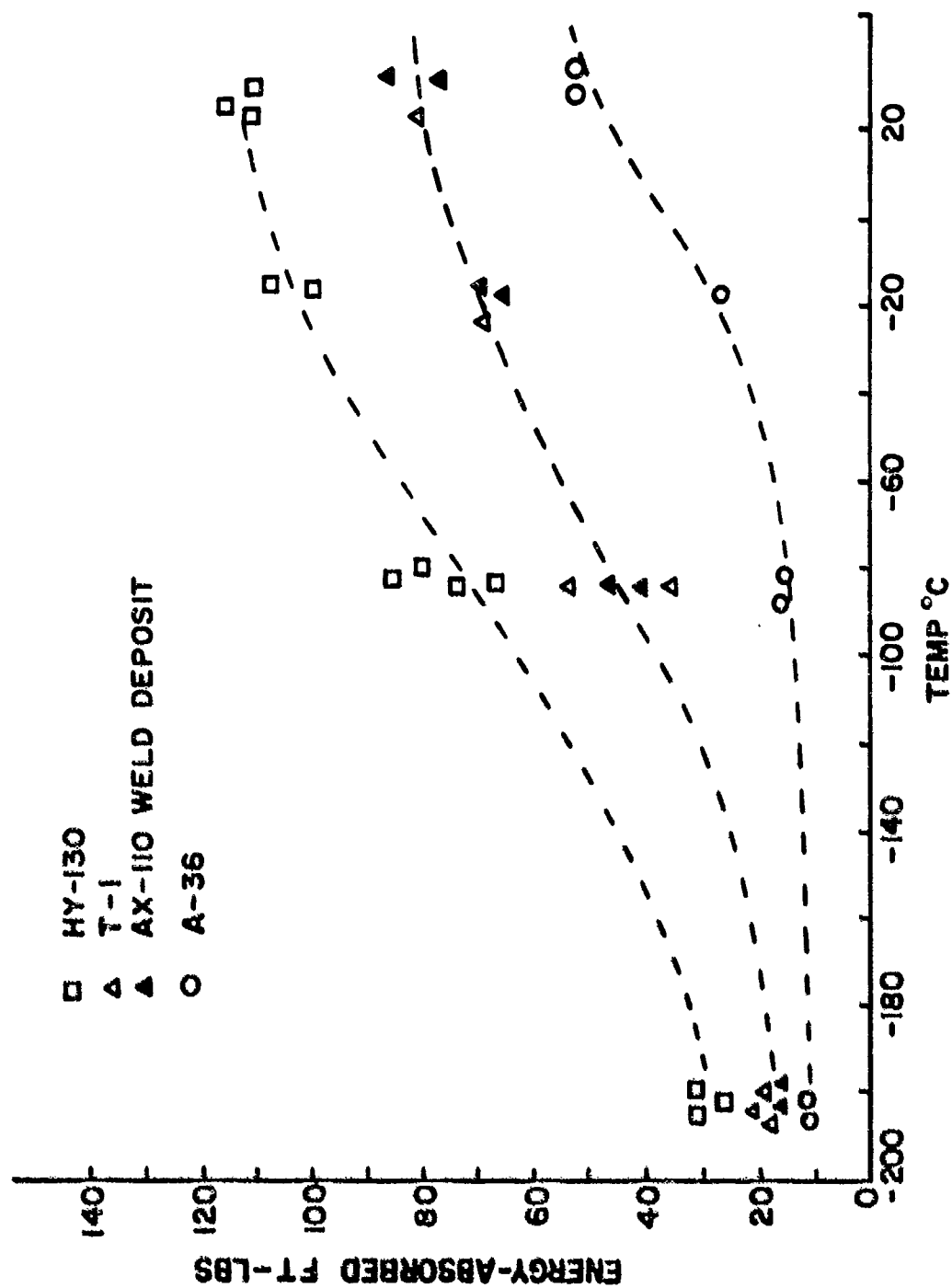


Figure 14. Variation in absorbed energy for A-36, T-1, and HY-130 steel and AX-110 weld deposit.

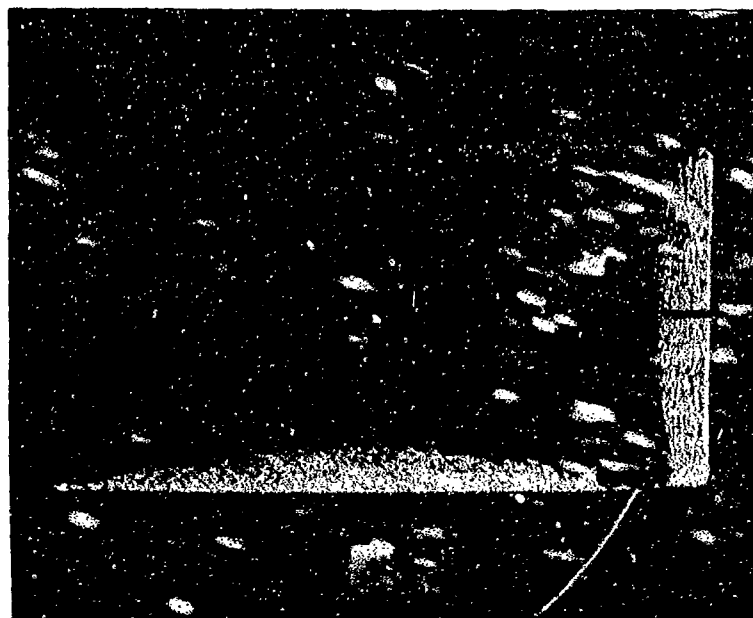


Figure 16

Figure 15. Tensile fracture surface of A-36 steel, 12x.



Figure 17

Figure 16. Dimple rupture in A-36 steel, 1000x.

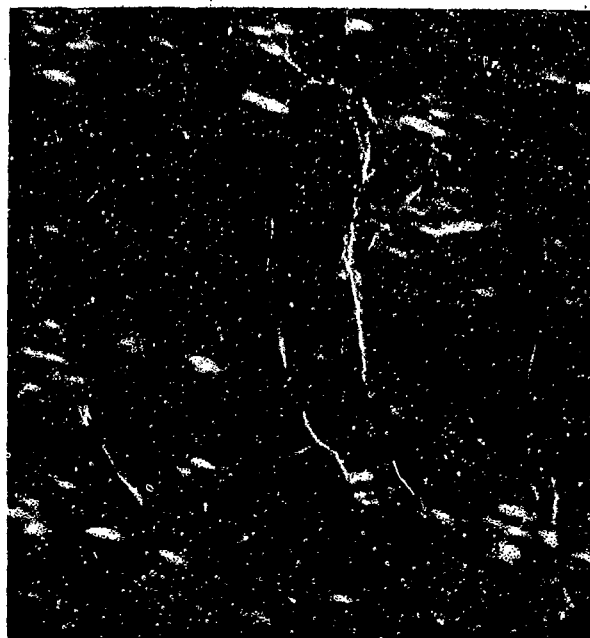


Figure 17. Plastic deformations in dimple rupture in A-36 steel, 3000x.

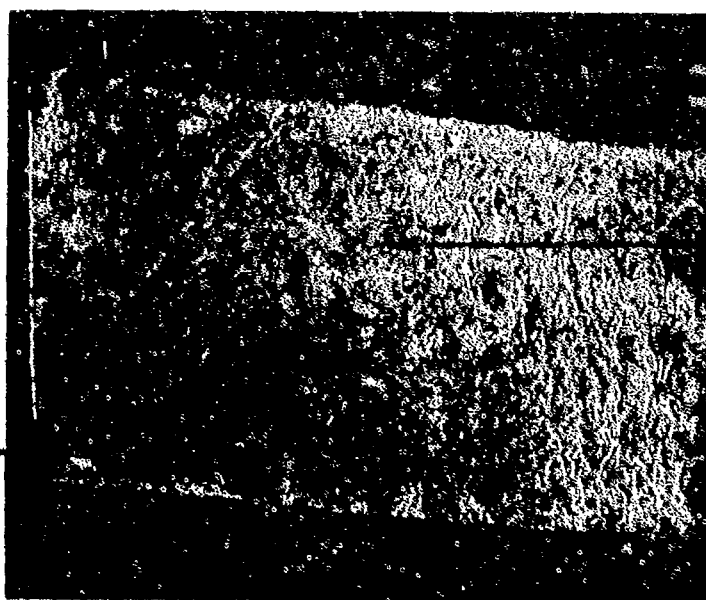


Figure 19

Figure 20

Figure 18. Tensile fracture surface of hydrogen-embrittled A-36 steel, 10x.

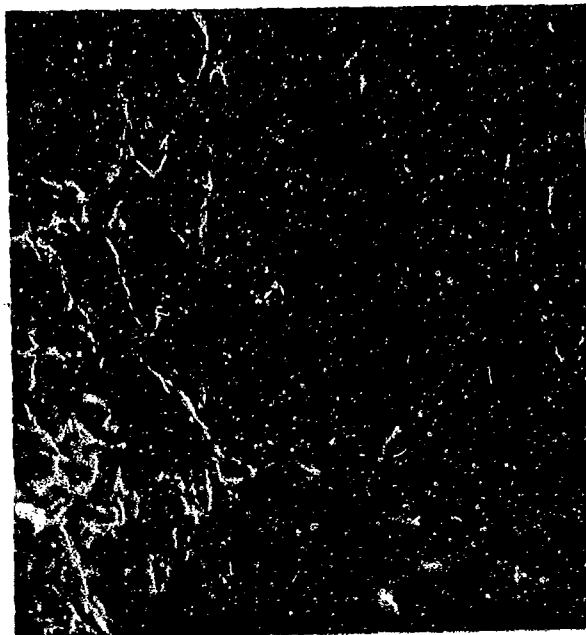


Figure 19. Quasi-cleavage facets in hydrogen-embrittled A-36 steel, 1100x.

area of
serpentine
glide

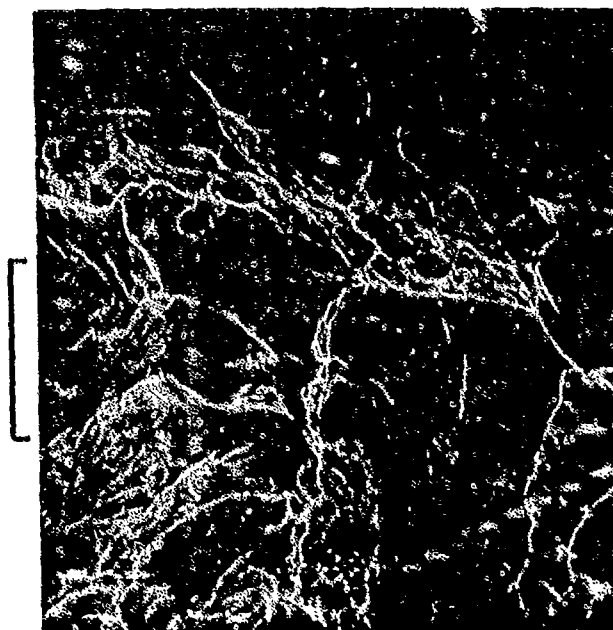
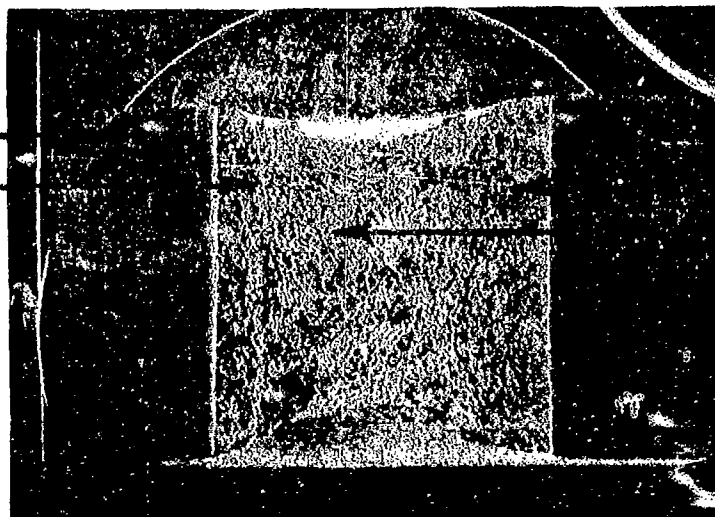


Figure 20. Inclusion-nucleated dimples in hydrogen-embrittled A-36 steel, 2000x.

notch
Figure 23



notch
Figure 22
Figure 24

Figure 21. Fatigue fracture surface of A-36 steel, 8x.

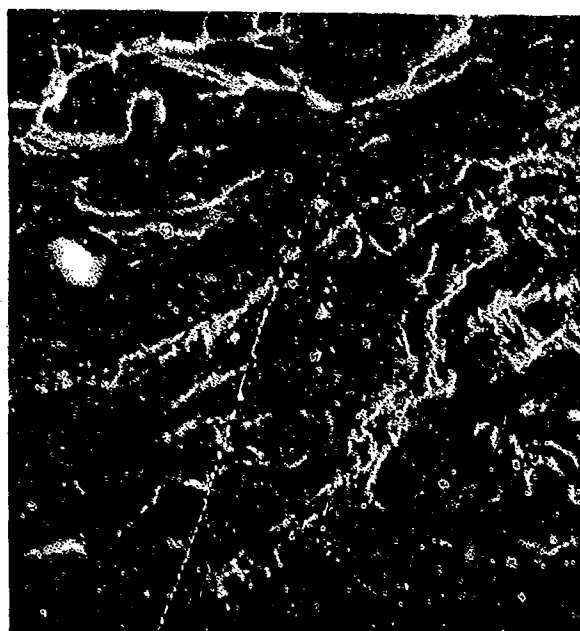


Figure 22. Fatigue striations on surface of A-36 steel, 4000x.

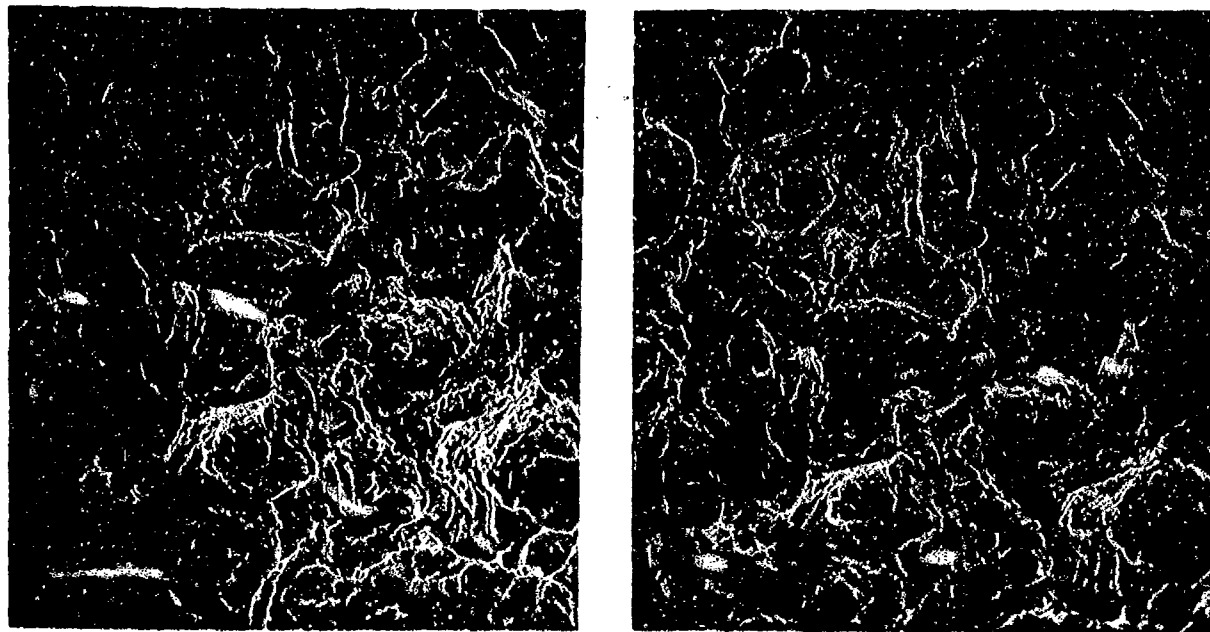


Figure 23. Stereo micrograph of fatigue zone in A-36 steel, 500x.

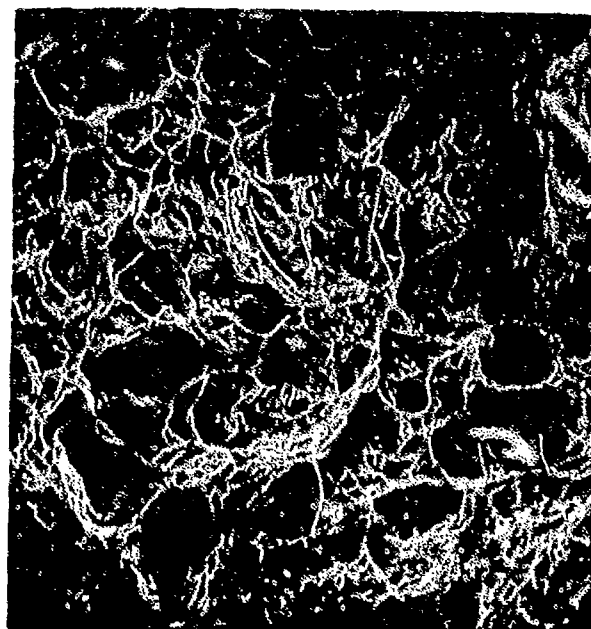


Figure 24. Tensile overload region in A-36 fatigue specimen, 700x.

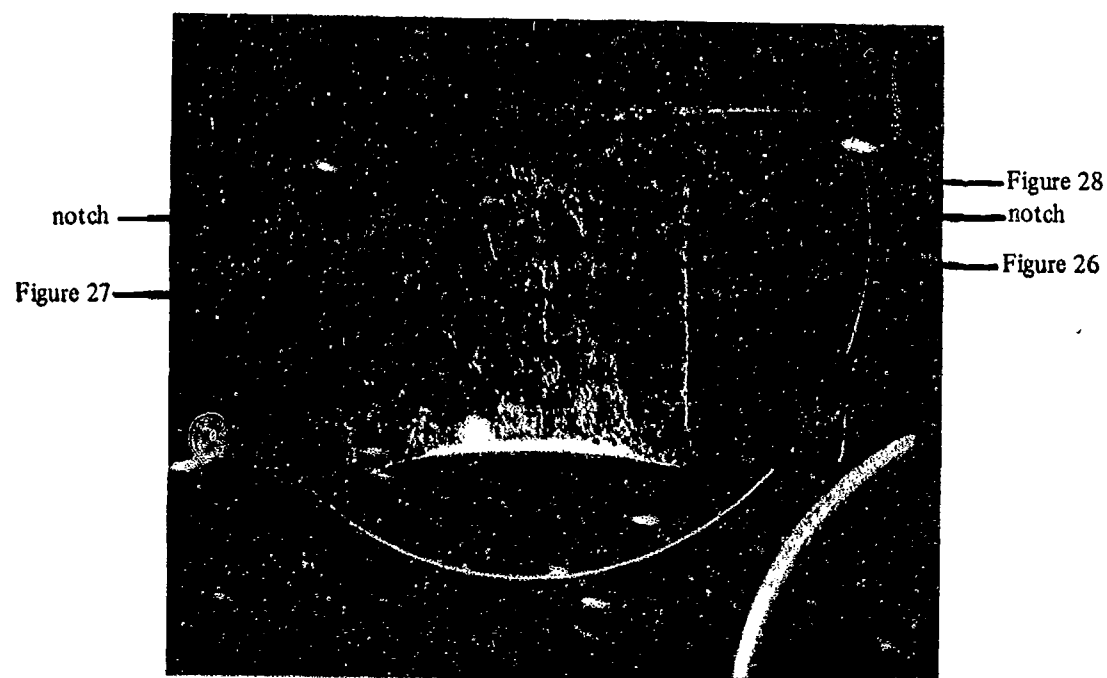


Figure 25. Fracture surface of a hydrogen-embrittled A-36 fatigue specimen, 8x.

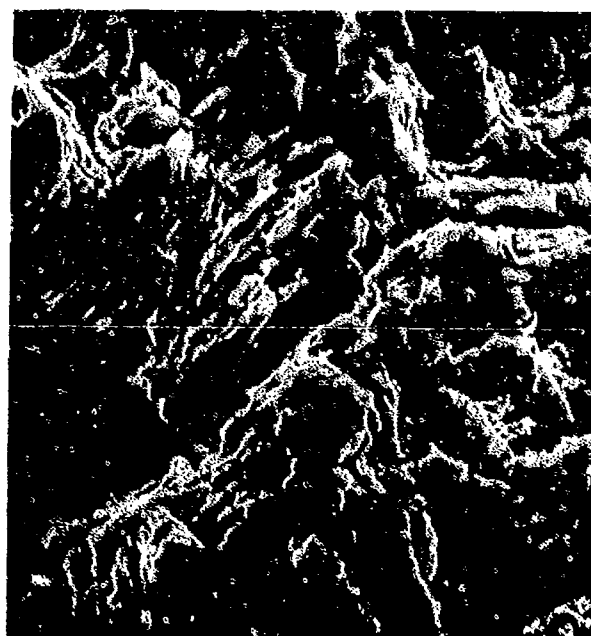


Figure 26. Fatigue striations on surface of hydrogen-embrittled A-36 fatigue specimen, 4250x.

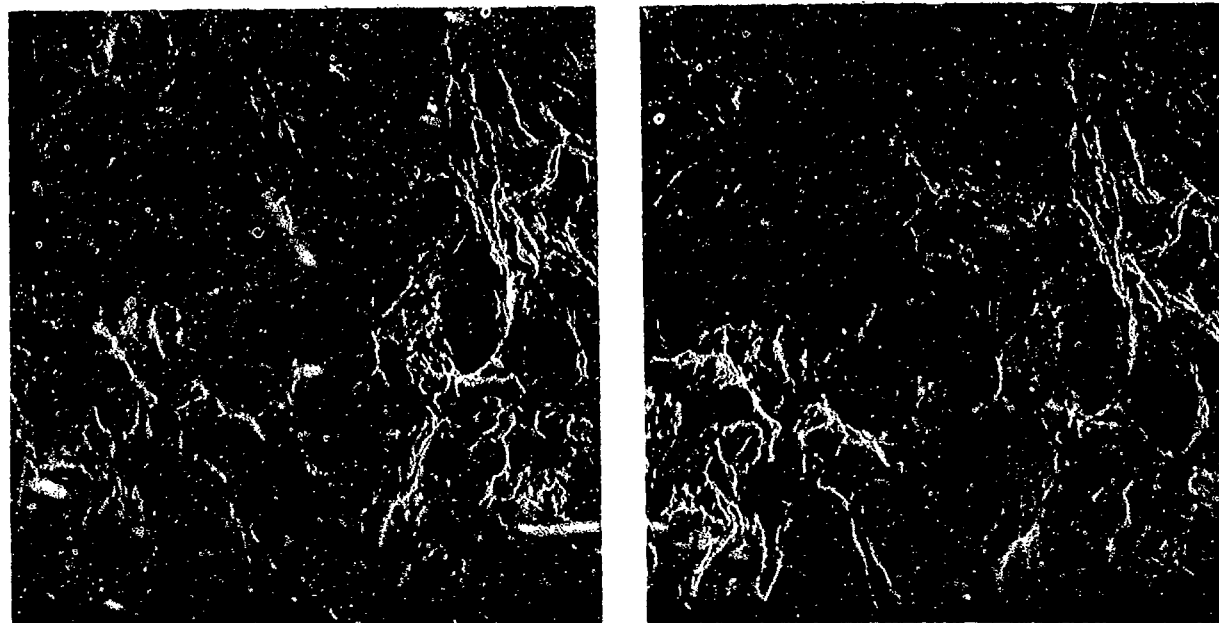


Figure 27. Stereo micrograph of fatigue zone in hydrogen-embrittled A-36 steel, 500x.

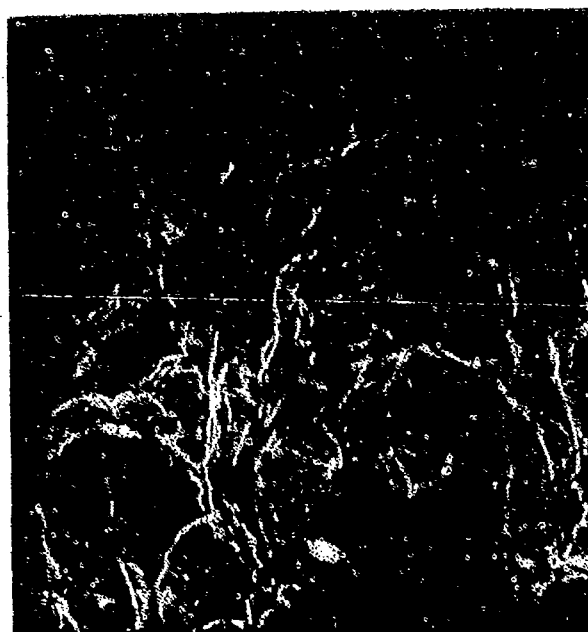


Figure 28. Tensile overload region in hydrogen-embrittled A-36 fatigue specimen, 1400x.

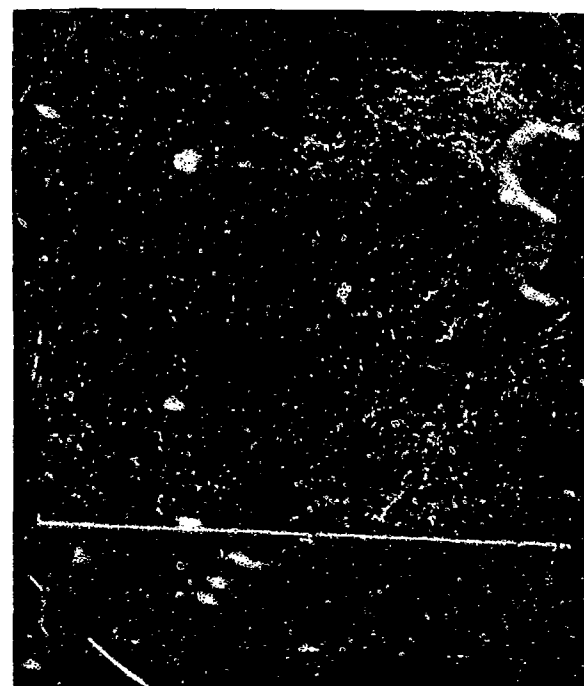


Figure 29. Fracture surface of A-36 Charpy specimen tested at -196°C , 7x.

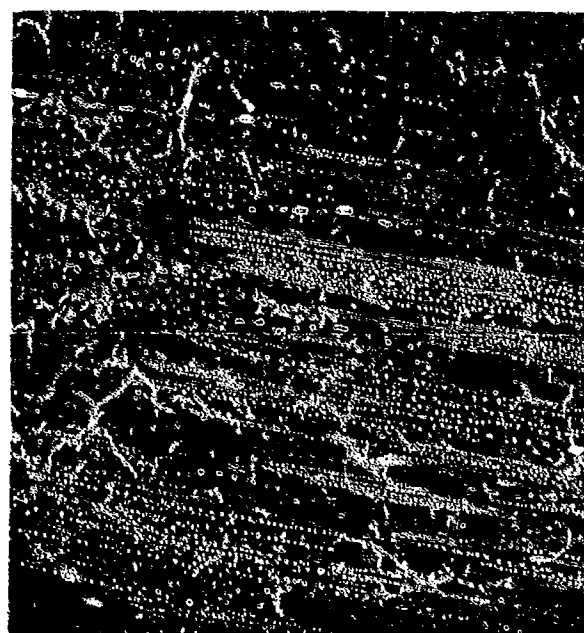


Figure 30. Cleavage fracture in A-36 Charpy specimen tested at -195°C , 100x.

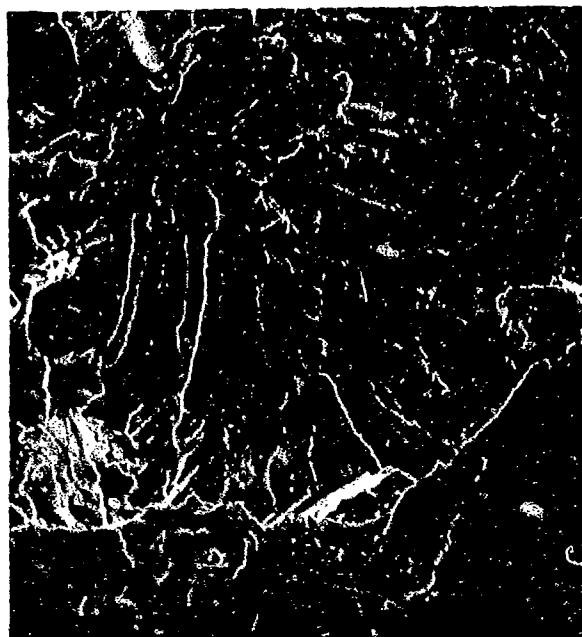


Figure 31. River patterns in cleavage facets, 500x.

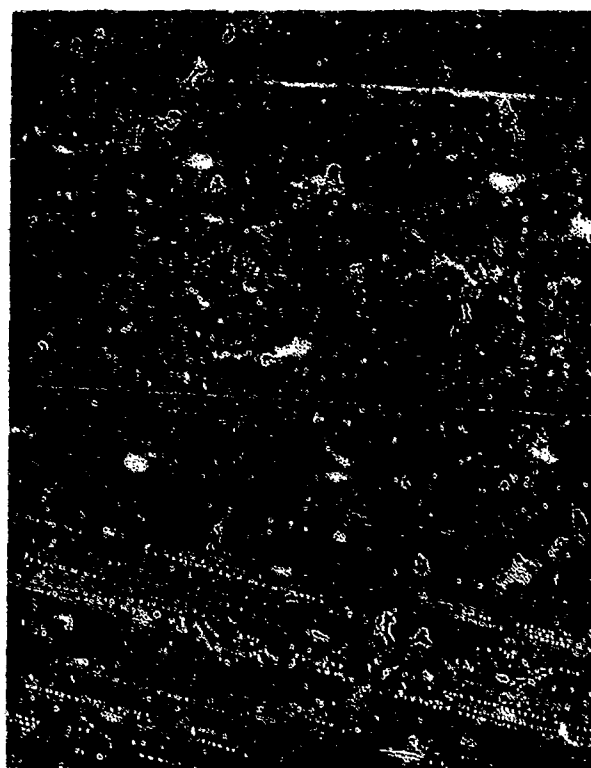


Figure 32. Fracture surface of A-36 Charpy specimen tested at -83°C , 7x.

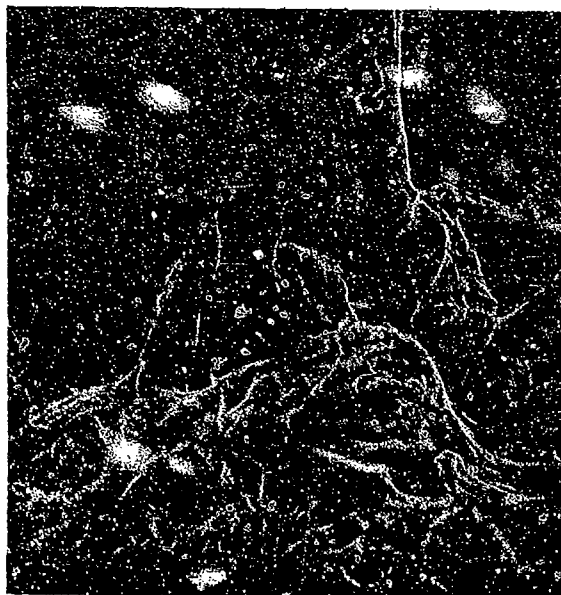


Figure 33. Mixed mode failure in A-36 Charpy specimen tested at -83°C , 1000x.

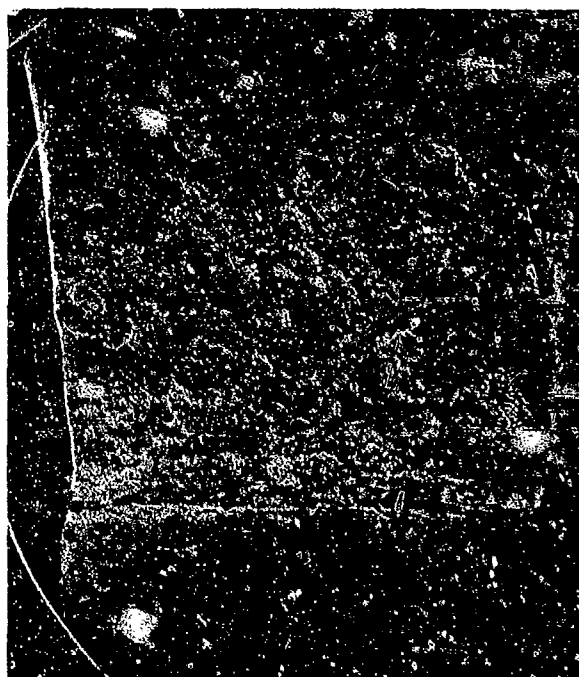


Figure 36.

Figure 35

notch

Figure 34. Fracture surface of A-36 Charpy specimen tested at -18°C , 7x.

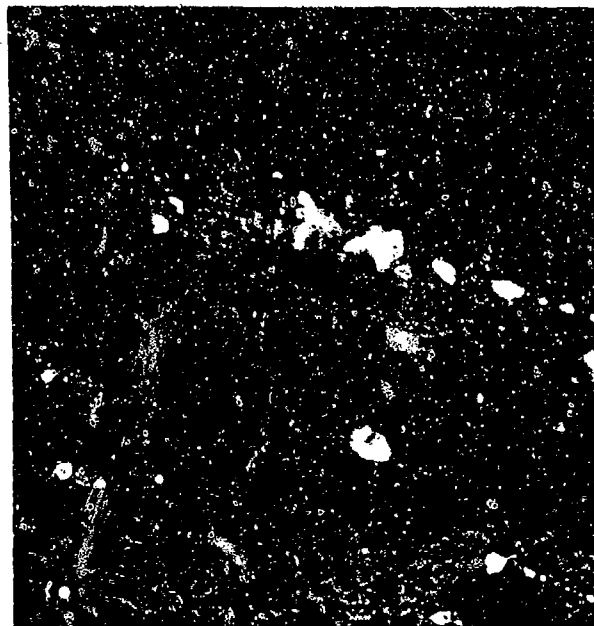


Figure 35. Dimple rupture in notch region of A-36 Charpy specimen tested at -18°C , 100x.

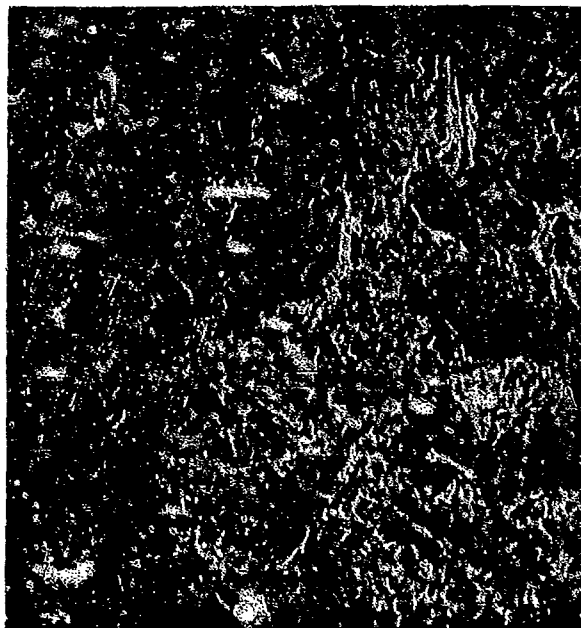


Figure 36. Mixed mode failure in central region of A-36 Charpy specimen tested at -18°C , 100x.

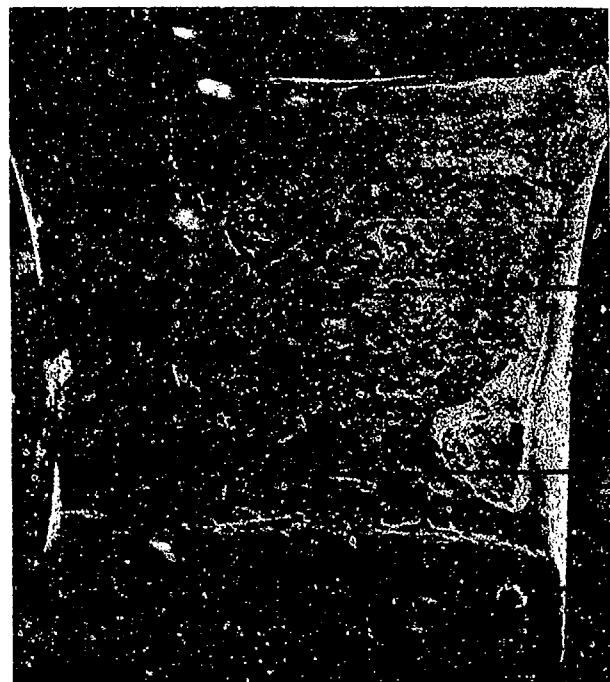


Figure 39

Figure 38

notch

Figure 37. Fracture surface of A-36 Charpy specimen tested at room temperature, 7x.



Figure 40

Figure 38. Dimple rupture in notch region of A-36 Charpy specimen tested at room temperature, 100x.

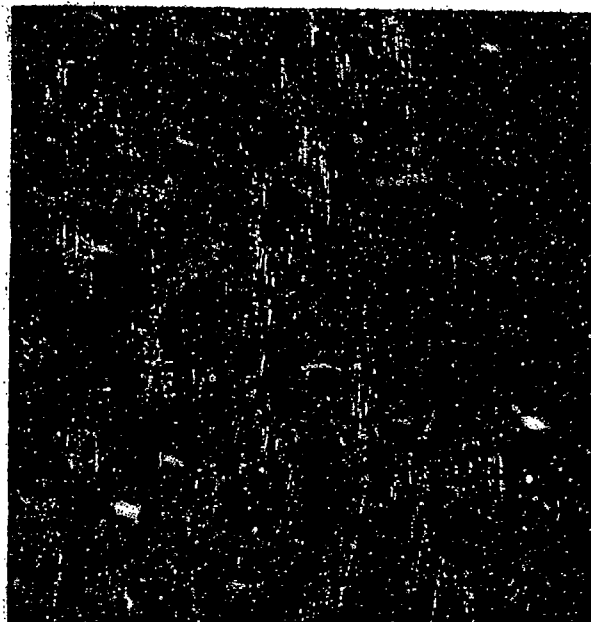


Figure 41

Figure 39. Cleavage fracture in central region of A-36 Charpy specimen tested at room temperature, 100x.

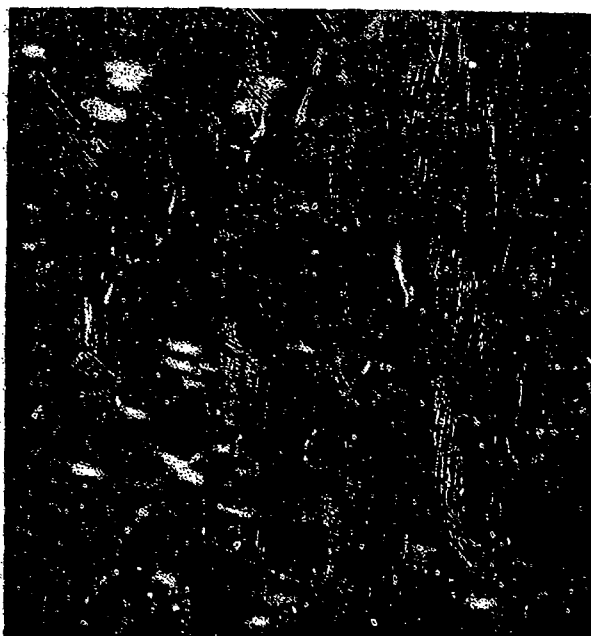


Figure 40. Microvoid coalescence and inclusion-generated voids in region near notch, 1000x.

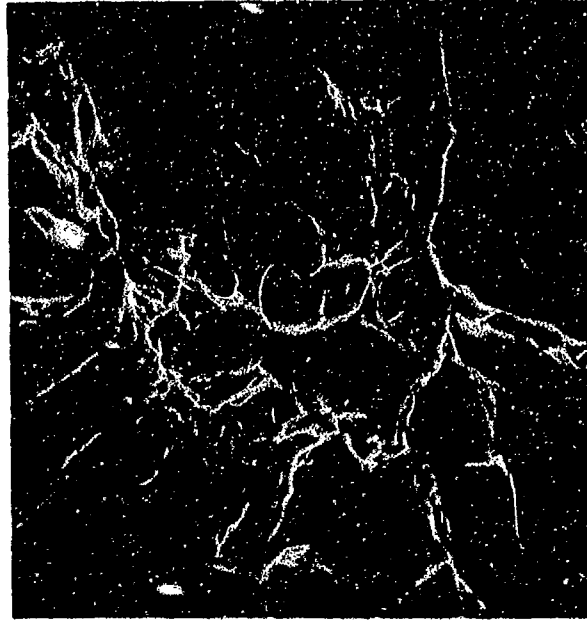


Figure 41. Microvoid coalescence interspersed among cleavage facets in central region of A-36 Charpy specimen tested at room temperature, 1000x.

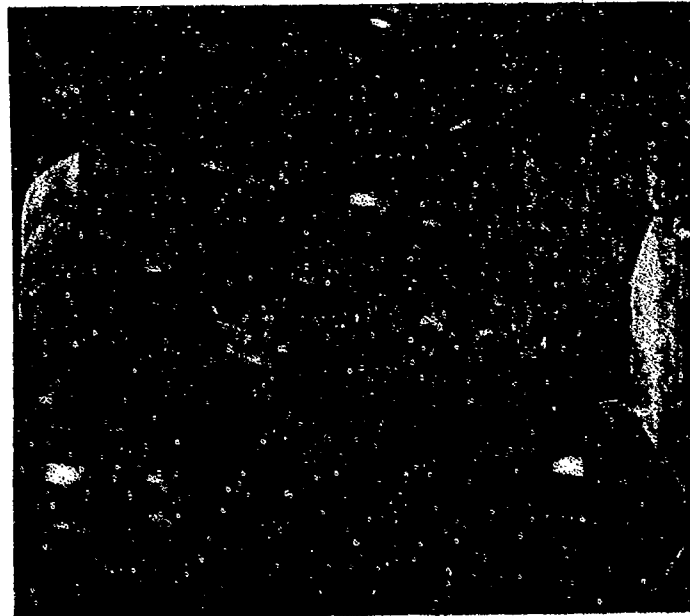


Figure 42. Tensile fracture surface of T-1 steel plate specimen, 8x.

Figure 43



Figure 44

Figure 43. Equiaxed dimples in central region of fractured surface, 1500x.



Figure 44. Equiaxed dimples containing inclusions, 7500x.

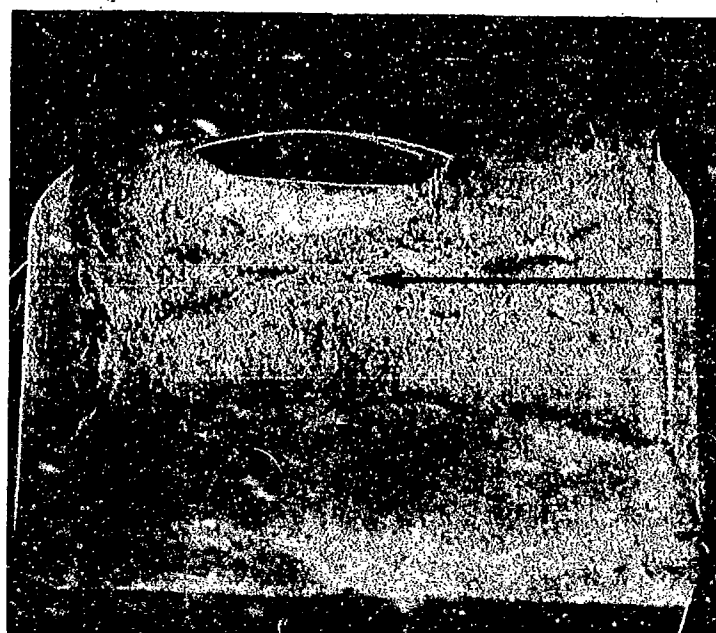


Figure 46

Figure 45. Tensile fracture surface of hydrogen-embrittled T-1 steel, 8x.

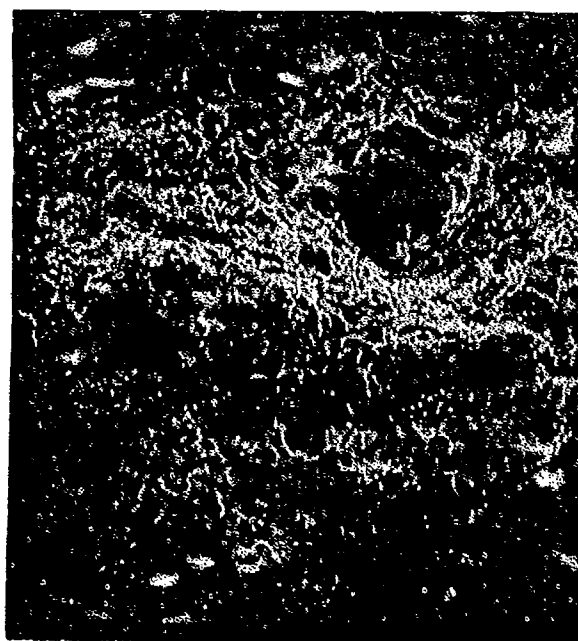


Figure 46. Tensile failure of hydrogen-embrittled steel by dimple rupture, 650x.

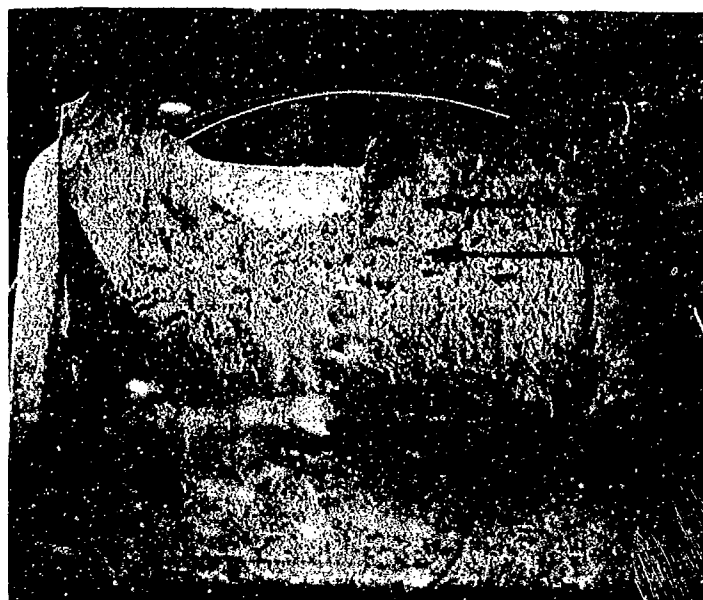


Figure 49

Figure 48

Figure 47. Tensile fracture surface of temper-embrittled steel, 8x.

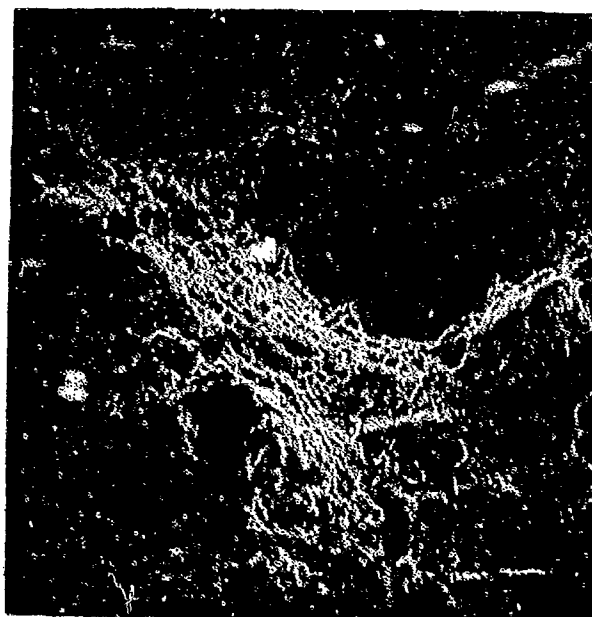


Figure 48. Tensile failure of temper-embrittled T-1 steel by dimple rupture, 375x.

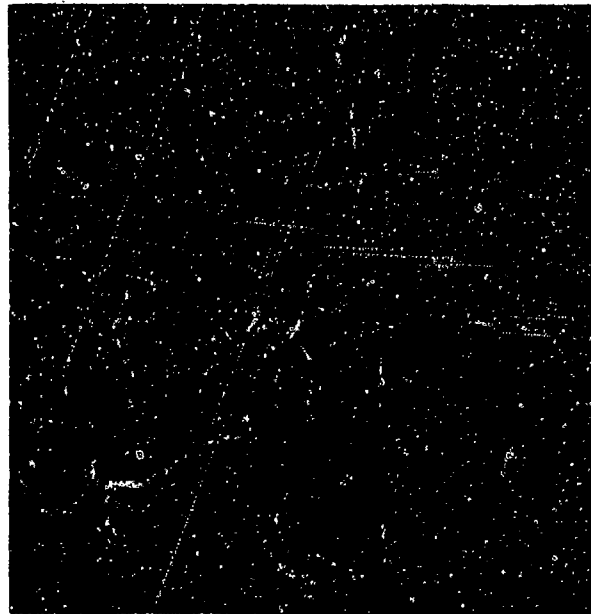


Figure 49. Equiaxed dimples and microvoid coalescence in temper-embrittled T-1 steel, 1500x.

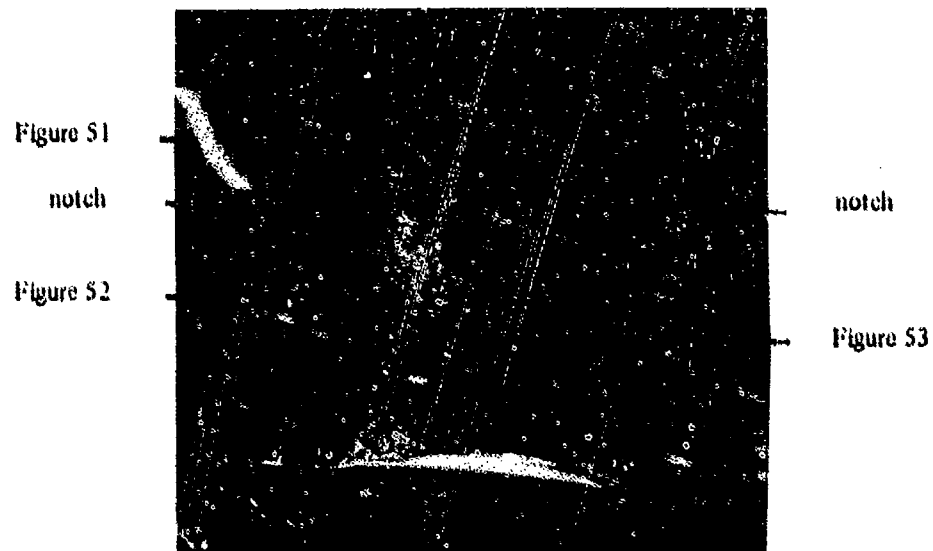


Figure 50. Fatigue fracture surface of a T-1 steel plate specimen, 10x.

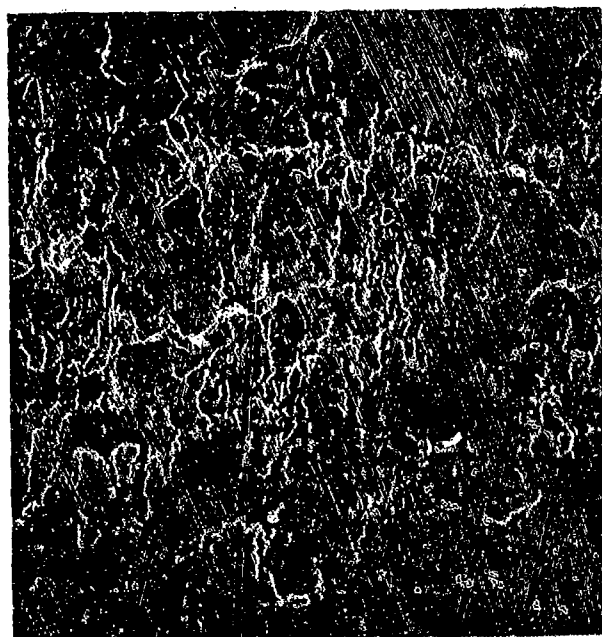


Figure 51. Fatigue striations on surface of T-1 fatigue specimen, 1000x.

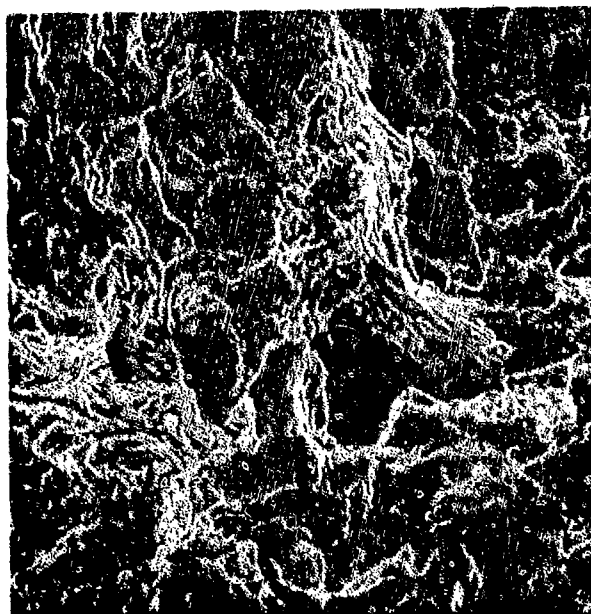
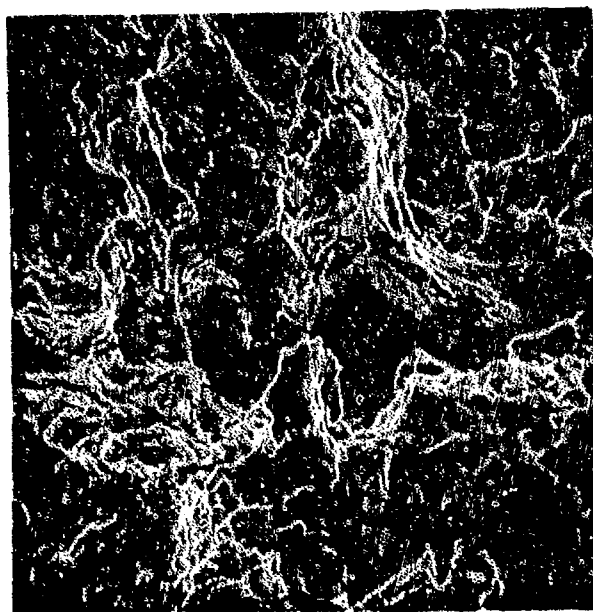


Figure 52. Stereo micrograph of the fatigue zone in T-1 steel, 1600x.

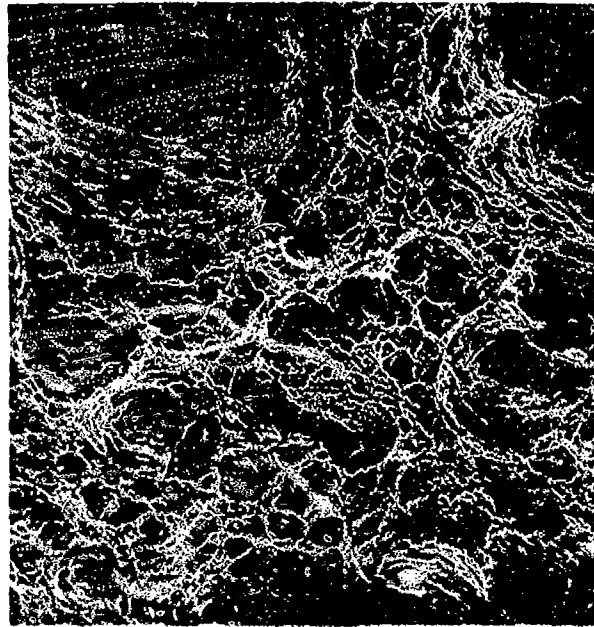


Figure S3. Tensile overload region of T-1 fatigue specimen, 700x.



Figure S4. Fracture surface of hydrogen-embrittled T-1 plate fatigue specimen, 8x.

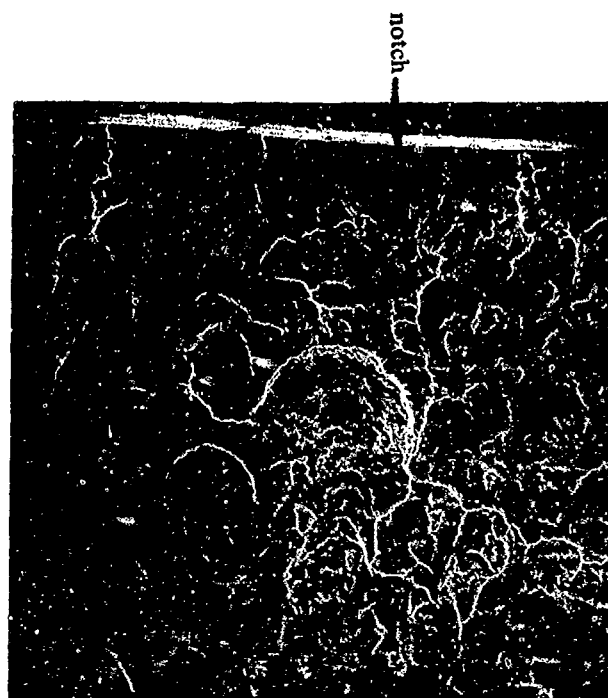


Figure 55. Fatigue zone of hydrogen-embrittled T-1 plate fatigue specimen, 60x.

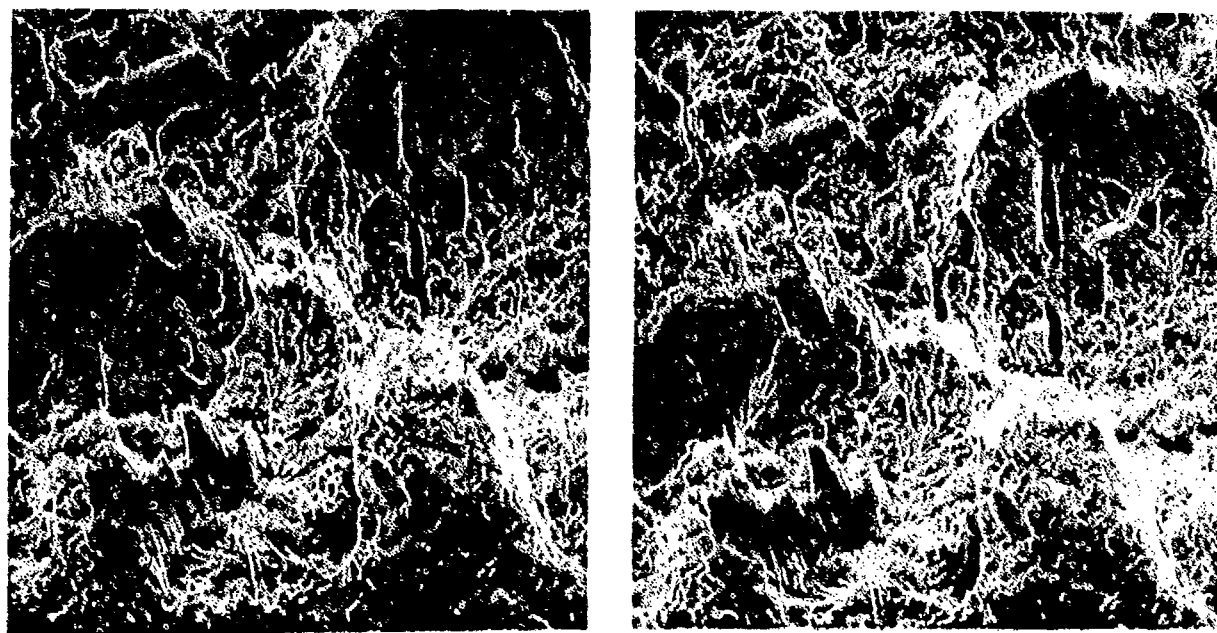


Figure 56. Stereo micrograph of fatigue zone in hydrogen-embrittled T-1 steel, 400x.

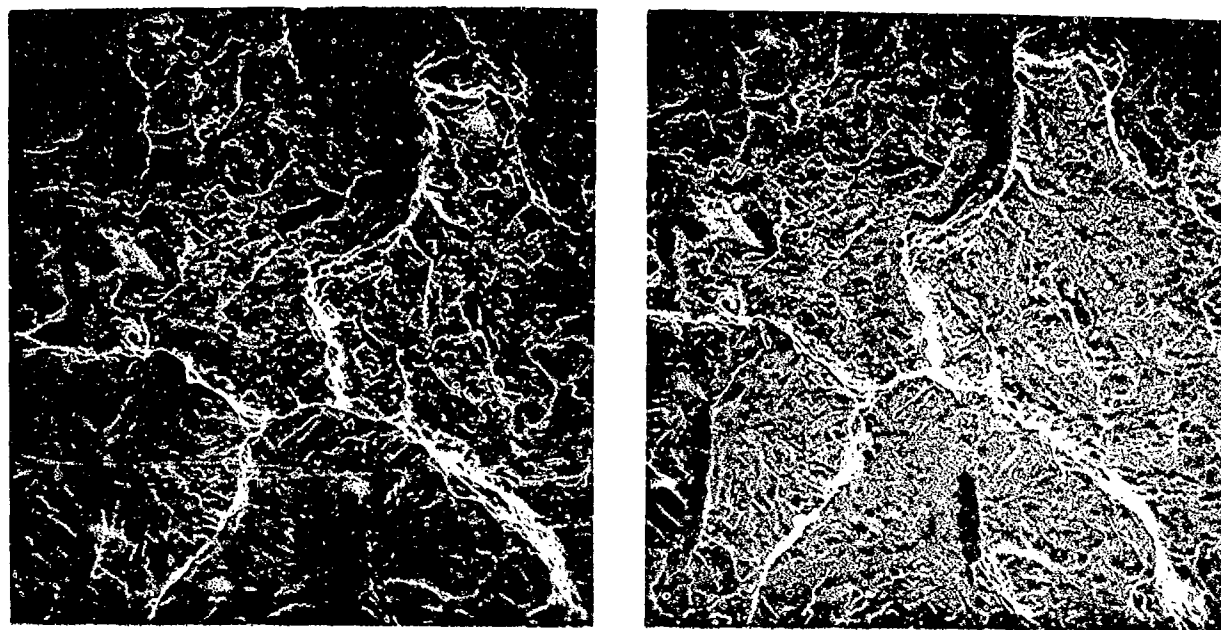


Figure 57. Stereo micrograph of fatigue zone in hydrogen-embrittled T-1 steel, 500x.

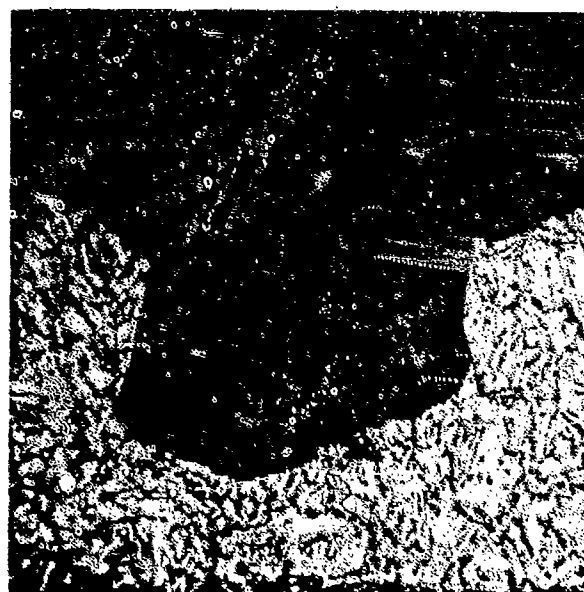


Figure 58. Optical micrograph of a longitudinal section of the fatigue zone in hydrogen-embrittled T-1 steel, 550x.

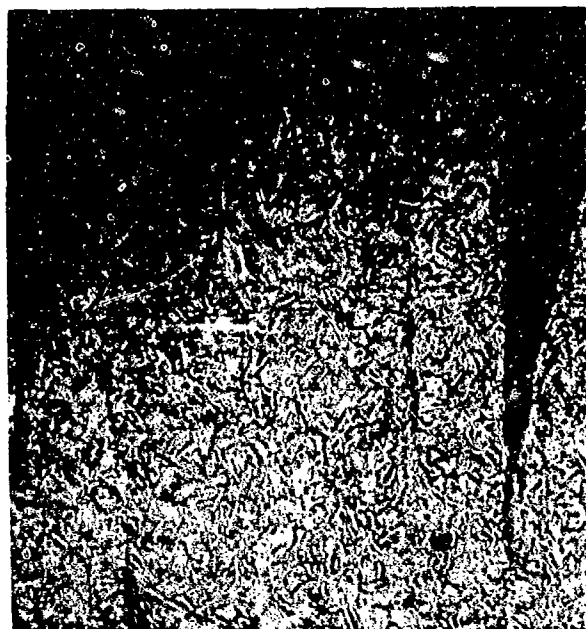


Figure 59. Optical micrograph showing the beginning and intermediate stages of crater formation, 550x.

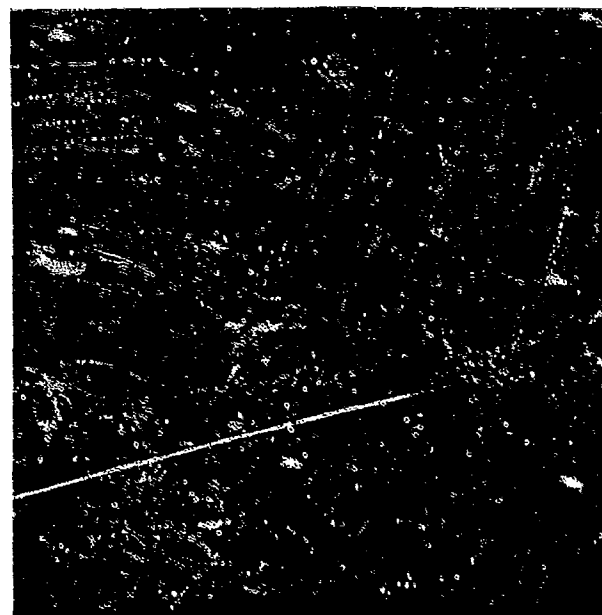


Figure 60. Tensile overload region of hydrogen-embrittled T-1 plate fatigue specimen, 140x.

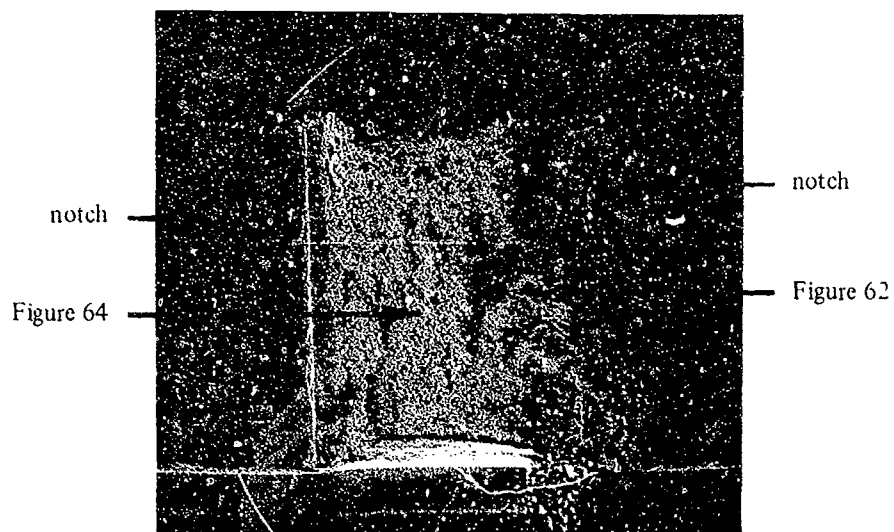


Figure 61. Fracture surface of temper-embrittled T-1 plate fatigue specimen, 10x.

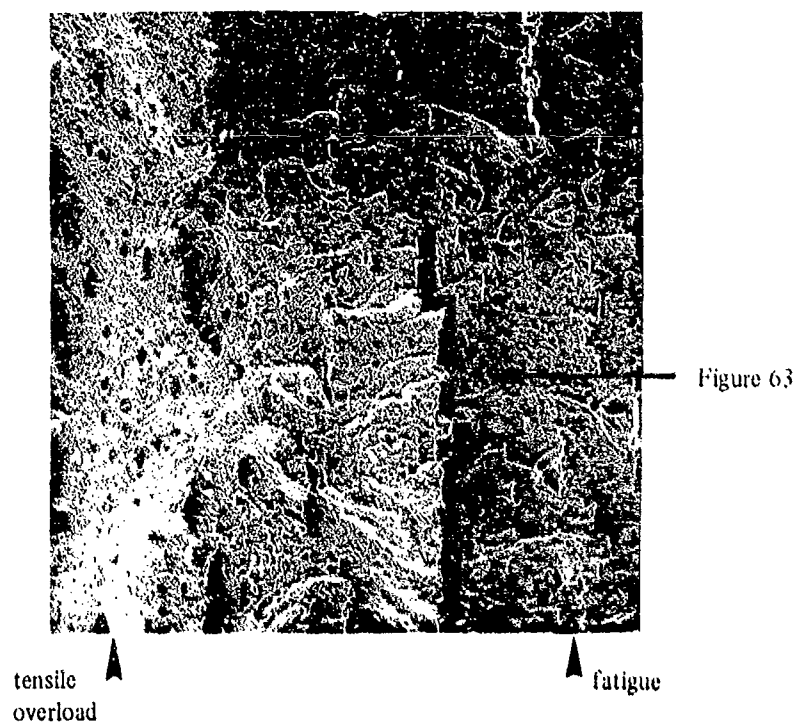


Figure 62. Transition region from fatigue to tensile overload in temper-embrittled T-1 fatigue specimen, 35x.

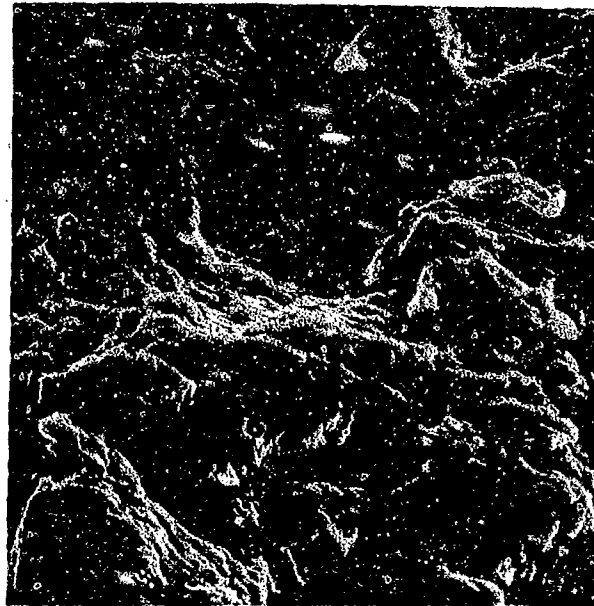


Figure 63. Fatigue striations on fracture surface of temper-embrittled T-1 steel, 5000x.

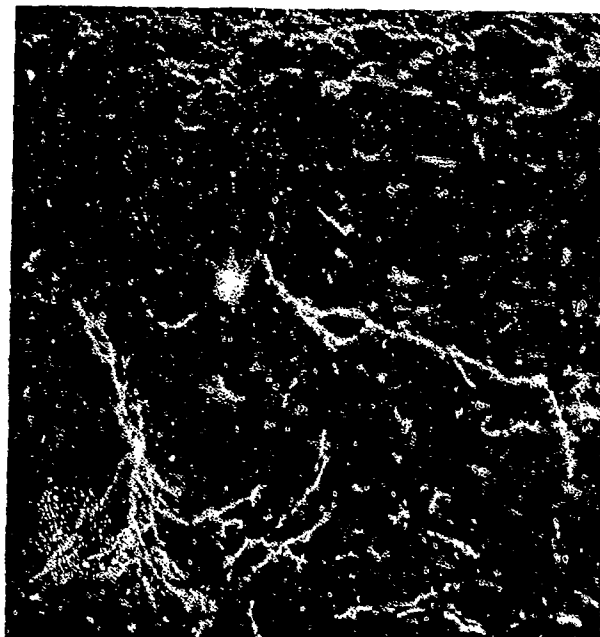


Figure 64. Dimple rupture in tensile overload region of temper-embrittled T-1 steel fatigue specimen, 3500x.

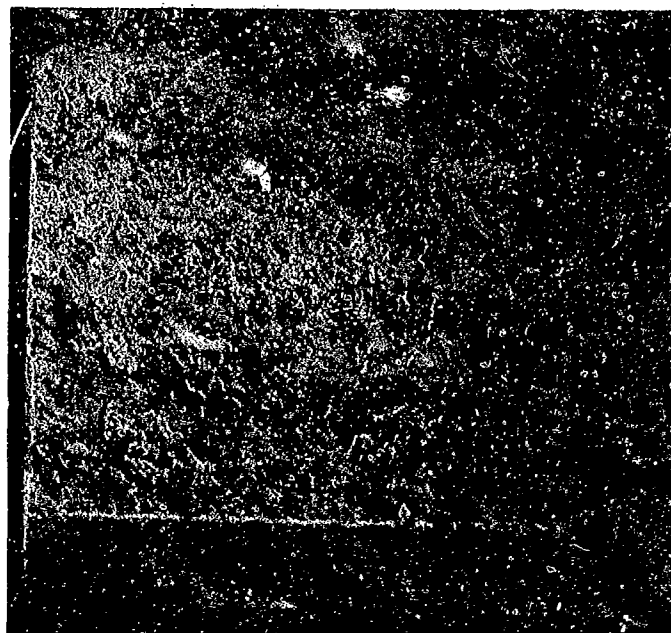


Figure 66

notch

Figure 65. Fracture surface of T-1 Charpy specimen tested at -196°C , 8x.

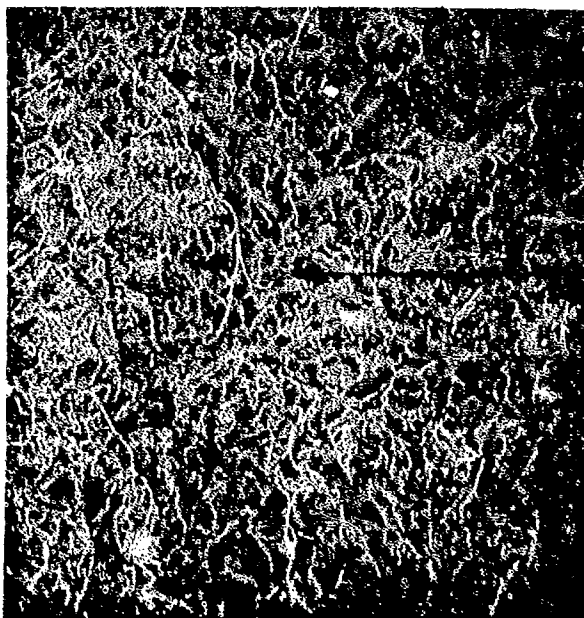


Figure 67

Figure 66. Cleavage fracture in T-1 Charpy specimen tested at -196°C , 250x.



Figure 67. Cleavage facets containing tear lines, 5000x.

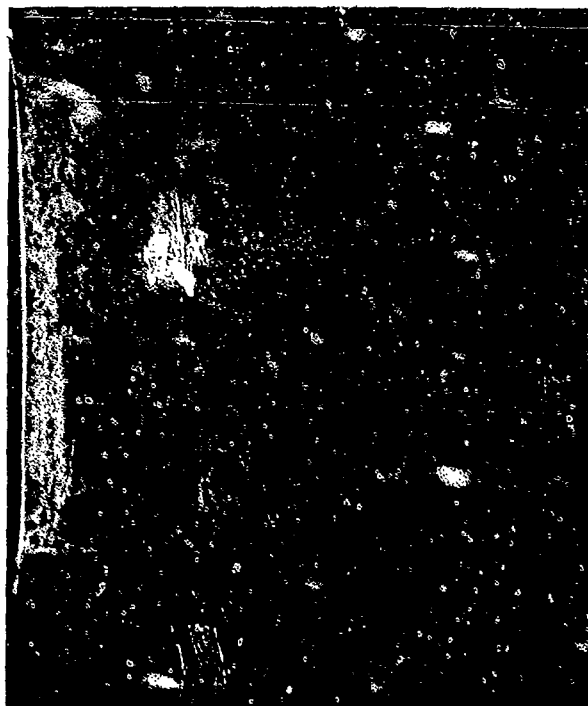


Figure 70

Figure 68. Fracture surface of a T-1 Charpy specimen tested at -83°C , 8x.

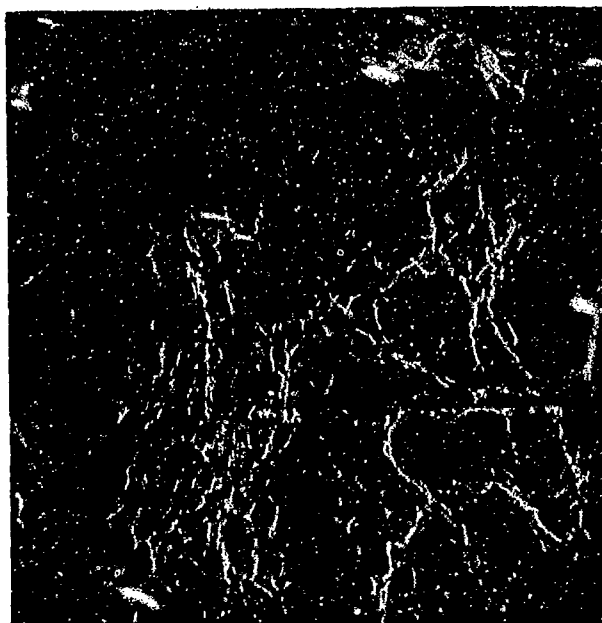


Figure 69. Edge of T-1 Charpy specimen tested at -83°C , 1000x.

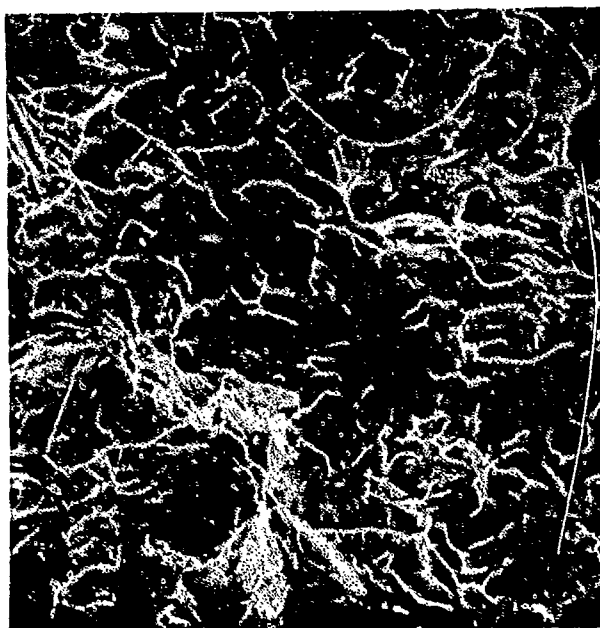


Figure 70. Center of T-1 Charpy specimen tested at -83°C , 1000x.

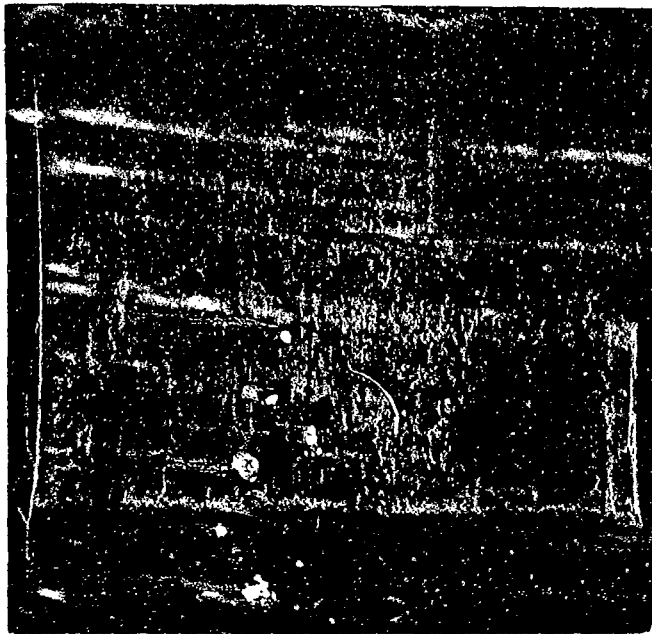


Figure 72

notch

Figure 71. Fracture surface of T-1 Charpy specimen tested at -18°C , 8x.

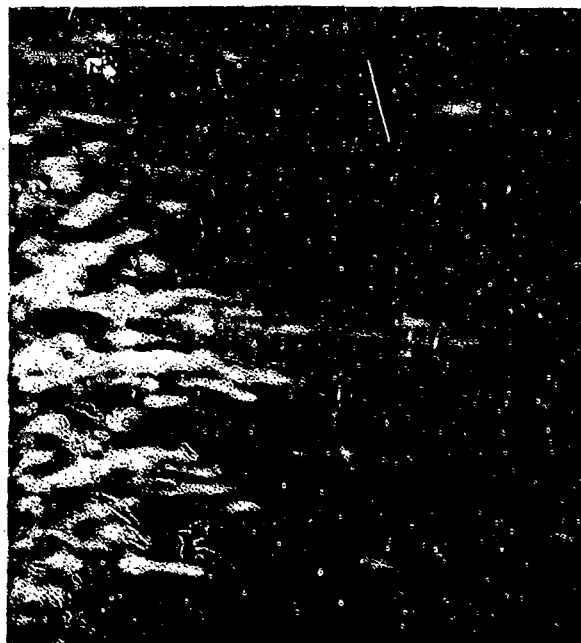


Figure 72. Failure of T-1 Charpy specimen tested at 18°C by dimple rupture, 1000x.



Figure 73. Fracture surface of T-1 Charpy specimen tested at room temperature, 10x.

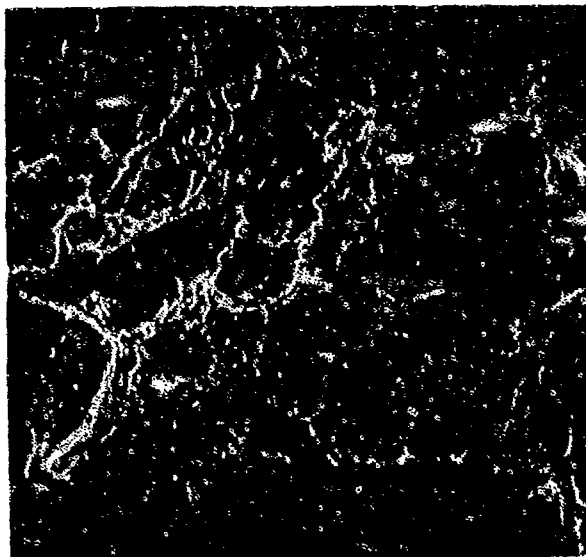


Figure 74. Failure of T-1 Charpy specimen tested at room temperature by ductile rupture, 1700x.

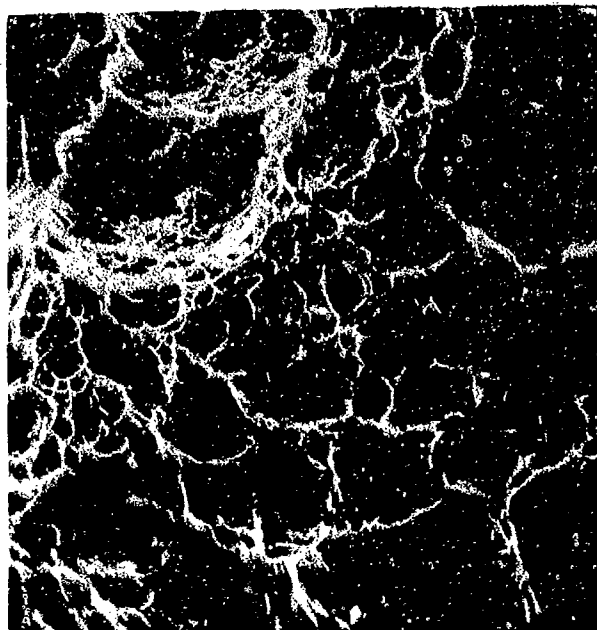


Figure 75. Dimple rupture by microvoid coalescence, 4250x.



Figure 76. Tensile fracture surface of HY-130 steel specimen, 8x.

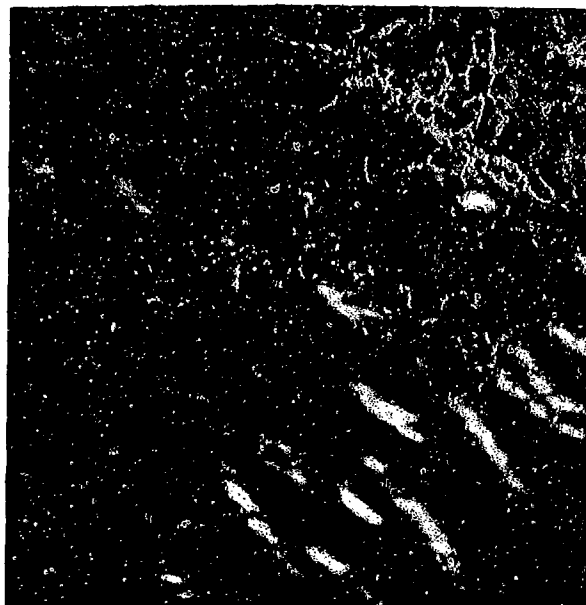


Figure 77. Center of HY-130 tensile specimen, 1500x.



Figure 78. Edge of HY-130 tensile specimen, 1600x.



Figure 79. Tensile fracture surface of hydrogen-embrittled HY-130 specimen, 9x.

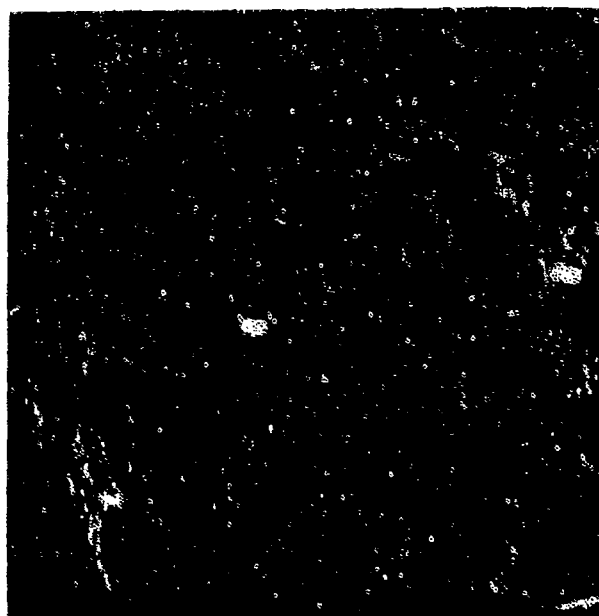


Figure 80. "Fisheyes" on surface of hydrogen-embrittled HY-130 tensile specimen, 120x.

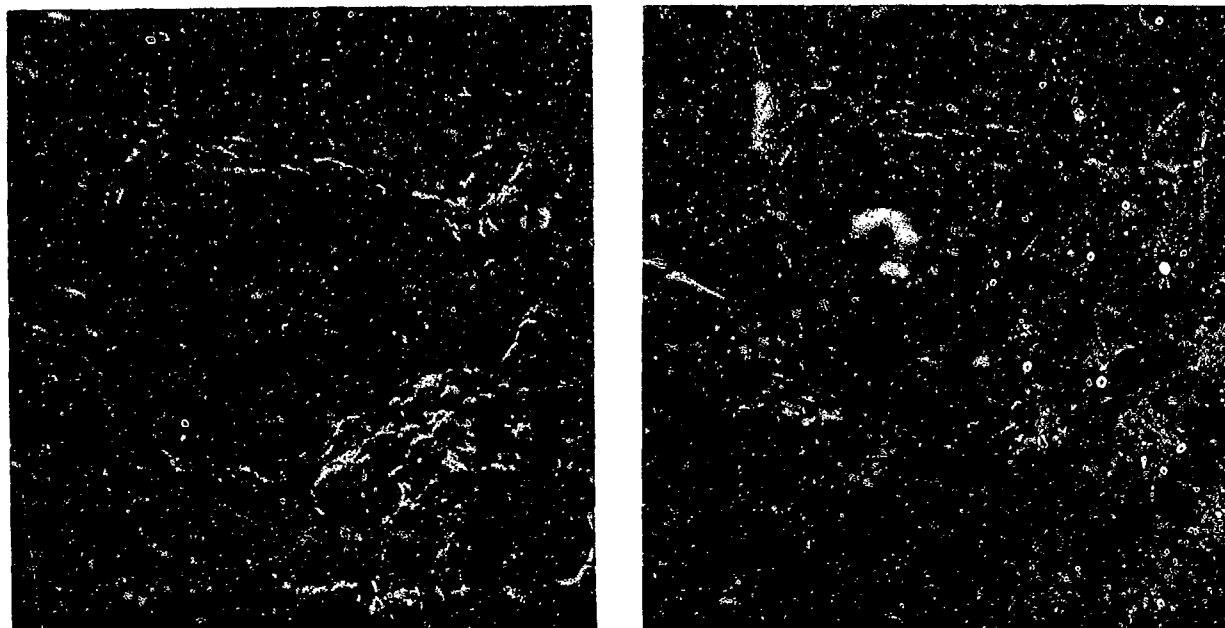


Figure 81. Stereo micrograph of center of fisheye on fracture surface of hydrogen-embrittled HY-130 tensile specimen, 1400x.

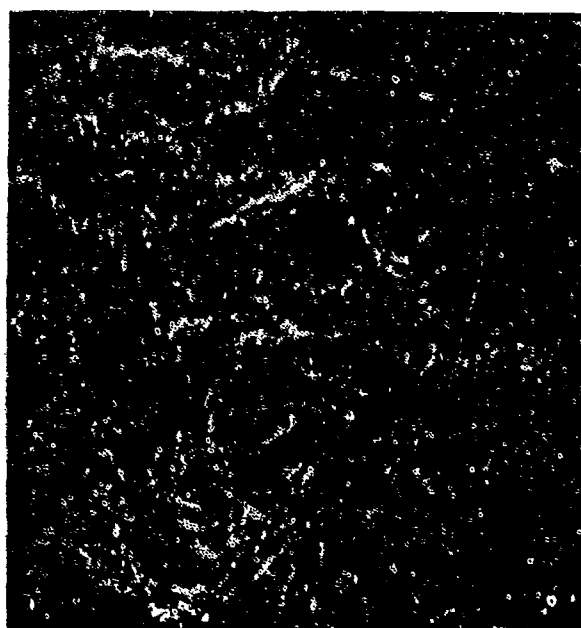


Figure 82. Quasi-cleavage fracture in fisheye, 1600x.

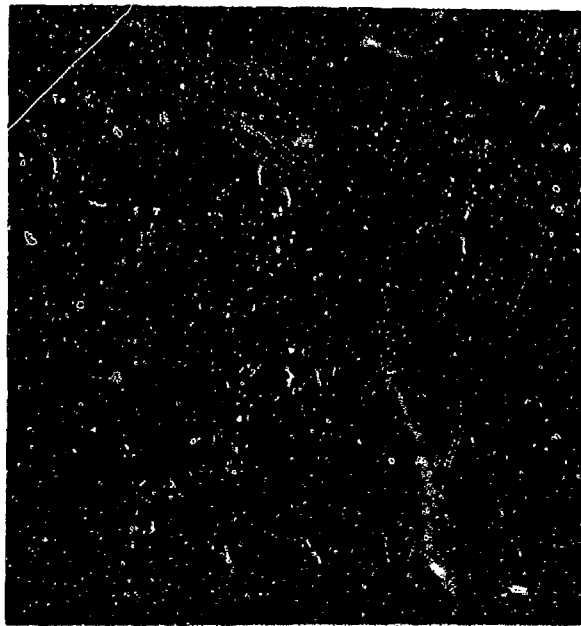


Figure 84

Figure 83. Grain boundary separation with microvoid coalescence in hydrogen-embrittled HY-130 tensile specimen, 1200x.



Figure 84. Grain boundary separation with microvoid coalescence in hydrogen-embrittled HY-130 tensile specimen, 3000x.

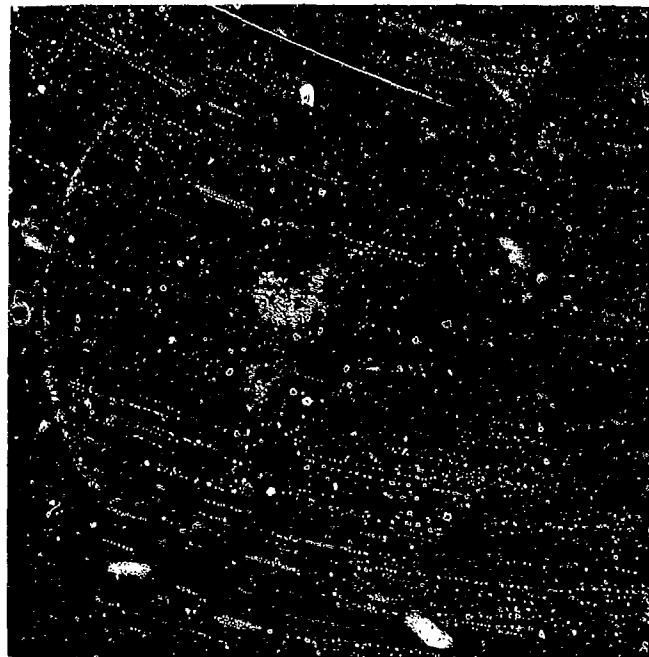


Figure 87

Figure 86

Figure 85. Tensile fracture surface of temper-embrittled HY-130 specimen, 8x.

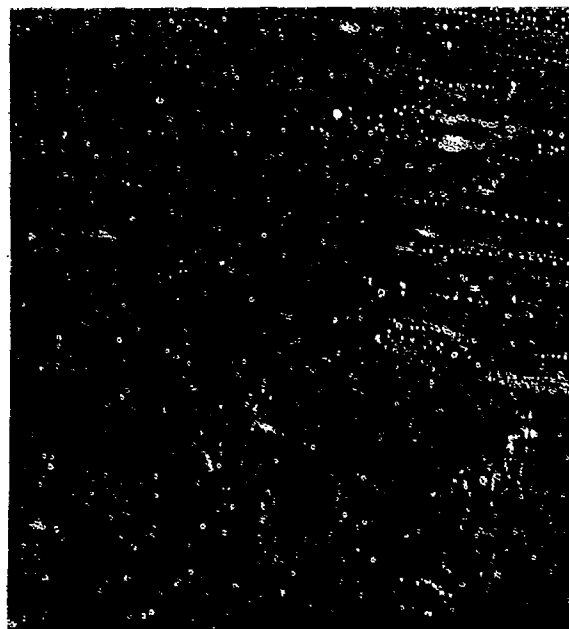


Figure 86. Fracture surface of temper-embrittled HY-130 tensile specimen, 375x.

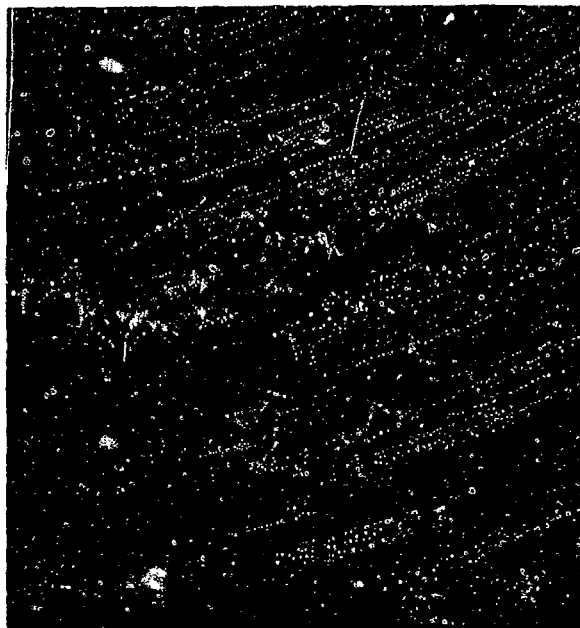
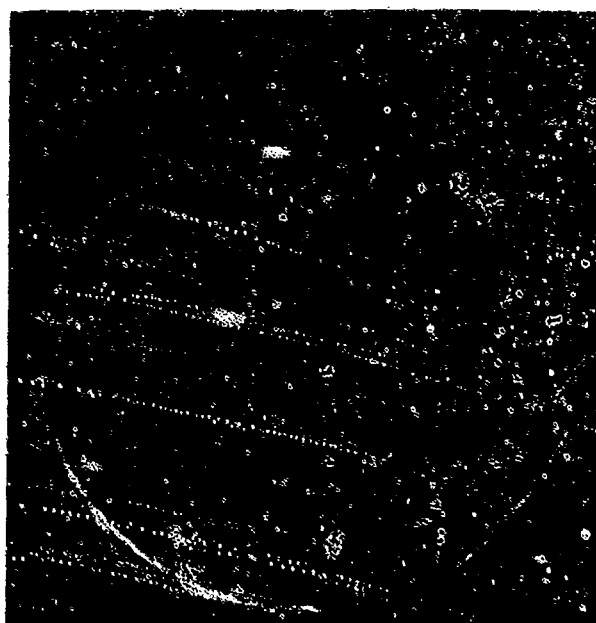


Figure 87. Fracture of temper-embrittled HY-130 tensile specimen by slipping, tearing, and microvoid coalescence, 1500x.



notch

Figure 88. Fracture surface of round HY-130 fatigue specimen, 10x.

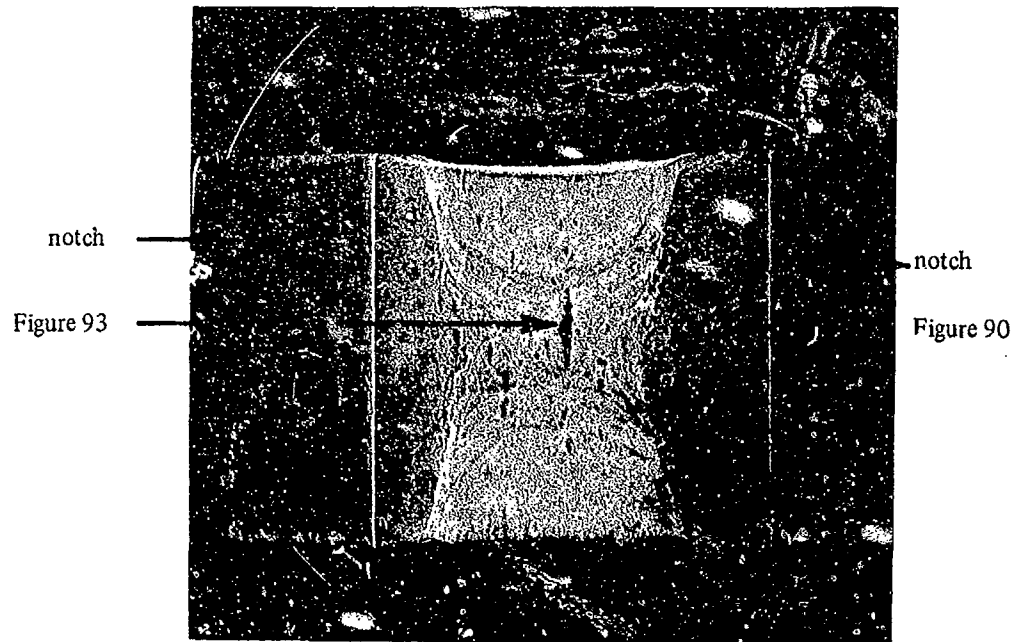


Figure 89. Fracture surface of flat HY-130 fatigue specimen, 8x.



Figure 90. Fatigue region of HY-130 fracture surface, 50x.

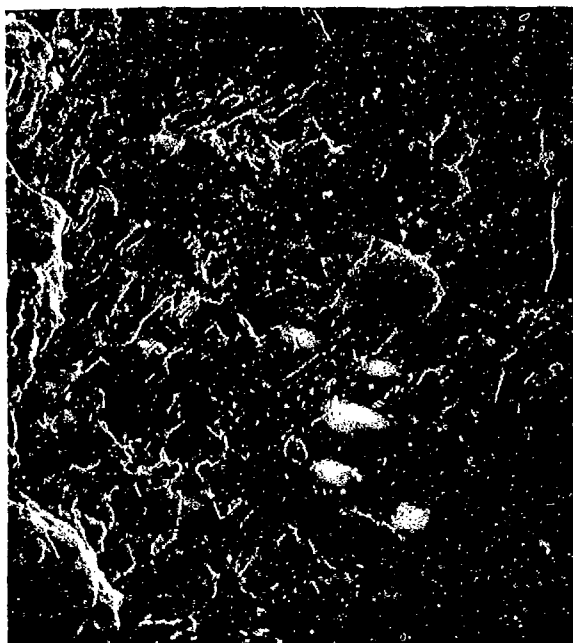


Figure 91. Fatigue striations on fracture surface of HY-130 steel, 1450x.

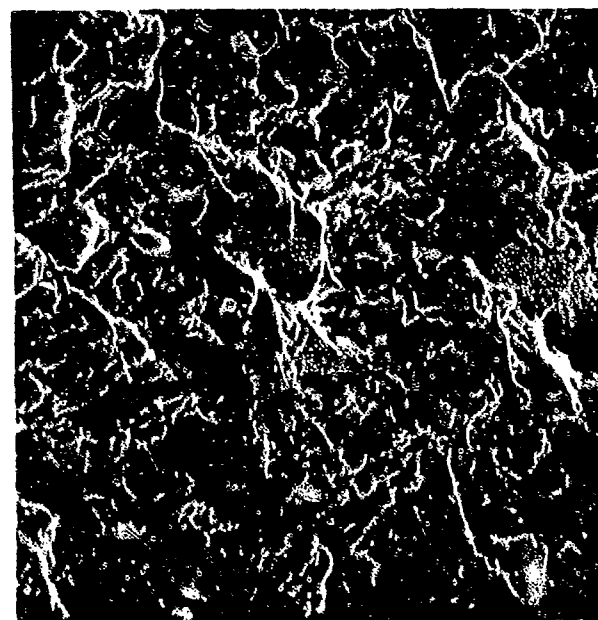
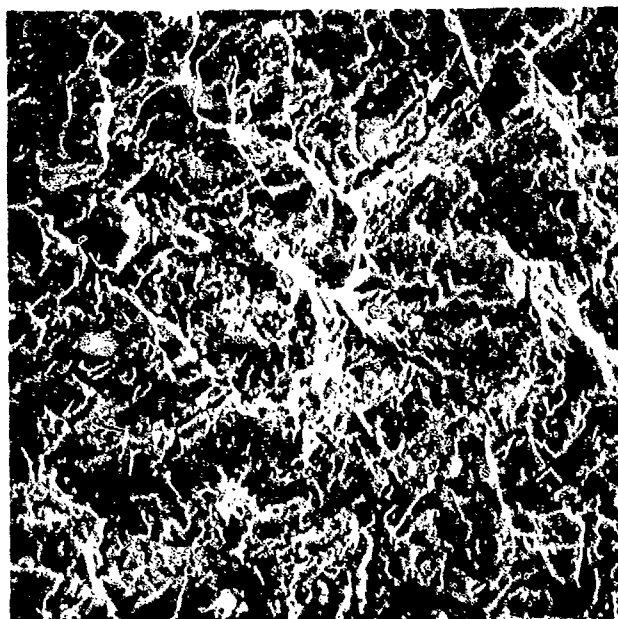


Figure 92. Stereo micrograph of fatigue zone in HY-130 steel, 1550x.

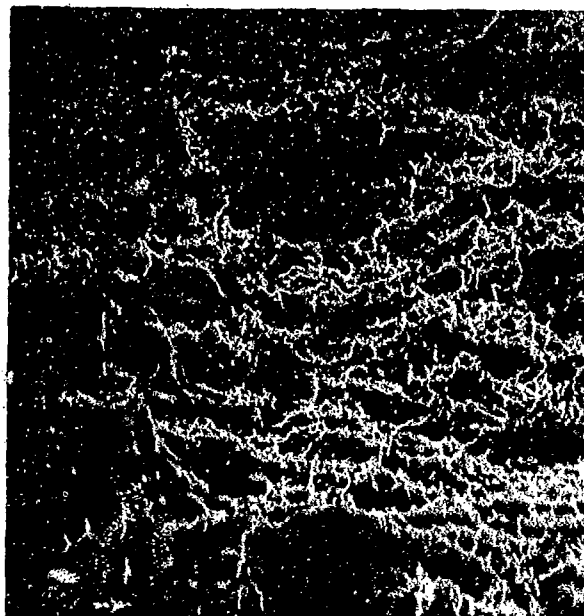


Figure 93. Tensile overload zone in HY-130 fatigue specimen, 1500x.



Figure 94. Fracture surface of hydrogen-embrittled HY-130 fatigue specimen, 10x.



Figure 96

Figure 95. Fatigue region of hydrogen-embrittled HY-130 fatigue specimen, 40x.

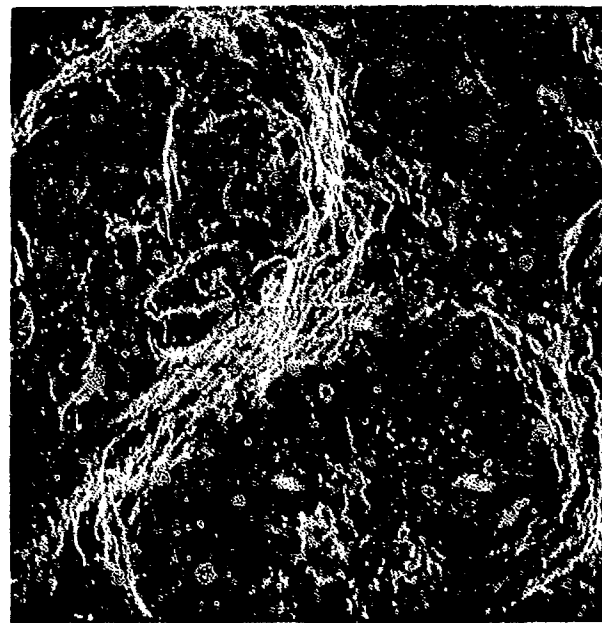
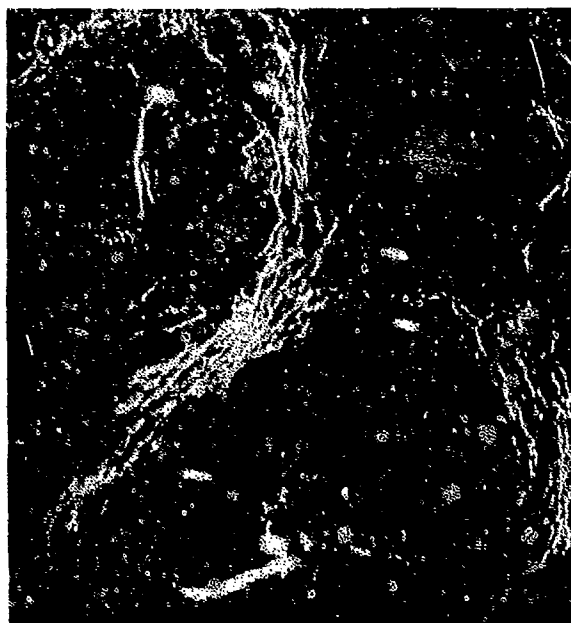


Figure 96. Stereo micrograph of fatigue zone in hydrogen-embrittled HY-130 Steel, 400x.

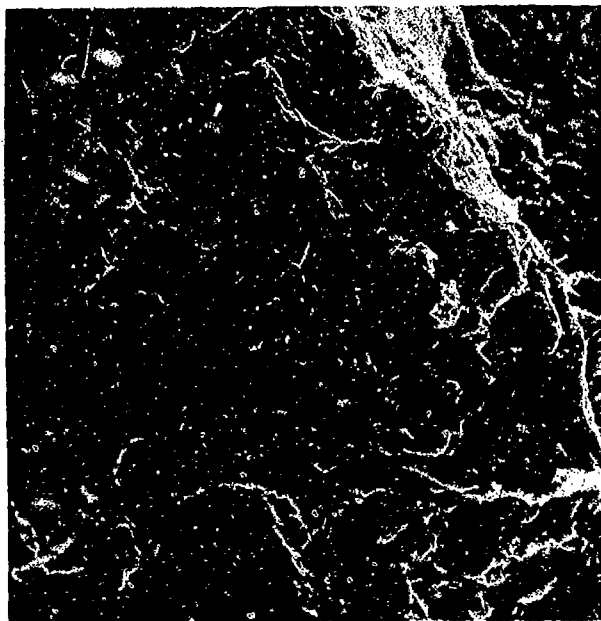


Figure 97. Fatigue striations on fracture surface of hydrogen-embrittled HY-130 steel, 1600x.



Figure 98. Tensile overload region in hydrogen-embrittled HY-130 steel, 1500x.

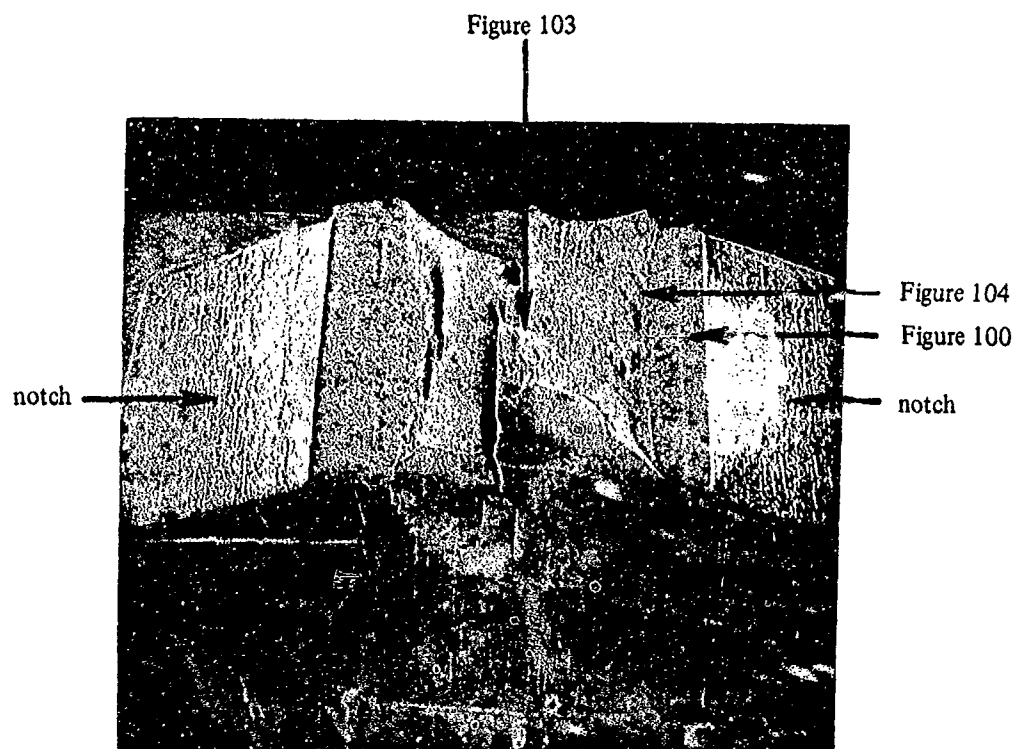


Figure 99. Fracture surface of temper-embrittled HY-130 fatigue specimen, 8x.

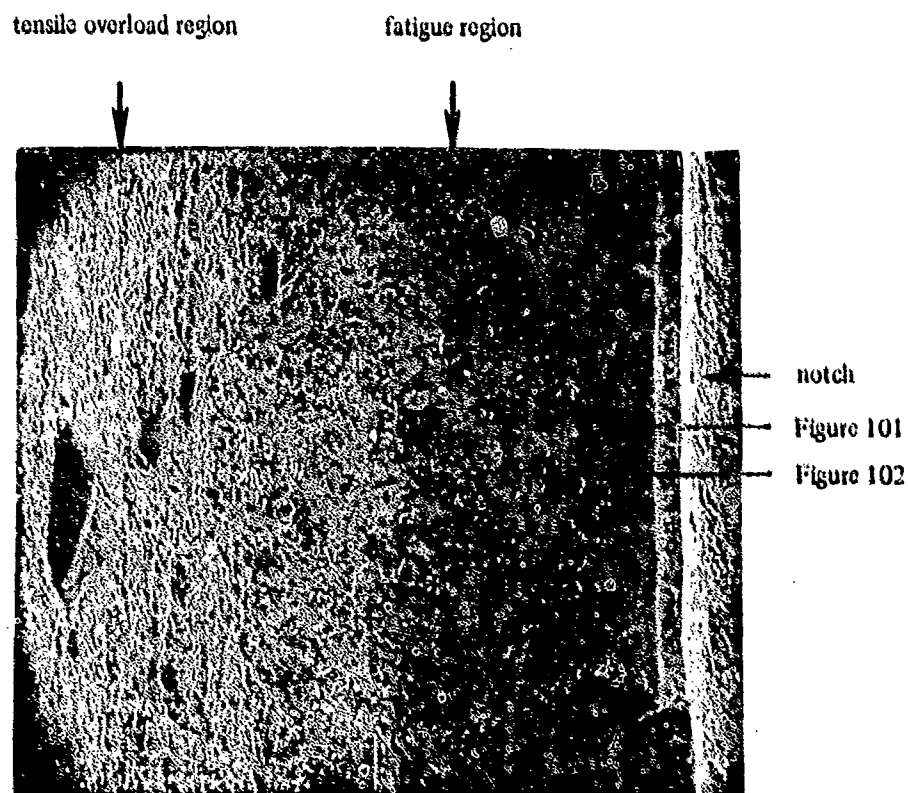


Figure 100. Fatigue region of temper-embrittled HY-130 fatigue specimen, 60x.

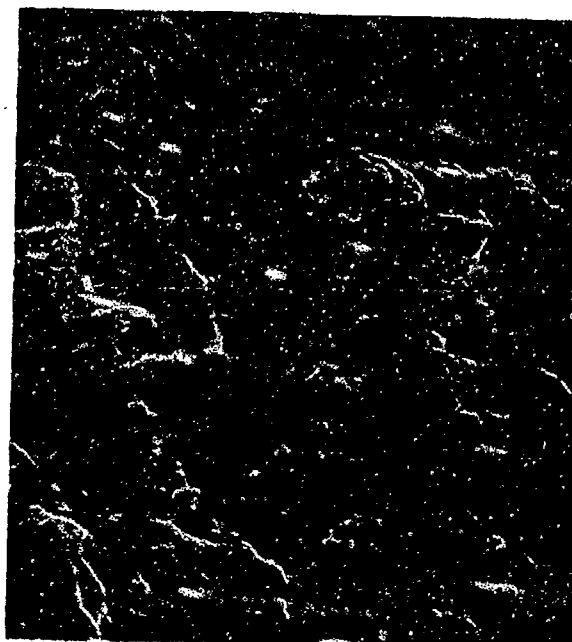


Figure 101. Fatigue striations on fracture surface of temper-embrittled HY-130 steel, 1600x.

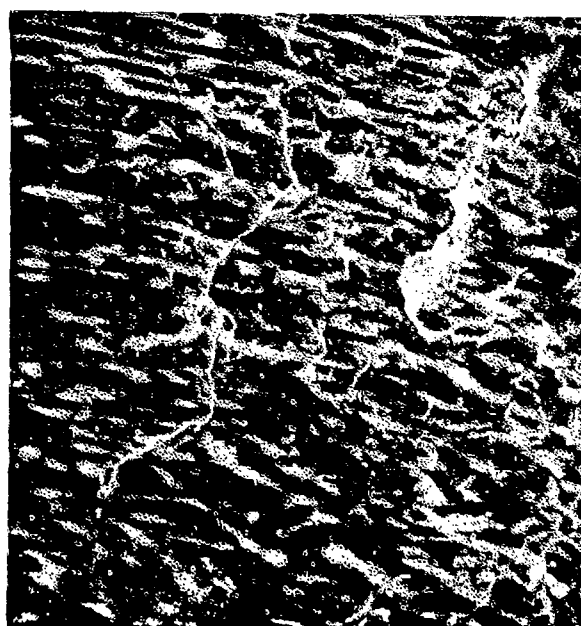


Figure 102. Stereo micrograph of fatigue zone in temper-embrittled HY-130 steel, 1500x.

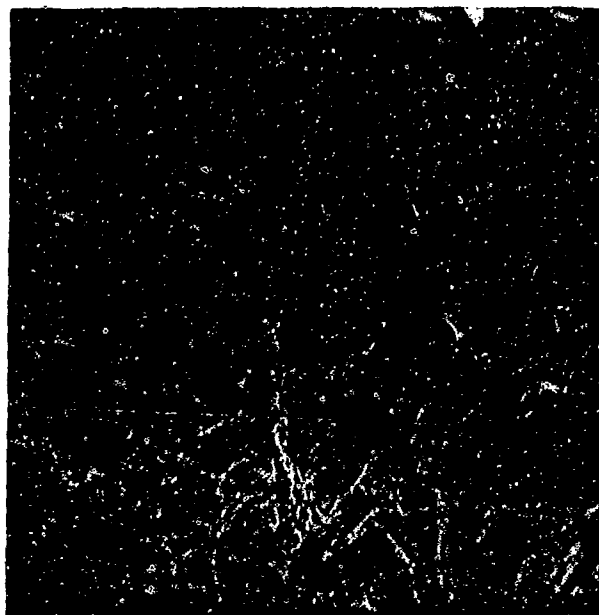


Figure 103. Slipping, tearing, and microvoid coalescence along one of laminates in temper-embrittled HY-130 steel, 800x.

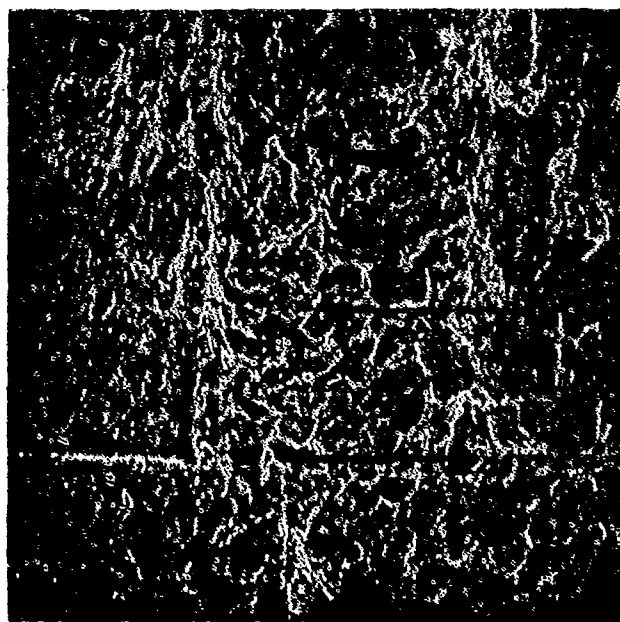


Figure 105

Figure 106

Figure 104. Band of intergranular fracture between fatigue and tensile overload zones, 160x.



Figure 105. Intergranular fracture in temper-embrittled HY-130 steel (located in center of 104), 1600x.

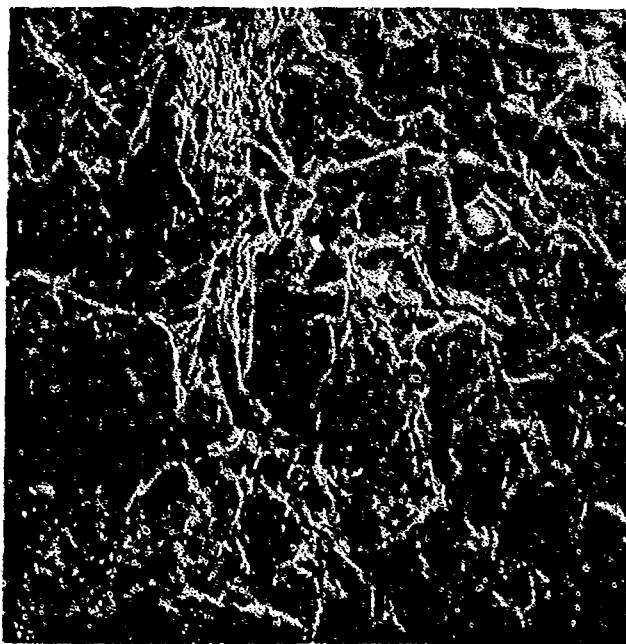


Figure 106. Intergranular fracture and microvoid coalescence in temper-embrittled HY-130 steel, 800x.



Figure 108

notch

Figure 107. Fracture surface of HY-130 Charpy specimen tested at -196°C , 8x.

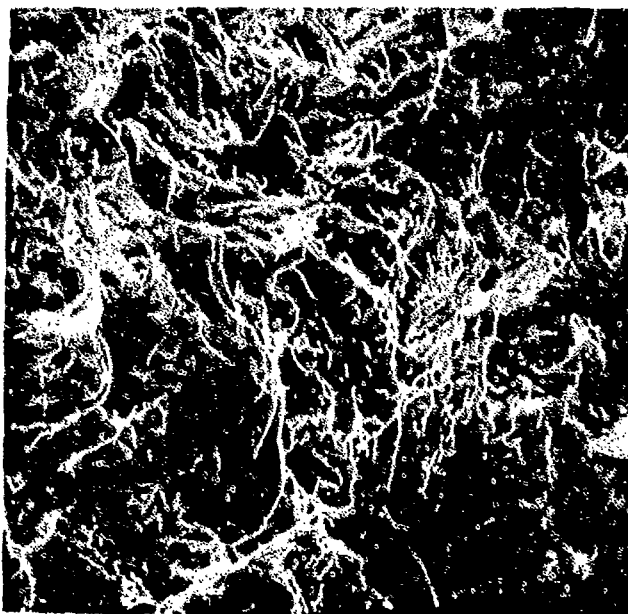
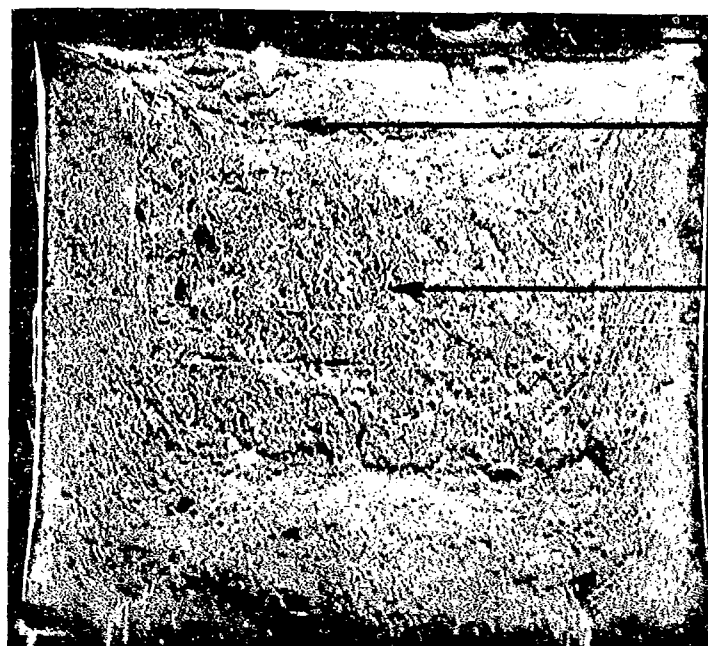


Figure 108. Cleavage fracture in HY-130 Charpy specimen tested at -196°C , 1600x.



notch

Figure 110

Figure 111

Figure 109. Fracture surface of HY-130 Charpy specimen tested at -83°C , 10x.

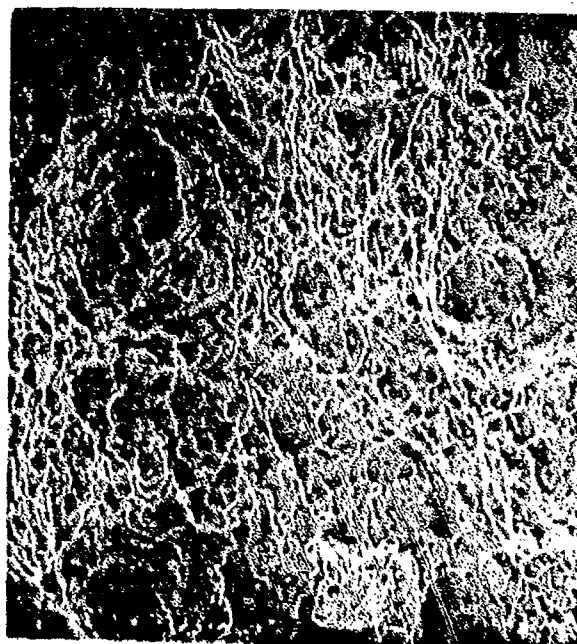


Figure 110. Edge of HY-130 Charpy specimen tested at -83°C , 650x.

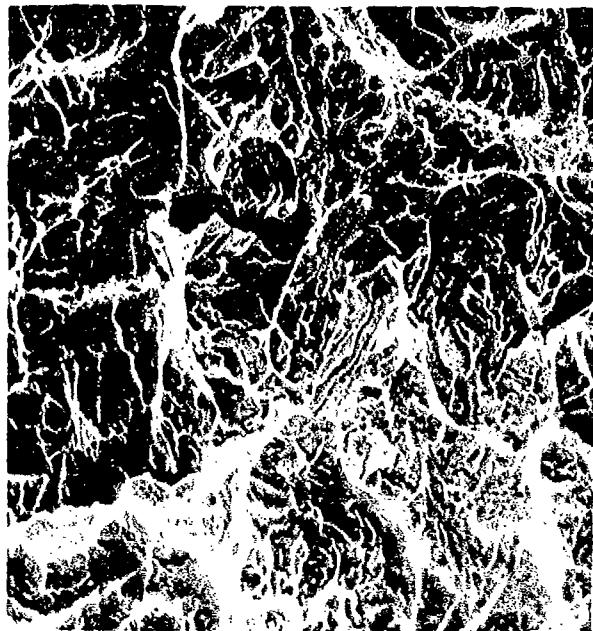


Figure 111. Center of HY-130 Charpy specimen tested at -83°C , 1600x.

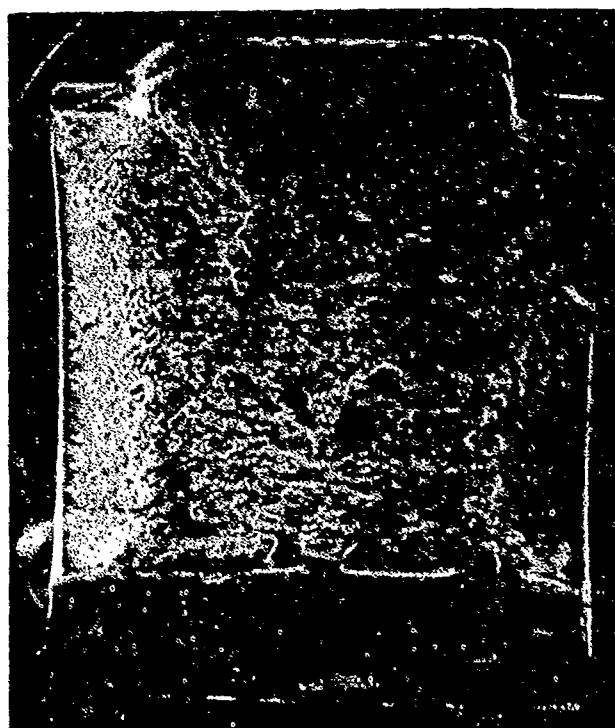


Figure 113

notch

Figure 112. Fracture surface of HY-130 Charpy specimen tested at -18°C , 8x.

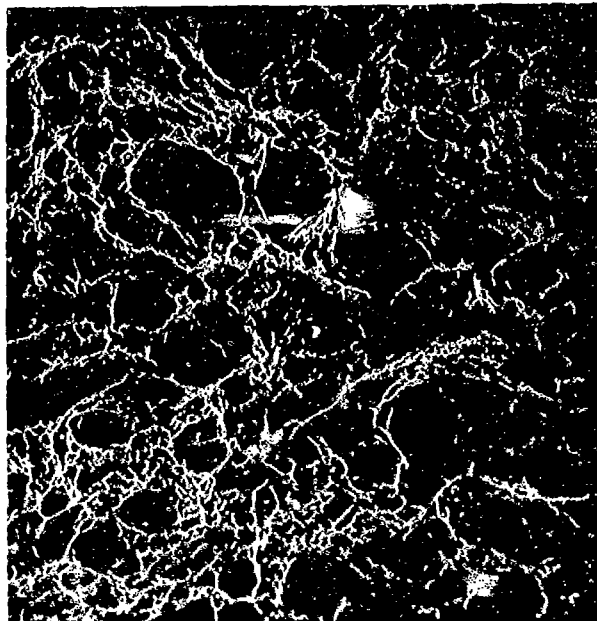


Figure 113. Failure of HY-130 Charpy specimen tested at -18°C , 1600x.

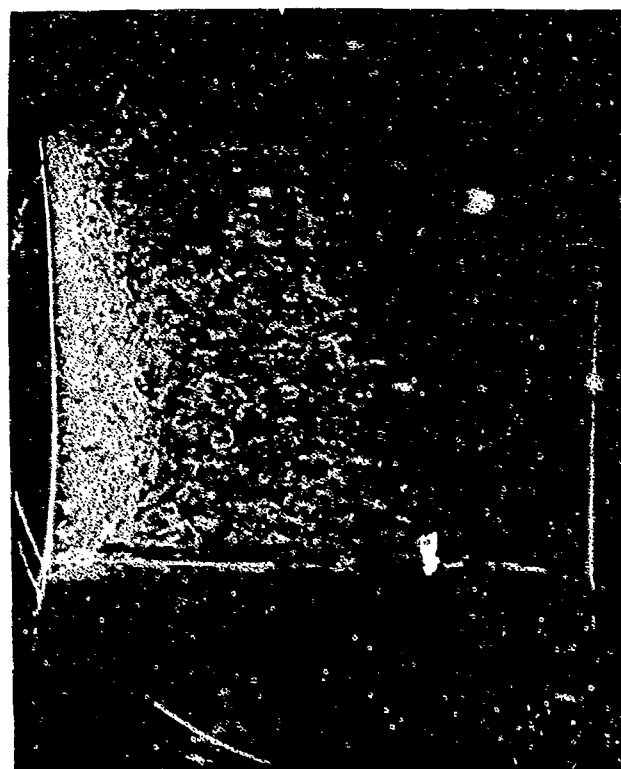


Figure 115

notch

Figure 114. Fracture surface of HY-130 Charpy specimen tested at room temperature, 8x.

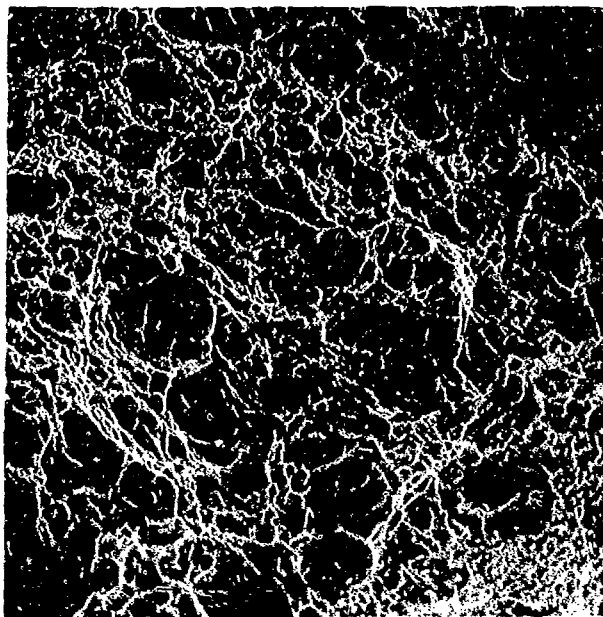


Figure 115. Failure of HY-130 Charpy specimen tested at room temperature by dimple rupture, 1600x.



Figure 117

Figure 116. Tensile fracture surface of an AX-110 weld specimen, 25x.

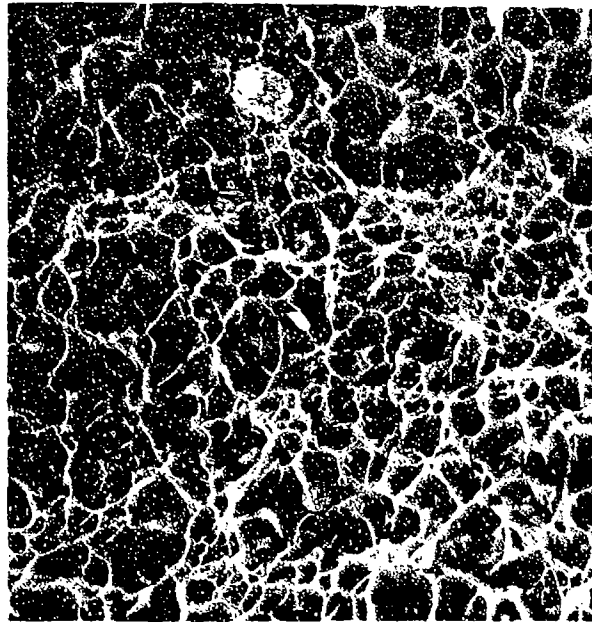


Figure 117. Tensile failure of AX-110 weld material by dimple rupture, 4000x.



Figure 118. Tensile fracture surface of hydrogen-embrittled AX-110 weld specimen, 25x.

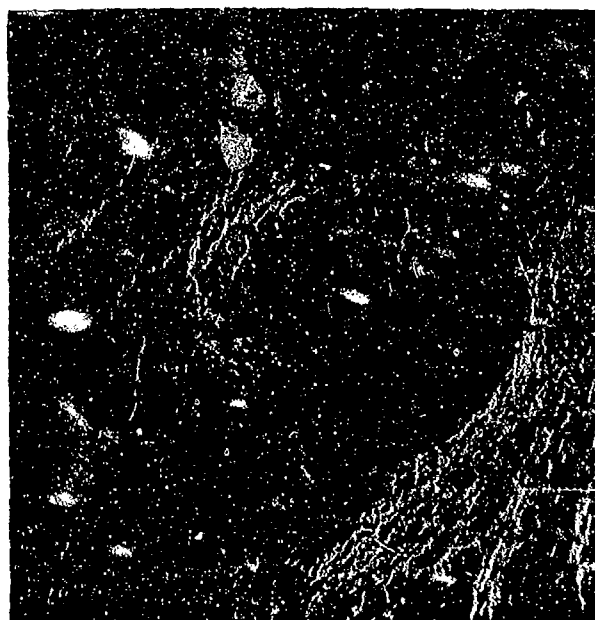


Figure 120

Figure 119. Fisheye on the fracture surface of hydrogen-embrittled AX-110 weld specimen, 150x.



Figure 121

Figure 120. Fracture surface of region in fisheye, 1600x.

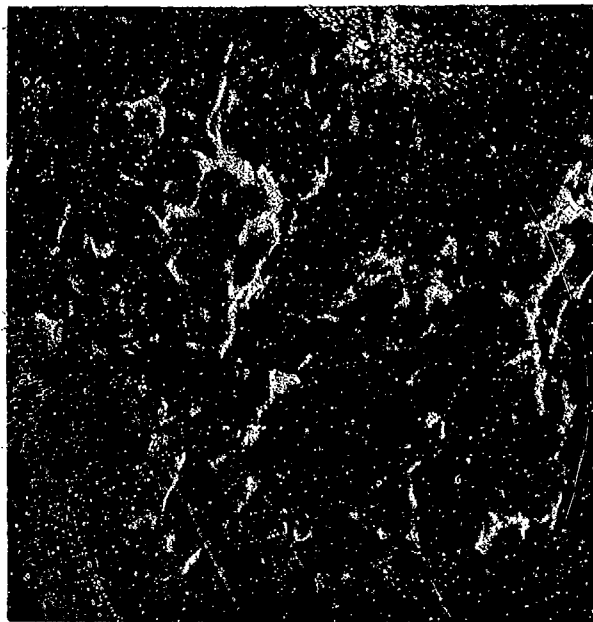


Figure 121. Small cleavage facets located in fisheye, 4000x.

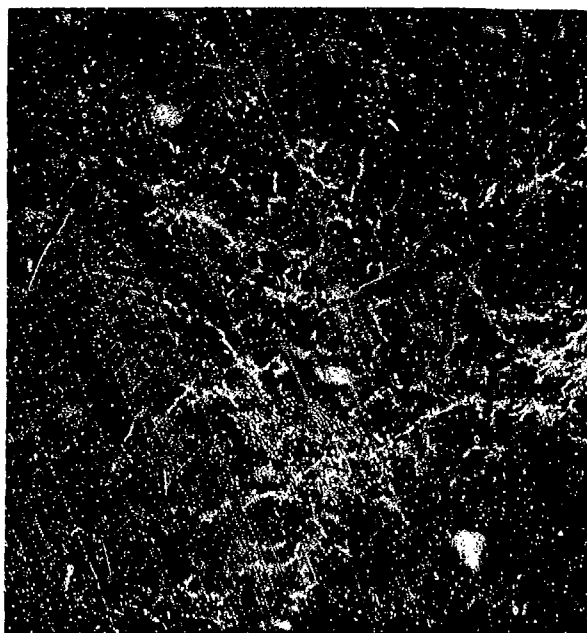


Figure 122. Fracture surface of hydrogen-embrittled AX-110 weld specimen away from fisheye, 1500x.



Figure 124

Figure 123. Tensile fracture surface of temper-embrittled AX-110 weld specimen, 15x.



Figure 124. Tensile failure of temper-embrittled AX-110 weld specimen by dimple rupture, 750x.

Figure 126

notch

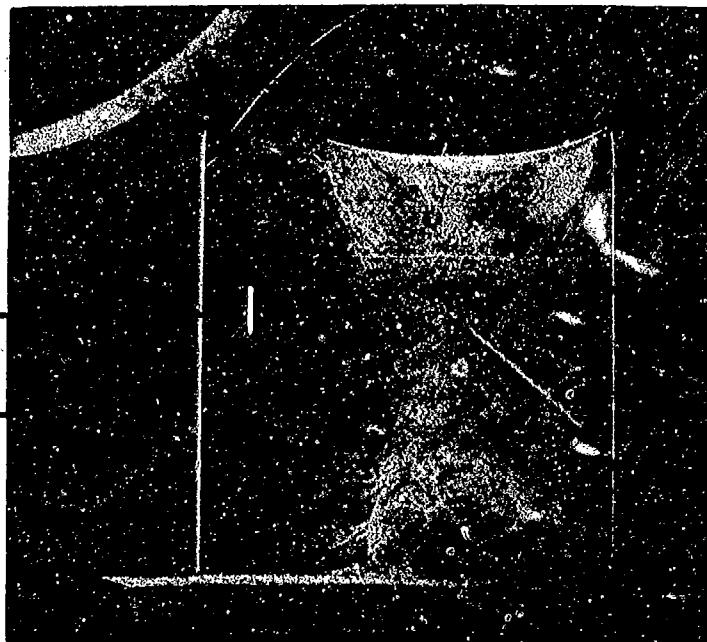


Figure 127

notch

Figure 125. Fatigue fracture surface of an AX-110 weld specimen, 11x.

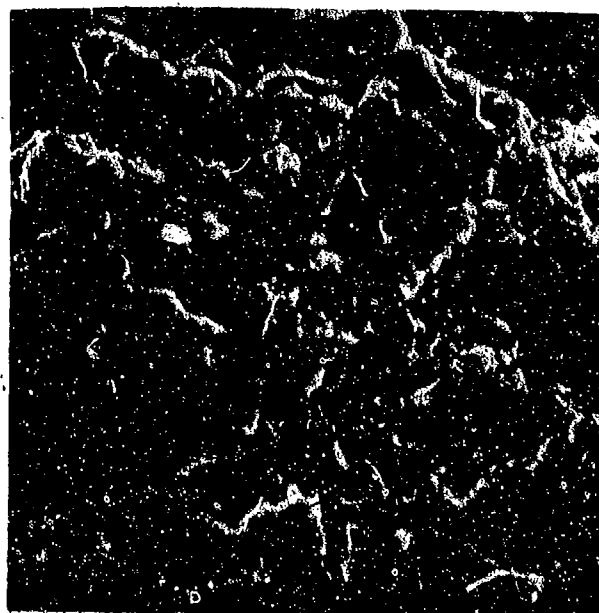


Figure 126. Fatigue cracks on fracture surface of AX-110 weld material, 4000x.

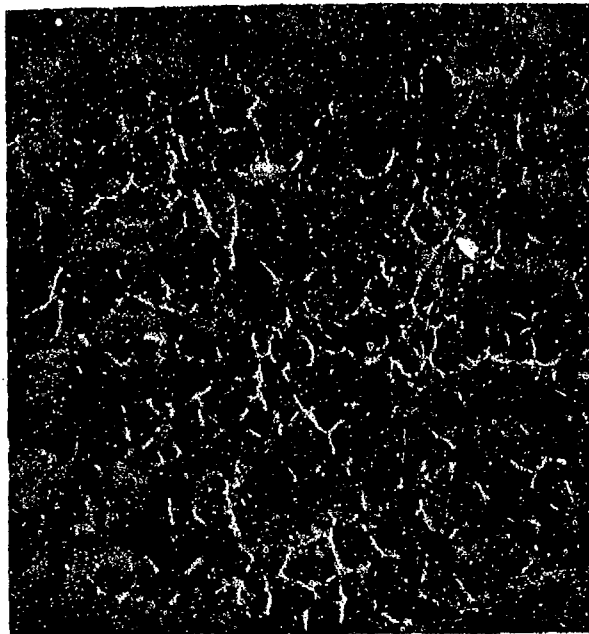


Figure 127. Tensile overload region of AX-110 weld fracture surface, 1500x.

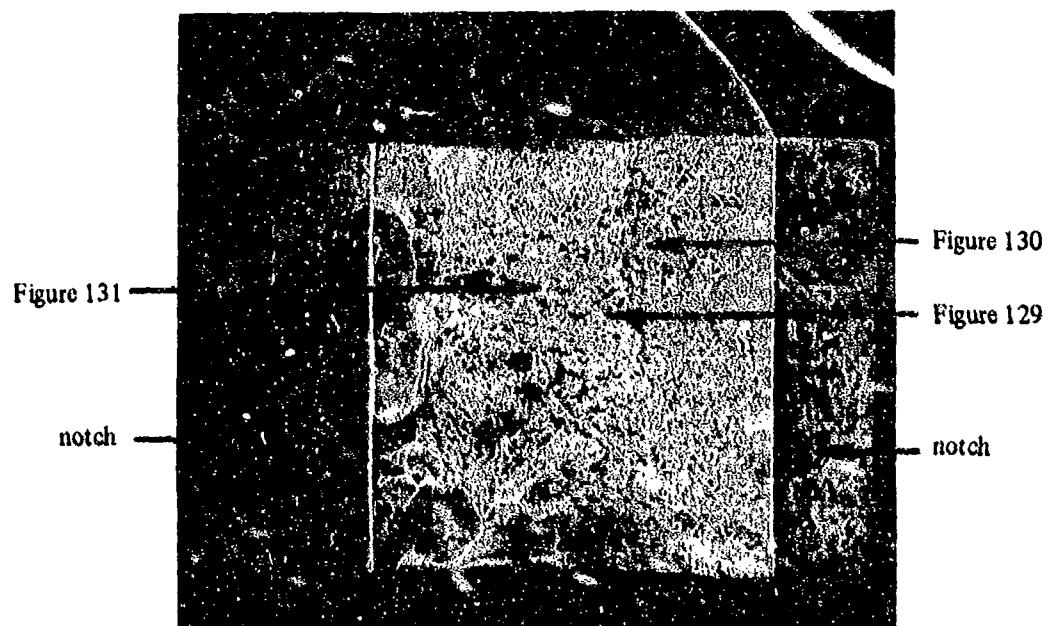


Figure 128. Fatigue fracture surface of hydrogen-embrittled AX-110 weld specimen, 10x.

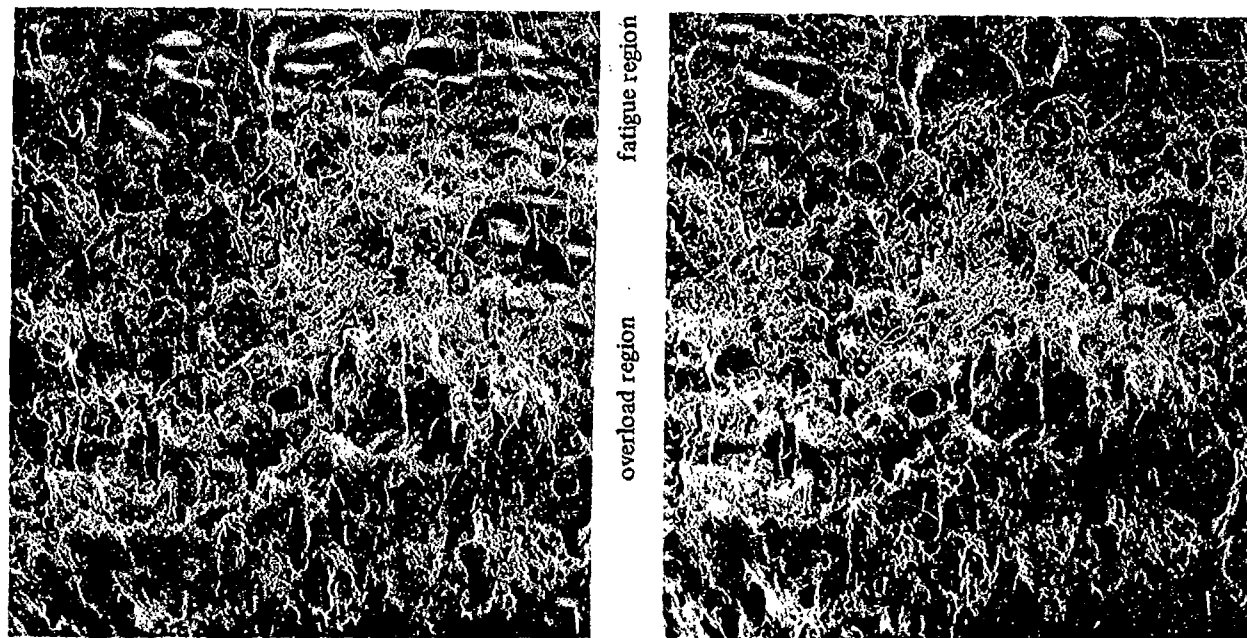


Figure 129. Stereo micrograph of fatigue region in a hydrogen-embrittled AX-110 weld specimen, 40x.



Figure 130. Fatigue striations on surface of hydrogen-embrittled AX-110 weld fatigue specimen, 2000x.

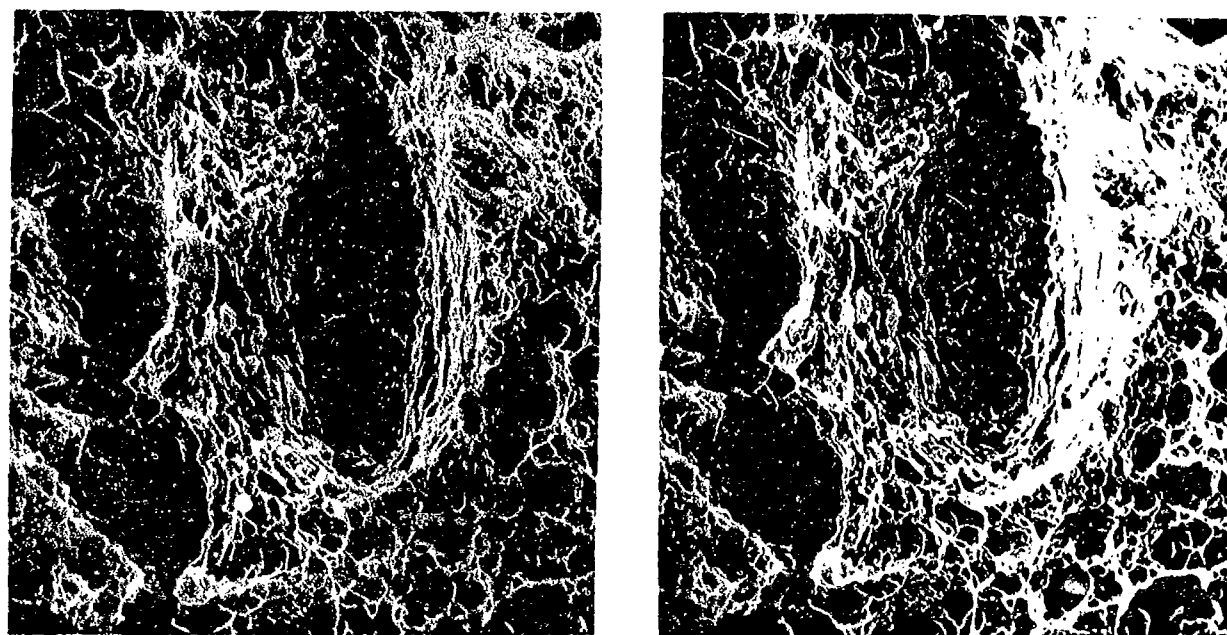


Figure 131. Stereo micrograph of the tensile overload region in a hydrogen-embrittled AX-110 weld fatigue specimen, 1600x.

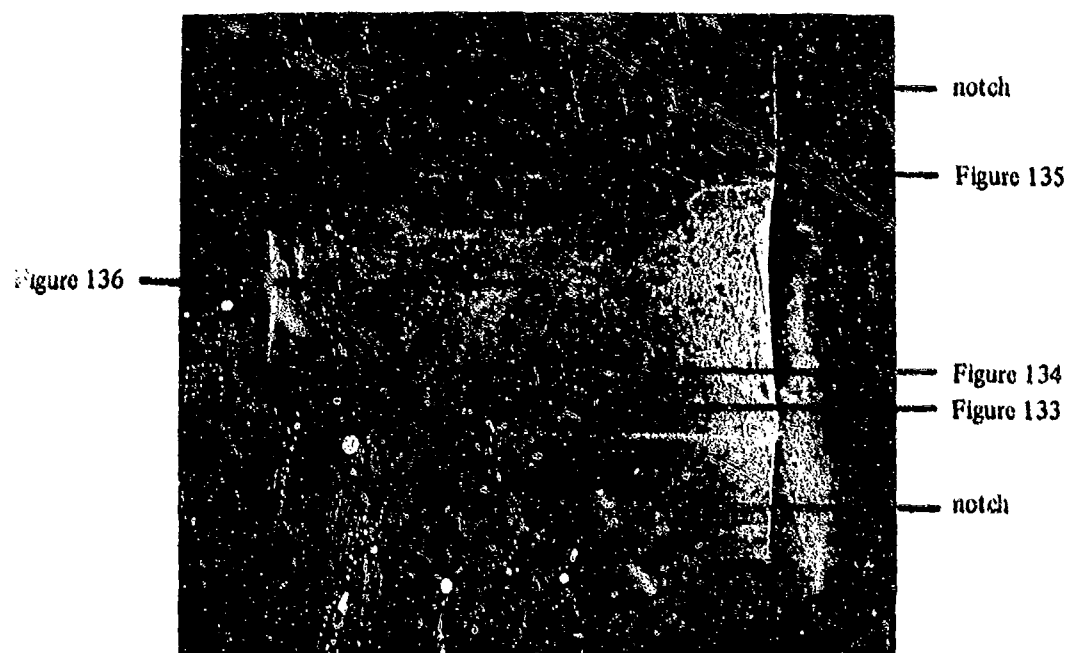


Figure 132. Fatigue fracture surface of temper-embrittled AX-110 weld specimen, 11x.

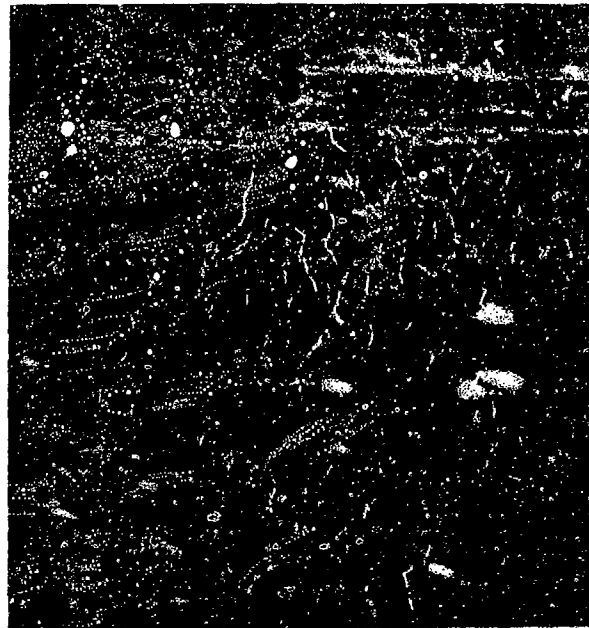


Figure 133. Fatigue region of temper-embrittled AX-110 weld fracture surface, 375x.

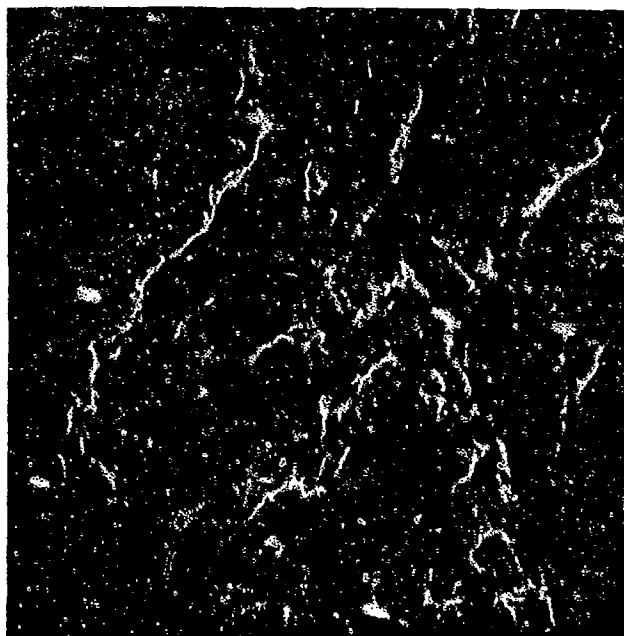


Figure 134. Fatigue striations on fracture surface of temper-embrittled AX-110 weld fatigue specimen, 1500x.

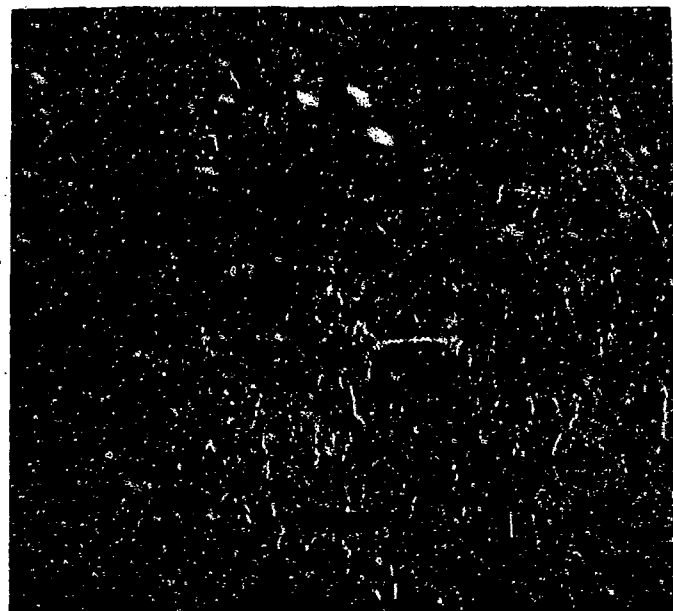


Figure 135. Lamellar tearing occurring in fatigue zone of temper-embrittled AX-110 weld specimen, 150x.

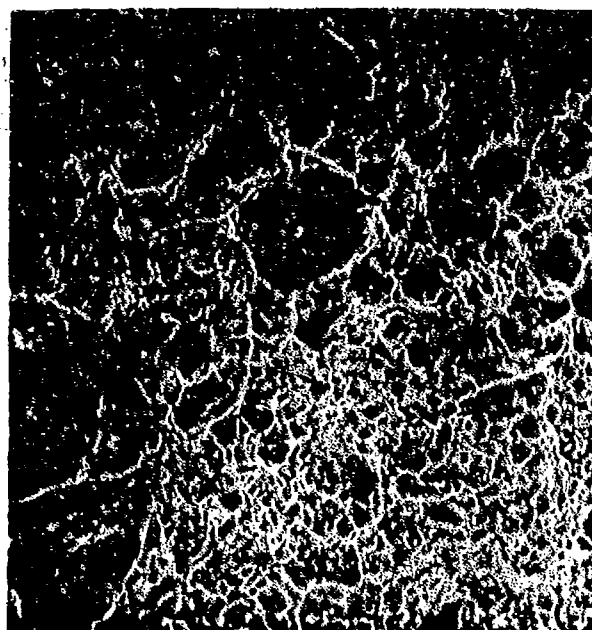


Figure 136. Tensile overload region in temper-embrittled AX-110 weld fatigue specimen, 750x.

notch



Figure 141

Figure 137. Fracture surface of AX-110 weld Charpy specimen tested at -196°C , 8x.



Figure 142

Figure 143

notch

Figure 138. Fracture surface of AX-110 weld Charpy specimen tested at -83°C , 8x.



Figure 144

notch

Figure 139. Fracture surface of AX-110 weld Charpy specimen tested at -18°C , 8x.



Figure 144

notch

Figure 140. Fracture surface of AX-110 weld Charpy specimen tested at room temperature, 8x.

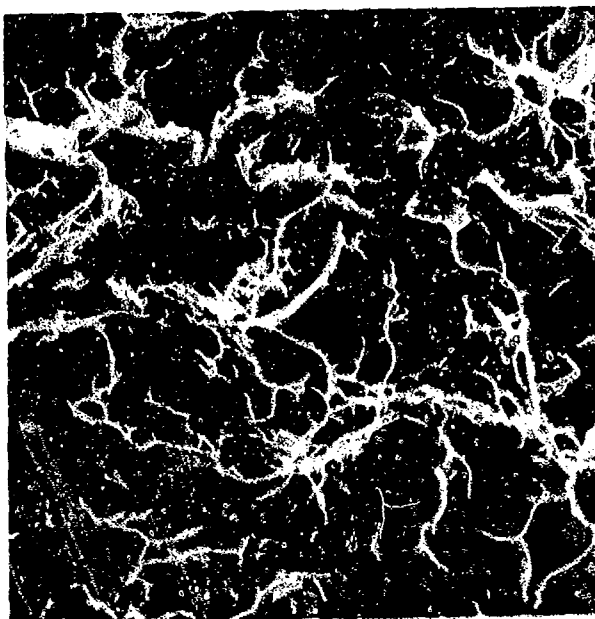


Figure 141. Failure of AX-110 weld Charpy specimen tested at -196°C by cleavage, 4000x.

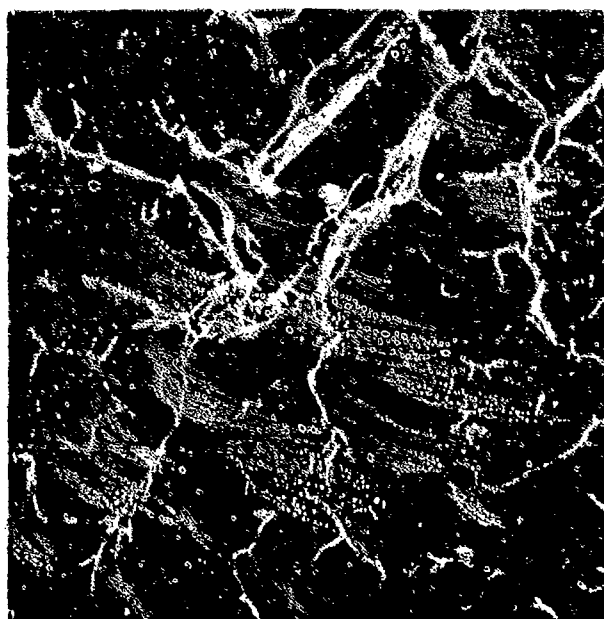


Figure 142. Center of AX-110 weld Charpy specimen tested at -83°C , 4000x.

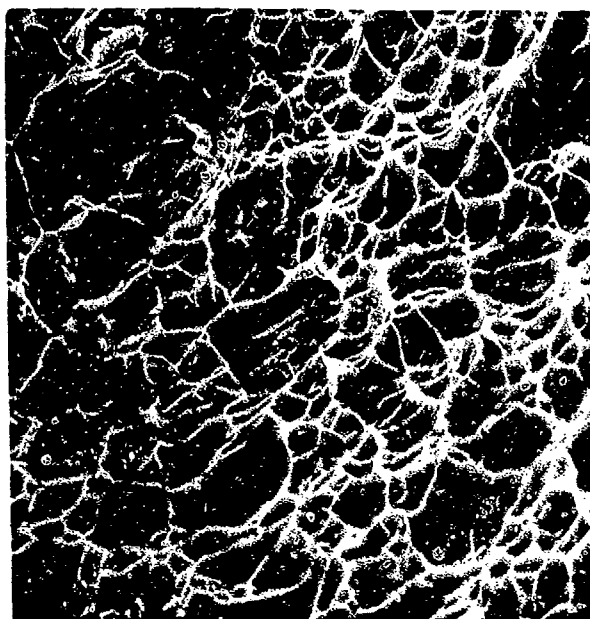


Figure 143. Edge of AX-110 weld Charpy specimen tested at -83°C , 4000x.

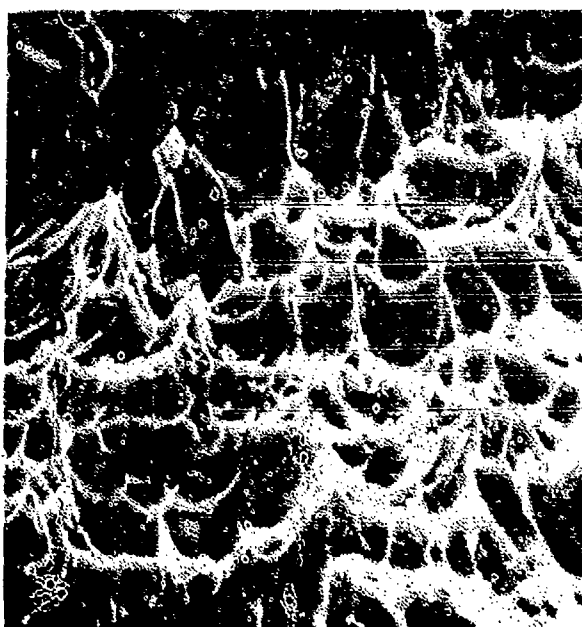


Figure 144. Fracture surface of AX-110 weld Charpy specimen tested at or above -18°C , 4250x.

Figure 146

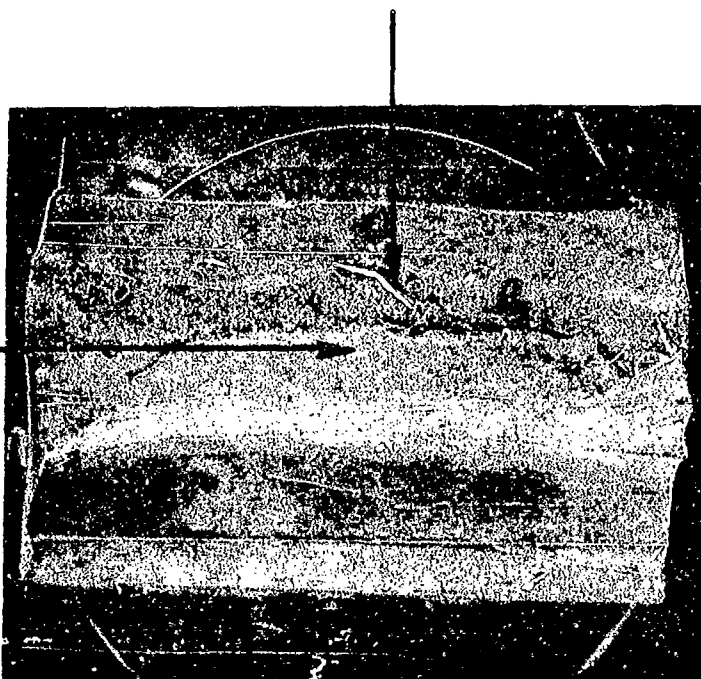


Figure 147

Figure 145. Tensile fracture surface of AX-110 weldment containing LOP, 8x.



Figure 146. LOP region on tensile fracture surface of AX-110 weldment, located in center of specimen, 250x.

Figure 148

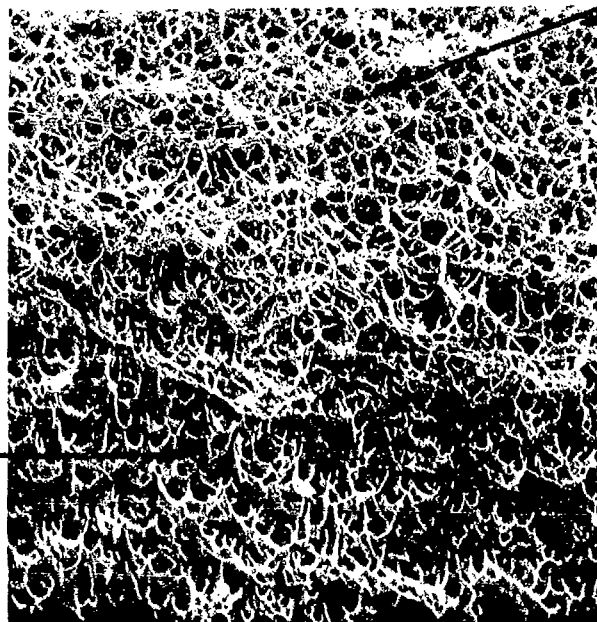


Figure 149

Figure 147. Transition region on tensile fracture surface of AX-110 weldment, 1900x.

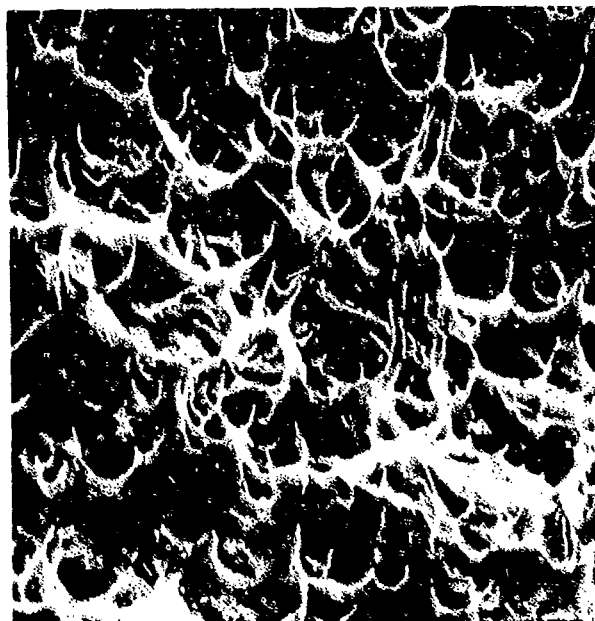


Figure 148. Elongated dimples on tensile fracture surface of AX-110 weldment, 4600x.

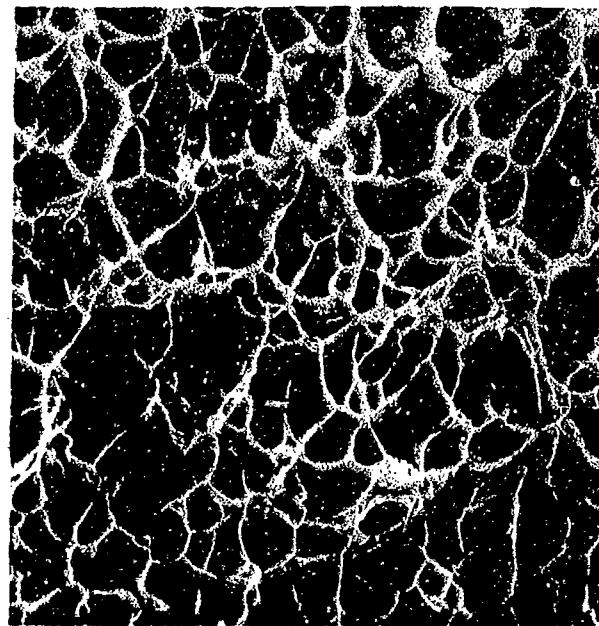


Figure 149. Equiaxed dimples on tensile fracture surface of AX-110 weldment, 4600x.

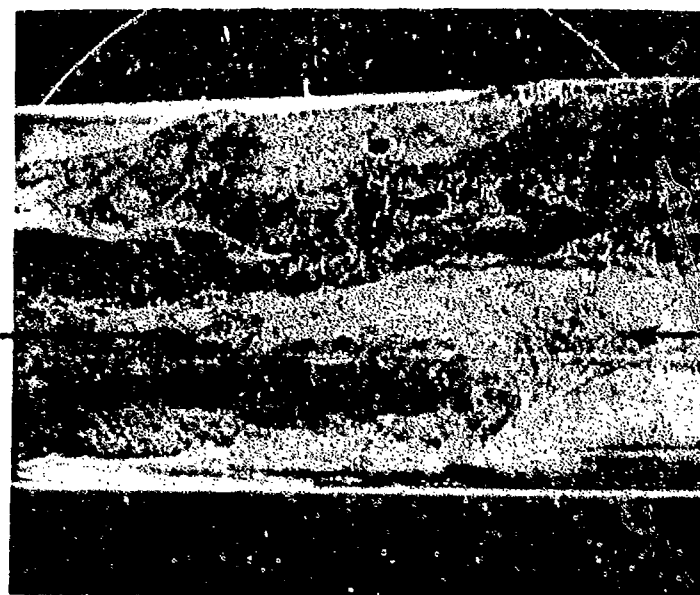


Figure 152

Figure 151

Figure 153

Figure 150. Tensile fracture surface of AX-110 weldment containing LOP and LOF, 8x.

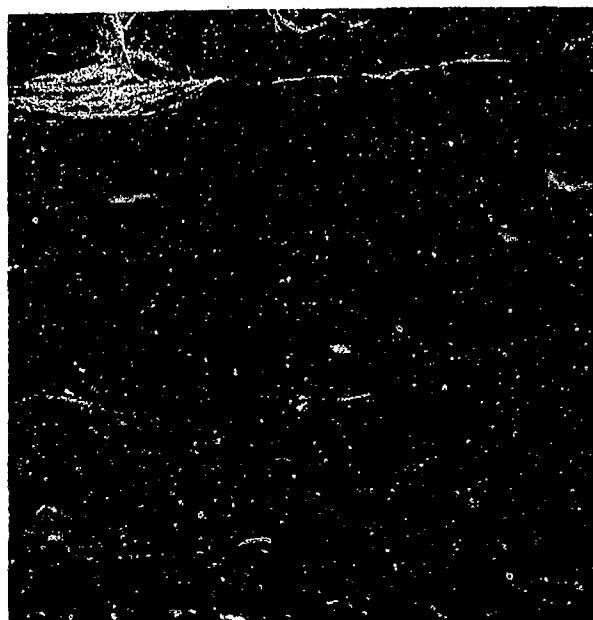


Figure 151. LOP region on tensile fracture surface of AX-110 weldment, 300x.

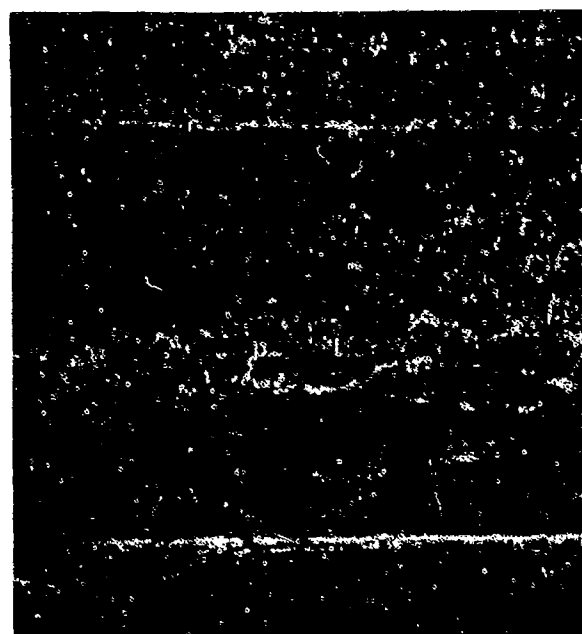


Figure 152. LOP region on tensile fracture surface of AX-110 weldment, 260x.

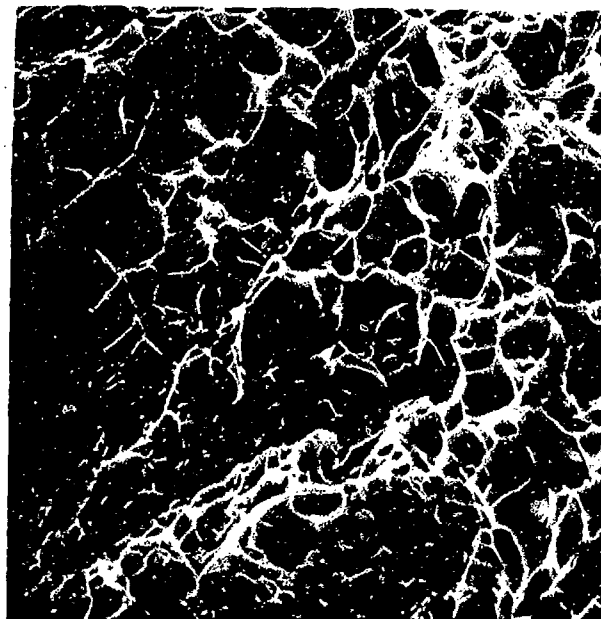


Figure 153. Region away from defects on AX-110 weldment fracture surface, 4000x.

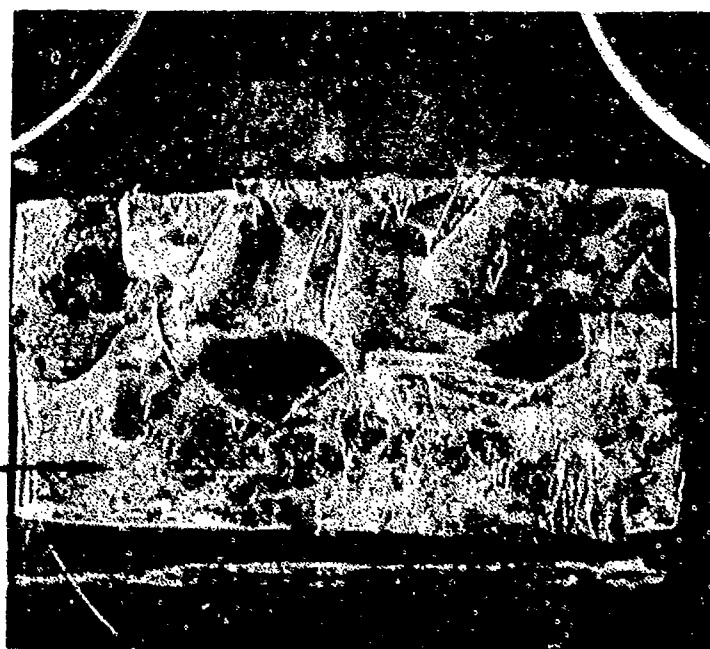


Figure 156

Figure 155

Figure 154. Tensile fracture surface of AX-110 weldment containing porosity, 8x.

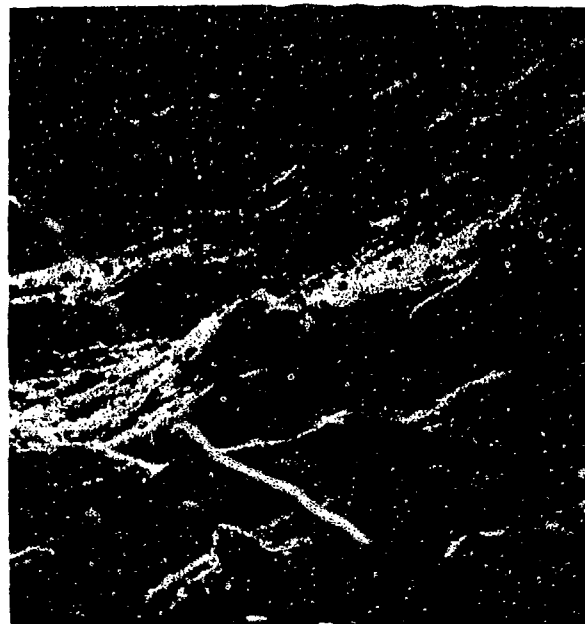


Figure 155. Interior surface of pore, 2500x.

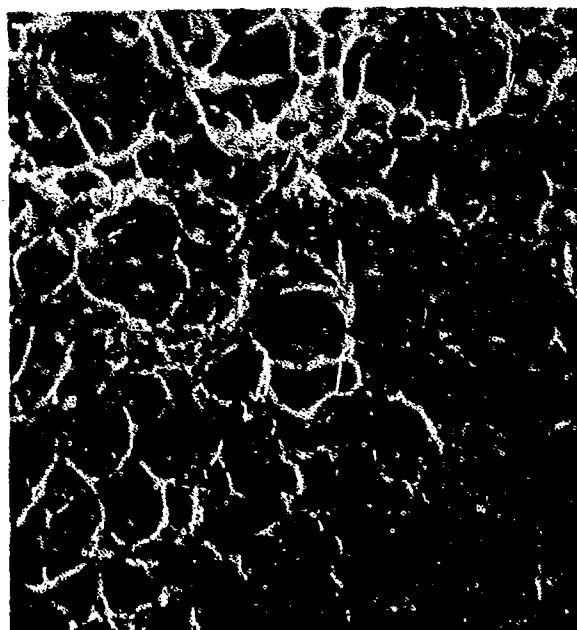


Figure 156. Fracture surface away from porosity defects, 3500x.

Figure 159



Figure 158

Figure 157. Fatigue fracture surface of AX-110 weldment containing LOP, 8x.

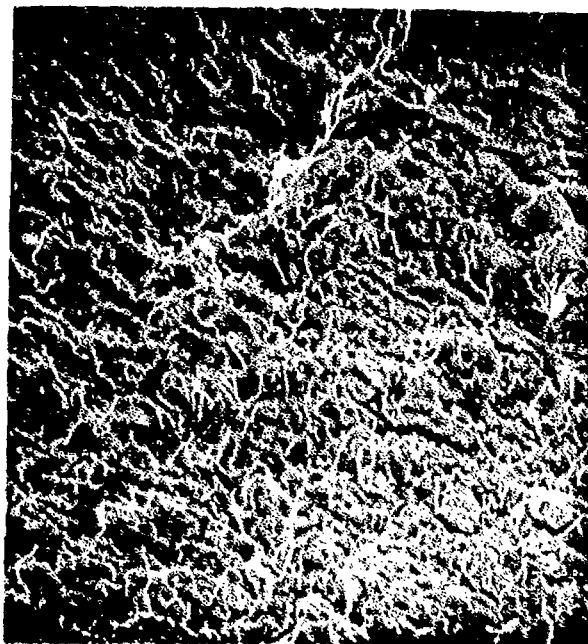


Figure 158. Fatigue region of fracture surface of AX-110 weldment containing LOP, 1700x.



Figure 159. Tensile overload region of fatigue fracture surface of AX-110 weldment containing LOP, 3250x.

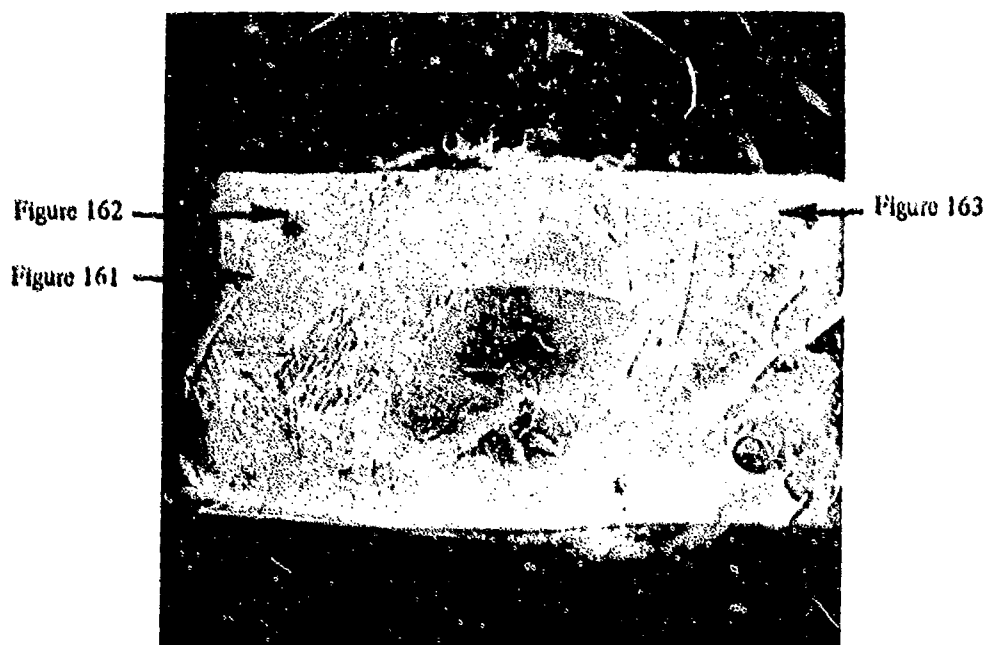


Figure 160. Fatigue fracture surface of AX-110 weldment containing porosity, 10x.

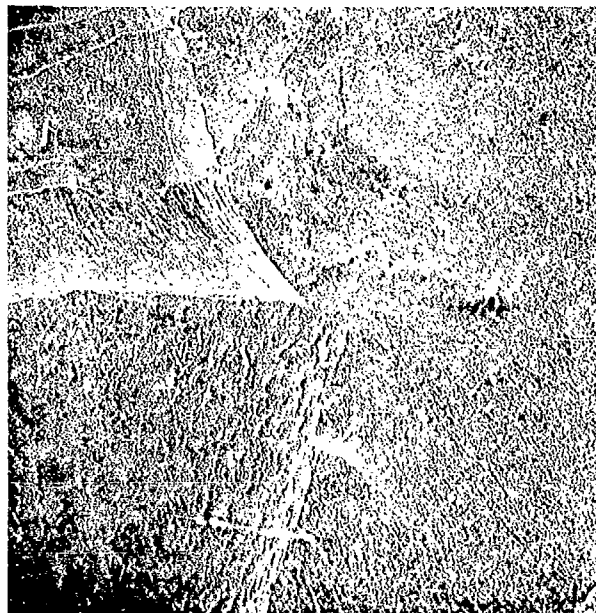


Figure 161. Fatigue initiation site on fracture surface of AX-110 weldment containing porosity, 50x.

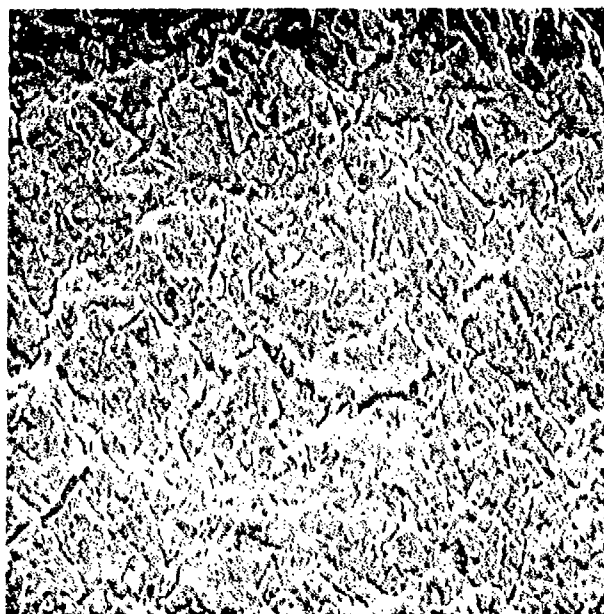


Figure 162. Fatigue region of fracture surface of AX-110 weldment containing porosity, 1380x.

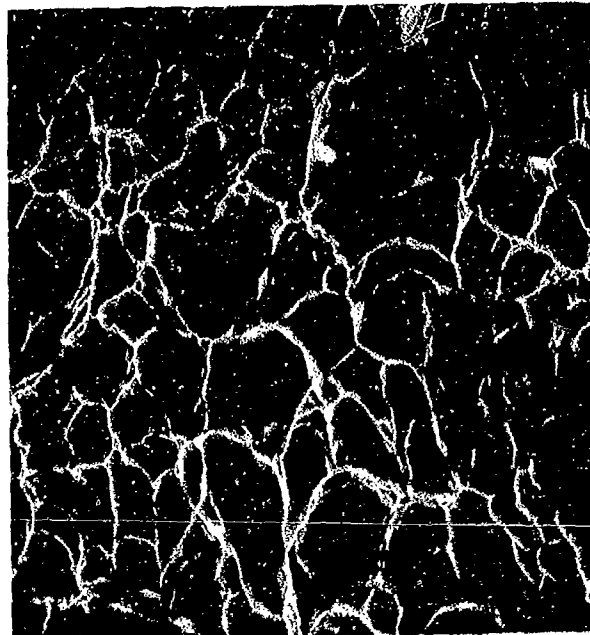


Figure 163. Tensile overload region of fracture surface of AX-110 weldment containing porosity, 1380x.

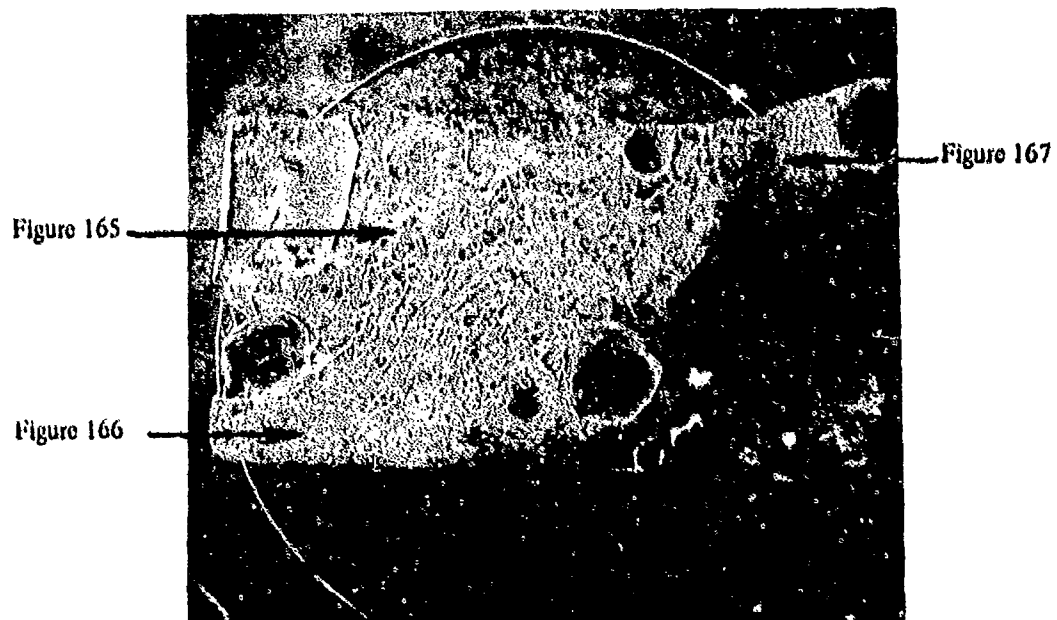


Figure 164. Fatigue fracture surface of a hydrogen-embrittled AX-110 weldment containing porosity, 8x.

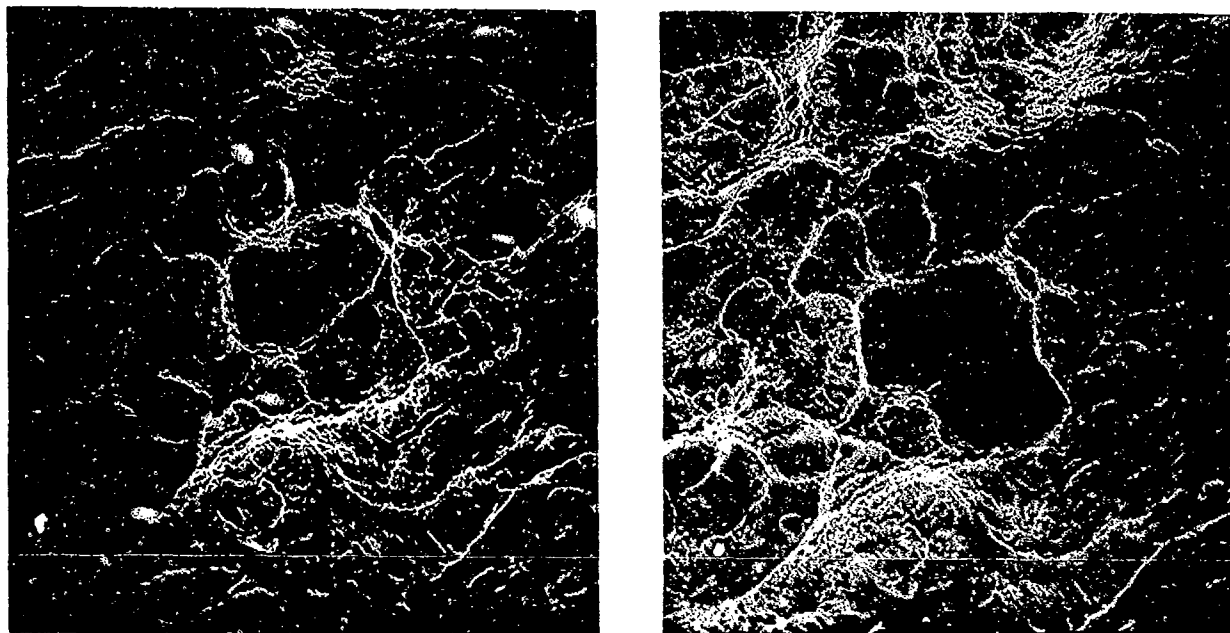


Figure 165. Stereo micrograph of fatigue region of hydrogen-embrittled AX-110 weldment containing porosity, 120x.

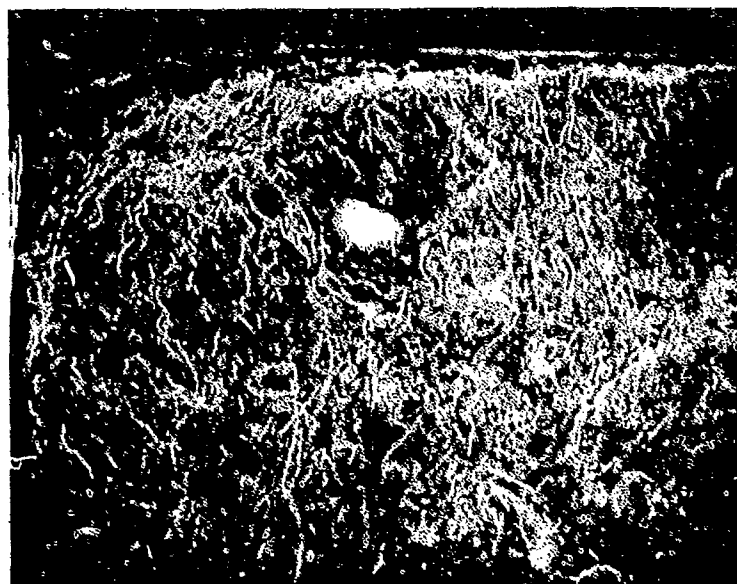


Figure 166. Origin of fatigue failure in hydrogen-embrittled AX-110 weldment containing porosity, 120x.

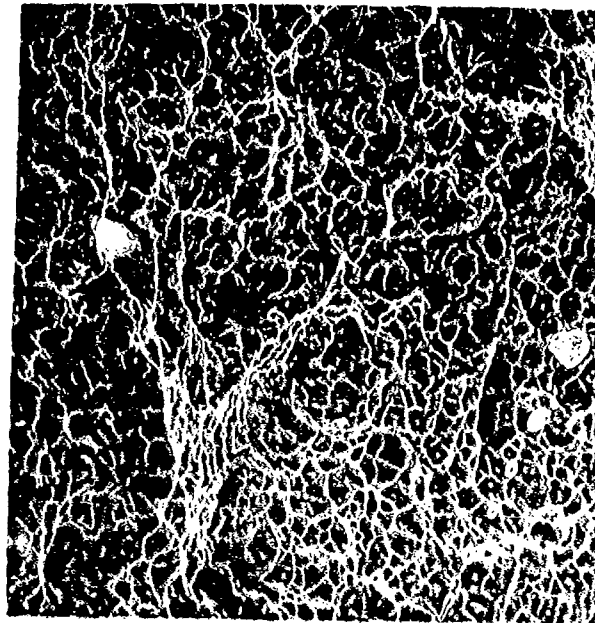


Figure 167. Tensile overload region in hydrogen-embrittled AX-110 weldment containing porosity, 1000x.

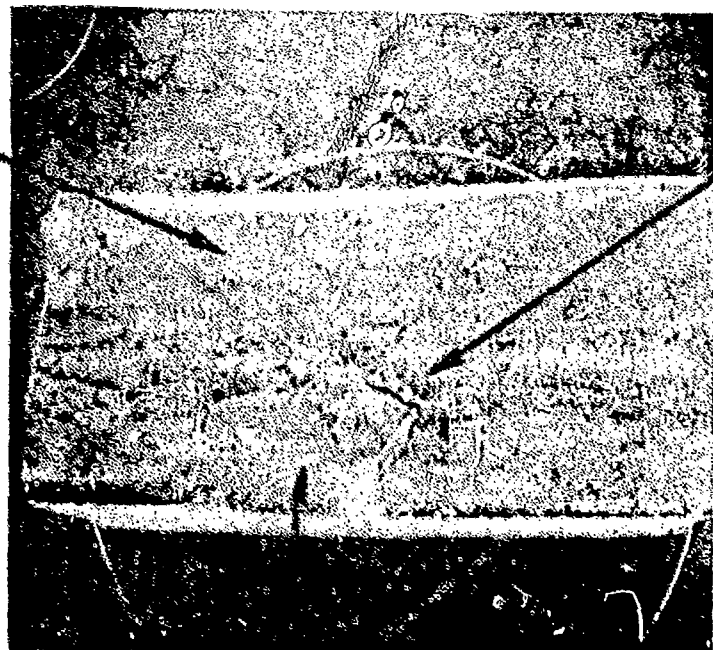


Figure 172

Figure 169

Figure 170

Figure 171

Figure 168. Fatigue fracture surface of temper-embrittled AX-110 weldment containing LOP, 8x.

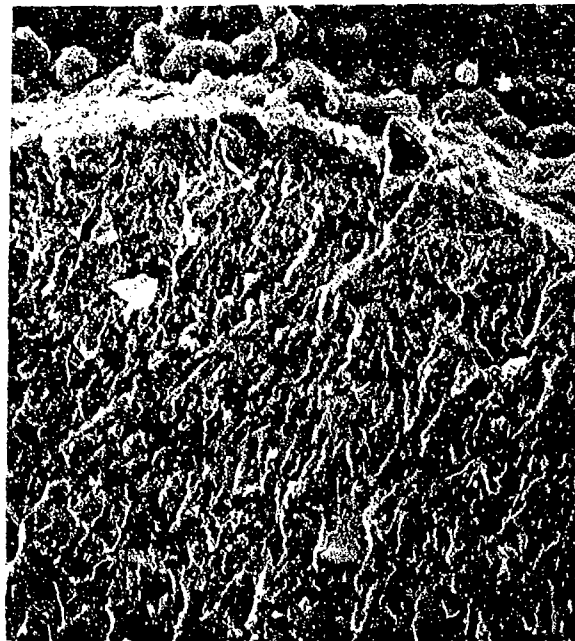


Figure 169. Origin of failure of temper-embrittled AX-110 weldment containing LOP, 1400x.

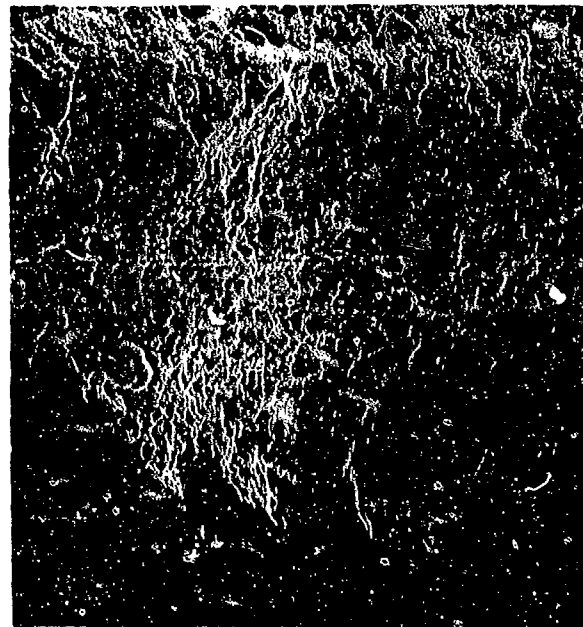


Figure 170. Secondary origin of fatigue failure of temper-embrittled AX-110 weldment containing LOP, 70x.

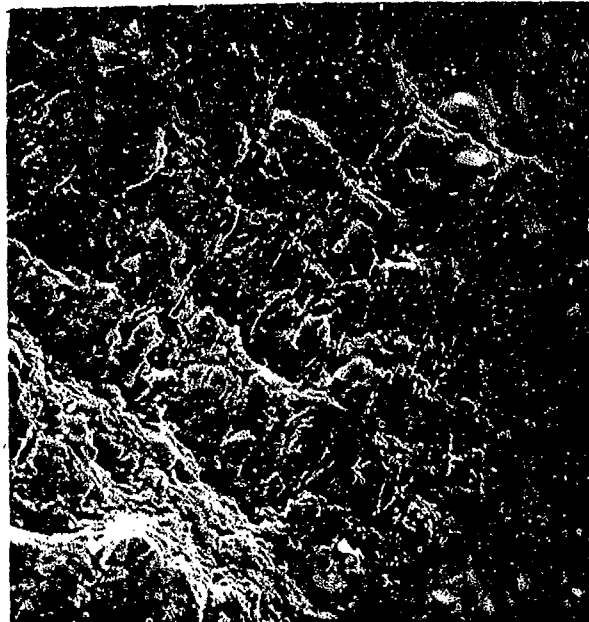


Figure 171. Fatigue striations on fracture surface of temper-embrittled AX-110 weldment containing LOP, 1400x.

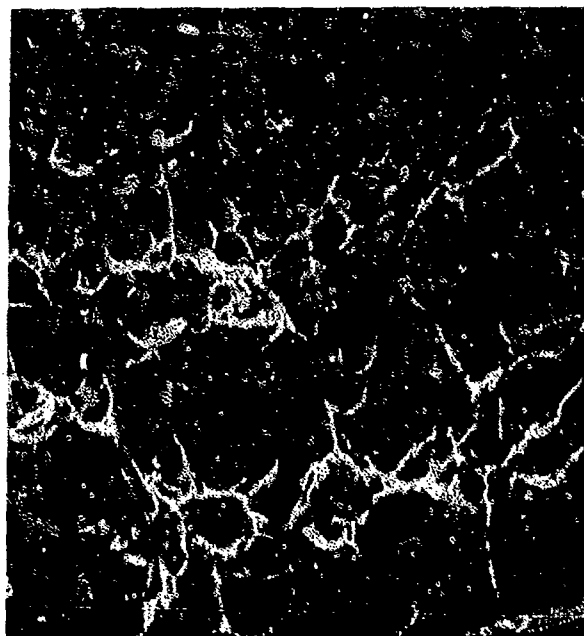


Figure 172. Elongated dimples on shear lip of fracture surface, 3500x.

GLOSSARY

crystal: A solid composed of atoms, ions, or molecules arranged in a pattern which is repetitive in three dimensions.

crystallographic plane: A plane which is formed by the atoms, ions, or molecules in a crystal.

grain: An individual crystal in a polycrystalline metal or alloy.

slip: Plastic deformation by the irreversible shear displacement (translation) of one part of a crystal relative to another in a definite crystallographic direction and usually on a specific crystallographic plane. Sometimes called "glide."

slip plane: The crystallographic plane in which slip occurs in a crystal.

slip system: A specific plane and direction in which slip occurs. Generally the slip plane is the plane of greatest atomic density, and the slip direction is the closest-packed direction within the slip plane.

REFERENCES

- Ault, R. T., R. B. Holtmann, and J. R. Myers, *Heat Treatment of a Martensitic Stainless Steel for Optimum Combination of Strength, Toughness, and Stress Corrosion Resistance*, Technical Report AFML-TR-68-7 (Air Force Materials Laboratory, April 1968).
- Beck, W., *Electrochemical Technology*, Vol 2 (1964), pp 74-78.
- Beck, W., E. J. Jankowski, and P. Fisher, *Hydrogen Stress Cracking of High-Strength Steels*, NADC-MA-7140 (Naval Air Development Center, 1971).
- Bornstein, I. M., "The Role of Hydrogen in the Embrittlement of Iron and Steel," *Materials Science and Engineering*, Vol 6, No. 1 (1970), pp 1-19.
- Cotterill, P., "The Hydrogen Embrittlement of Metals," *Progressive Materials Science*, Vol 9, No. 4 (1961).
- Forsyth, P. J. E., "Fatigue Damage and Crack Growth in Aluminum Alloys," *ACTA Metallurgica*, Vol 2, No. 703, 1963.
- Fractography and Atlas of Fractographs*, ASM Metals Handbook, Vol 9, 8th Edition (American Society for Metals [ASM], 1974).
- Harrison, J. D. and G. C. Smith, *British Welding Journal*, Vol 14 (1967), pp 493-502.
- Heat Treating, Cleaning, and Finishing*, ASM Metals Handbook, Vol 2, 8th Edition (1964), p 245.
- Hill, M. N. and E. W. Johnson, *Transactions of the American Institute of Mining, Metallurgical and Petroleum Engineers (AIME)*, Vol 215, No. 717 (1959).
- Honda, R., *International Conference on Fracture*, Sendai, Japan (1965).
- Hydrogen Embrittlement Testing*, ASTM STP543 (American Society for Testing and Materials [ASTM], 1974).
- Joshi, A., and D. F. Stein, *Temper Embrittlement of Alloy Steels*, ASTM STP 499 (ASTM, 1972), pp 59-89.
- Laird, C., and G. C. Smith, "Crack Propagation in High Stress Fatigue" *Philosophical Magazine*, Vol II (1962), p 847.
- Low, J. R., Jr., *Fracture of Engineering Materials* (ASM, 1964), p 127.
- Low, J. R., Jr., B. L. Averbach, et al., *Fracture* (John Wiley, 1959), p 163.
- Low, J. R., Jr., D. F. Stein, A. M. Turkalo, and R. P. Lafarel, *Transactions of AIME*, MT6TB, Vol 242 (1968), pp 14-24.
- Marcus, H. L., Jr., and P. W. Palmberg, "Effect of Solute Elements on Temper Embrittlement of Low Alloy Steels," *Temper Embrittlement of Steels*, ASTM STP 499 (ASTM, 1971), pp 90-103.
- McMahon, C. J., Jr., *Temper Embrittlement in Steel*, ASTM STP 407 (ASTM, 1968), p 127.
- Ohtani, H., H. C. Feng, and C. J. McMahon, Jr., "New Information on the Mechanism of Temper Embrittlement of Alloy Steels," *Metallurgical Transactions*, Vol 5 (1974), pp 516-518.

Personal Communication with R. A. Swift, January 1973 Concerning Temper Embrittlement. Study of HY-130 Steel.

Petch, N. J., "The Ductile Fracture of Polycrystalline-Iron," *Philosophical Magazine*, Vol 1 (1956), pp 186-191.

Phillips, A., ed., *The Welding Handbook*, Vol 1 (American Welding Society, 1968).

Schwen, G., G. Sachs, and K. Tonk, *ASTM Proceedings*, Vol 57 (1957), pp 682-697.

Scultz, B. J. and C. J. McMahon, Jr., *Temper Embrittlement of Alloy Steels*, ASTM STP 499 (ASTM, 1972), pp 104-135.

Sptizig, W. A., P. M. Talda, and R. P. Wei, "Fatigue-Crack Propagation and Fractographic Analysis of 18 Ni (250) Maraging Steel Tested in Argon and Hydrogen Environments," *Engineering Fracture Mechanics*, Vol 1 (1968), pp 155-165.

Tetelman, A. S., and A. J. McEvily, Jr., *Fracture of Structural Materials* (John Wiley, 1967).

Troiano, A., "The Role of Hydrogen and Other Interstitials in the Mechanical Behavior of Metals," *Transactions of the American Society for Metals (ASM)*, Vol 52 (1960), p 52.

Warren, D. and R. D. Stout, *Welding Journal*, Vol 3, No. 8, Research Support 381-5 (1952).

Zaffe, C. A., *Journal of Iron and Steel Institute*, Vol 154, No. 123 (1946).

CERL DISTRIBUTION

Chief of Engineers
ATTN: DAEN-MCZ-S (2)
ATTN: DAEN-ASI-L
ATTN: DAEN-FEE-A
ATTN: DAEN-FE
ATTN: DAEN-RO
ATTN: DAEN-CWZ-R (3)
ATTN: DAEN-MCE-D
ATTN: CWR-R (2)
Dept of the Army
WASH DC 20314

U.S. Military Academy
ATTN: Dept of Mechanics
ATTN: Library
West Point, NY 10996

The Engineering School
Technical Information Br.
Archives Section (Bldg 270)
Ft Belvoir, VA 22060

USA Engineering School
ATTN: ATSEN-DT-LD (2)
Ft Belvoir, VA 22060

Director
USA Cold Regions Research
Engineering Laboratory
PO Box 282
Hanover, NH 03755

Director, USA-WES
ATTN: Concrete Div
ATTN: Soils Div
ATTN: Library
PO Box 631
Vicksburg, MS 39181

Deputy Chief of Staff
for Logistics
US Army, The Pentagon
WASH DC 20310

The Army Library
Office of the Adjutant
General
Room 1A530, The Pentagon
WASH DC 20315

HQDA (SGRD/Chief),
Sanitary Engr Br
WASH DC 20314

Dept of the Army
ATTN: EACICT-P
HQ I Corps (Group)
APO San Francisco 96358

Commander-in-Chief
US Army, Europe
ATTN: AEAE
APO New York, NY 09403

Commander, Naval Facilities
Engineering Command
ATTN: Dep Ass't Commander
for Design & Spec (O4D)
200 Stenall Street
Alexandria, VA 22332

Chief, Naval Operations
ATTN: The Library
Dept of the Navy
WASH DC 20360

Chief, Hydrographic Office
ATTN: The Library
Dept of the Navy
WASH DC 20360

Chief
Naval Air Systems Command
ATTN: The Library
Dept of the Navy
WASH DC 20360

Naval Civil Engineering Lab
Technical Library Code L31
Port Hueneme, CA 93043

Officer in Charge
Naval Civil Engineering Lab
Port Hueneme, CA 93043

AF Civil Engr Center/PG
Tyndall AFB, FL 32401

AFWL/Civil Engr Div
Kirtland AFB, NM 87117

AF/PREE
Bolling AFB, DC 20332

AF/RDPO
WASH DC 20330

Each Division Engineer
US Army Engr Div
ATTN: Library
ATTN: Chief, Engr Div

Each District Engineer
US Army Engr District
ATTN: Library
ATTN: Chief, Engr Div

Defense Documentation
Center
ATTN: TCA (12)
Cameron Station
Alexandria, VA 22314

Chief, Airports Standard
Div-A558
Federal Aviation Administration
800 Independence Ave SW
WASH DC 20553

Office of Management Svc.
MS 110 - FAA
800 Independence Ave SW
WASH DC 20553

Transportation Research Board
National Research Council (3)
2101 Constitution Ave
WASH DC 20418

Dept of Trans Library
Acquisitions Section (SR)
TAD-491.1
400 7th Street SW
WASH DC 20590

Engineering Societies Library
345 East 47th Street
New York, NY 10017

Library of Congress (2)
Exchange and Gift Div
ATTN: American & British
WASH DC 20540

Superintendent of Documents
Div of Public Documents
ATTN: Library (2)
US Govt Printing Office
WASH DC 20402

Commanding General
USA Engr Command, Europe
APO New York, NY 09403

Engineer
US Army, Alaska
APO Seattle, WA 98749

Commander, TRADOC
Office of the Engineer
ATTN: ATEN
Ft Monroe, VA 23651

Bldg Research Advisory Board
National Academy of Sciences
2101 Constitution Avenue
WASH DC 20418

Air Force Weapons Lab
Technical Library (DOUL)
Kirtland AFB, NM 87117

Commanding General
US Army Forces Command
ATTN: AFEN-FEB
Ft. McPherson, GA 30330

Commanding General, 5th USA
ATTN: Engineer
Ft Sam Houston, TX 78234

Commanding General, 6th USA
ATTN: Engineer
Presidio of San Francisco, CA
94129

Plastics Technical Evaluation
Center
ATTN: SHUPA-VP1
Picatinny Arsenal
Dover, NY 07801

Institute of Defense Analysis
400 Army-Navy Drive
Arlington, VA 22202

Defense Logistics Studies Infor-
mation Exchange (2)
U.S. Army Logistics Management
Center
ATTN: AMHMC-II
Ft. Lee, VA 23801

Chief, Civil Engineering Research
Division
Air Force Weapons Lab AFWL/III
Kirtland AFB, NM 87117

Coastal Engineering
Research Center
Kingman Bldg
ATTN: Library
Ft. Belvoir, VA 22060

Dept of the Army
HQ 15th Engineer Battalion
9th Infantry Division
Ft. Lewis, WA 98433

Main Library, Documents
Section
State University of
New York at Stony Brook
Stony Brook, NY 11790

W. N. Lofroos, P.E.
Chief, Bureau of Planning
Dept of Transportation
605 Suwannee St.
Tallahassee, FL 32304

Dept of the Army
U.S. Army Human Engr Lab
ATTN: AMZHE/J. D. Weisz
Aberdeen Proving Ground,
MD 21005

Naval Facilities Engineering
Command
ATTN: Code 04
200 Stovall St.
Alexandria, VA 22332

Ass't Chief of Engineers
ATTN: DAEN-ZC1
WASH DC 20314

314/DEEE
Little Rock Air Force Base
Jacksonville, AR 72076

Chief of Engineers
ATTN: DAEN-PMS (12)
Dept of the Army
WASH DC 20314

For forwarding to:

British Liaison Officer (5)
U. S. Army Mobility Equipment
Research and Development Center
Fort Belvoir, VA 22060

Canadian Forces Liaison Officer (4)
U. S. Army Mobility Equipment
Research and Development Center
Fort Belvoir, VA 22060

Chief
Construction Engineer
Air Service Branch
Department of Transport
Ottawa, Ontario, Canada

Div of Bldg Research
National Research Council
Montreal Road
Ottawa, Ontario, K1A0R6

National Defense Headquarters
Director General of Construction
Ottawa, Ontario K1A 0K2
Canada